UNIVERSITÀ DEGLI STUDI DI CATANIA
DIPARTIMENTO DI FISICA E ASTRONOMIA
DOTTORATO DI RICERCA IN FISICA

Lucia Oliva

IMPACT OF THE PRE-EQUILIBRIUM STAGE OF ULTRA-RELATIVISTIC HEAVY ION COLLISIONS: ISOTROPIZATION, PHOTON PRODUCTION AND ELLIPTIC FLOWS

TESI DI DOTTORATO

Supervisor:
Chiar.mo Prof. Vincenzo Greco
Dott. Salvatore Plumari
Dott. Marco Ruggieri

Ciclo XXIX 2013/2016

ABSTRACT

The currently accepted theory that governs the dynamics of quarks and gluons, within the Standard Model of fundamental interactions, is the Quantum Chromodynamics (QCD). Its non-abelian nature provides two important features: while at high energies the interaction becomes small and quarks and gluons interact weakly (asymptotic freedom), at low energies the interaction becomes strong and quarks are confined inside hadrons (color confinement). The asymptotic freedom of QCD implies the existence of a super-dense and ultra-hot form of matter in which the color charged particles are deconfined, the quark-gluon plasma (QGP). Many phenomenological approaches and numerical simulations of the QCD clearly indicate the existence of a transition from the hadronic matter to the quark-gluon plasma at large energy density, $\epsilon \gtrsim 0.5 - 1\,\mathrm{GeV/fm^3}$. Creating and studying the quark-gluon plasma in laboratory is one of the main challenges of experiments at the Large Hadron Collider (LHC) and at the Relativistic Heavy Ion Collider (RHIC). Through ultra-relativistic heavy ion collisions, which generate energies of $0.9-5.5\,\mathrm{TeV}$ per nucleon at LHC and $9-200\,\mathrm{GeV}$ per nucleon at RHIC, one try to get detailed information on the high temperature and low baryon density region of the phase diagram of QCD.

In this thesis we present our study, within the framework of relativistic transport kinetic theory, of the formation and the dynamical evolution of the quark gluon plasma in ultra-relativistic heavy ion collisions. In particular we investigate the time scales and the mechanisms responsible of the isotropization of the fluid produced in the initial out-of-equilibrium stage of the collision, aiming at spotting the impact of this pre-equilibrium phase on collective flows of the bulk matter and on photon observables.

In the first part of this thesis we present our model of the early times dynamics of relativistic heavy ion collisions, in which an initial color-electric field decays to a particle plasma by the Schwinger effect. One of the main novelties of our work consists in the coupling of field evolution to plasma dynamics by solving consistently the classical field equations and the relativistic Boltzmann equation; the self-consistent solution of the problem allows to take into account the backreaction of the color currents on the classical field. We find that the color-electric field experiences a rapid decay for small η/s, in both 1+1D and 3+1D space-time configurations; looking at the ratio of longitudinal over transverse pressure we find that the system acquires a substantial degree of isotropy in less than $1\,\mathrm{fm}/c$ for $\eta/s = 1/4\pi$, in agreement with the common lore of hydrodynamic approaches.

In the second part of this thesis, we extend our approach up to the implementation of a realistic initial condition in which the color-electric field is smoothly distributed in the transverse plane. This configuration, relevant to heavy ion collisions at RHIC and LHC energies, allows to investigate also the effect of the pre-equilibrium dynamics on observables, such as spectrum and elliptic flow of photons emitted from the quark-gluon plasma. To this end we compare the photon production starting from classical color field as discussed above with the standard initial condition of a plasma in thermal equilibrium. We find that the pre-equilibrium stage produces abundantly photons, comparable in num-

ber with those produced by the equilibrated quark-gluon plasma during the whole fireball lifetime. This early contribution enhances the spectrum mainly in a transverse momentum range ($p_T \gtrsim 2 - 3\,\mathrm{GeV}$) where thermal emission becomes less important. The pre-equilibrium phase has an impact also on the photon elliptic flow, since photons coming from the early times evolution of the fireball suppress the contribution to the momentum anisotropy brought by QGP thermal photons.

CONTENTS

INTRODUCTION

The current understanding of the laws which govern the evolution of the Universe from its first moments is based on the symbiosis between the theory of general relativity and the Standard Model of particle physics. The latter describes in a unified way the strong and the electroweak interactions and its validity is supported by a wealth of remarkably precise observations and experiments. Strong, weak and electromagnetic interactions act, through the exchange of mediating bosons, on hadrons and leptons which compose the visible matter in the Universe.

In the '60s Gell-Mann and Zweig developed the quark model, according to which hadrons are not elementary objects but rather aggregates composed of more fundamental particles called *quarks*. Quarks are fermions of spin 1/2 with fractional electric charge and must exist in three colors (a new quantum charge akin to electric charge) in order to explain the observed hadron spectroscopy. Inside hadrons, quarks are held together by the strong interaction, which originate from the exchange of elementary particles called *gluons*. The gluons are massless bosons of spin 1 and, owning colour charge, they can directly interact each other; this is the main difference respect to the electromagnetic interaction among electric charged particle, whose mediating bosons, the photons, do not

possess electric charge and then cannot self-interact, at least at leading order (i.e. directly). This dynamical diversity of the strong interaction causes its richness of interesting peculiarities.

The currently accepted theory that governs the dynamics of quarks and gluons, within the Standard Model of fundamental interactions, is the *Quantum Chromodynamics* (QCD), a Yang-Mills theory based on the color group $SU_C(3)$. The non-abelian nature of QCD provides two important features of the quark-gluon dynamics: while at high energies, or equivalently for small distance, the interaction becomes small and quarks and gluons interact weakly (*asymptotic freedom*), at low energies, or equivalently for large distance, the interaction becomes strong and quarks are confined inside hadrons (*color confinement*).

In the mid '70s the particle physics community realized that the asymptotic freedom of QCD implies the existence of a super-dense and ultra-hot form of matter in which the color charged particles are deconfined, the *quark-gluon plasma* (QGP). Many phenomenological approaches and numerical simulations of the QCD clearly indicate the existence of a transition from the hadronic matter to the quark-gluon plasma at large energy density, $\epsilon \gtrsim 0.5 - 1\,\mathrm{GeV/fm^3}$.

A hot quark-gluon plasma filled the early Universe about $10 - 20\,\mu$s after the Big Bang at low net baryon density and temperatures $T \gtrsim 150\,\mathrm{MeV} \sim 10^{12}\,\mathrm{K}$, five order of magnitude hotter than the center of the Sun. Another natural environment where the quark-hadron transition takes place is the core of supernovae and their remnants, such as neutron stars, where densities $\rho \gtrsim 10^{12}\,\mathrm{Kg/cm^3}$, several times the baryonic density of the normal nuclear matter $\rho_{nm} = 0.16\,\mathrm{fm^{-3}}$, make possible the existence of a cold quark-gluon plasma.

The extreme conditions required for the formation of the quark-gluon plasma are reproduced in particle accelerators by means of high energy nuclear collisions. Creating and studying the quark-gluon plasma in lab-

oratory has been the goal of SPS experiments at CERN, where first signals of the quark-gluon plasma became evident for the first time, and is still one of the main challenges of the experiments ALICE, ATLAS and CMS at Large Hadron Collider (LHC) and the STAR and PHENIX experiments at the Relativistic Heavy Ion Collider (RHIC) at Brookhaven National Laboratory (BNL). Through ultra-relativistic heavy ion collisions, which generate energies of $0.9 - 5.5\,\text{TeV}$ per nucleon at LHC and $9 - 200\,\text{GeV}$ per nucleon at RHIC, one try to get detailed information on the high temperature and low baryon density region of the phase diagram of QCD. Moreover, these experiments are the only possibility to measure observables that give quantitative informations about the properties of the deconfined phase of the QCD.

However, the study of the formation and the evolution of the quark-gluon plasma is a really complicated task, since the observables experimentally accessible concern hadrons, leptons and photons and the properties of deconfined quarks and gluons have to be probed indirectly.
The majority of experimentally measured quantities are hadronic observables, hence the study of the quark-gluon plasma is partially shadowed by the hadronization process that is still not completely understood, especially in a QCD medium; moreover, after their emission hadrons continue to be influenced by the strongly interacting medium suffering further scatterings at hadronic level. Instead photons are radiated during the whole space-time history of the expanding fireball and, due to their electromagnetic nature, once emitted, they leave the system almost undisturbed, reaching the detector with an unaltered imprint of the circumstances of their production; hence, photons are a very intriguing probe for the quark-gluon plasma.

One of the most amazing discoveries of heavy ion physics was that the system created after the collision is a strongly-coupled plasma that exhibits a fluid behaviour with the development of anisotropic collective

flows. Indeed, experiments have observed a large value of the elliptic flow v_2, which is a measure of the azimuthal asymmetry in momentum space and is related to the shear viscosity to entropy density ratio η/s of the matter created in the collision. The evidence that this liquid-like behaviour could be studied within a relativistic hydrodynamic approach, which does not need a detailed description of the microscopic dynamics, paved the way to the idea of the quark-gluon plasma as an *almost perfect fluid* with the smallest shear viscosity to entropy density ratio η/s ever observed in nature. Indeed, the η/s estimated from the collective flows is close to the lower bound $\eta/s = 1/4\pi$ conjectured in the context of supersymmetric Yang-Mills theory in the infinite coupling limit.

Hydrodynamical models provide a good description of the QGP observables, in particular the elliptic flow, in the low transverse momentum region and in the central rapidity range, where the local kinetic equilibrium assumed by hydrodynamics is plausible. However, hydrodynamics formulations, even those including viscous effects, have a limited range of validity in momentum space, in particular for the relatively large viscosities that could be envisaged at the initial high temperatures ($T \simeq 500\,\mathrm{MeV}$) and in the crossover region of the quark-hadron transition. Moreover, hydrodynamic models lose their power when they try to describe phenomena not related to the collective behaviour of the plasma as well as out-of-equilibrium processes like those affecting the system in the very early stages of relativistic heavy ion collision.

An alternative approach capable to study the evolution of the quark-gluon plasma is based on transport kinetic theory. Solving the relativistic Boltzmann-Vlasov equation for the one-body phase space distribution function $f(x, p)$, one can follow the whole space-time evolution of the system produced in high-energy heavy ion collisions, treating in a more suitable framework non-equilibrium states and relaxation toward the equilibrium. While in hydrodynamical formulations the dynamical

evolution is governed by macroscopic quantities, transport theory is a microscopic description of the system in terms of parton distribution functions and the dissipative effects produced by a finite viscosity are treated by means of a collision term with finite cross sections, accounting for the short range interaction between partons. Although inputs of kinetic models are usually microscopic details of fields and cross sections of a given set of microscopic processes, we perform transport simulation at fixed η/s in order to make a more direct link to viscous hydrodynamics. In other words we obtain in the limit of short mean free path an hydrodynamical description but starting from the one-body distribution function instead that from the energy-momentum tensor.
Transport models successfully reproduce hydrodynamical calculations for the elliptic flow in the low p_T region and supply a more reliable approach to describe the elliptic flow for intermediate and high transverse momenta. Moreover, kinetic theory, as we will show in this thesis, allow to investigate the non-equilibrium effects of the early times dynamics of ultra-relativistic heavy ion collisions and to follow the subsequent evolution of the fireball within a unified theoretical framework.

In this thesis we will present our study, within the framework of relativistic transport kinetic theory, of the formation and the dynamical evolution of the quark gluon plasma in ultra-relativistic heavy ion collisions. In particular we investigate the time scales and the mechanisms responsible of the isotropization of the matter produced in the initial out-of-equilibrium stage of the collision, aiming at spotting the impact of this pre-equilibrium phase on observables such as photon production and elliptic flows.

The understanding of early times dynamics and of thermalization and isotropization mechanisms that lead to the formation of an equilibrated quark-gluon plasma is one of the most interesting and challenging open issue in ultra-relativistic heavy ion collisions. In the standard initial

picture of such nuclear collisions, immediately after the two nuclei had passed one through each other, a peculiar configuration of strong longitudinal color-electric and color-magnetic coherent fields named *glasma* is produced; as the system expands quantum fluctuations, amplified by plasma instabilities, cause the decay of the glasma to a parton liquid which locally isotropizes and thermalizes in $\tau_{eq} \lesssim 1\,\mathrm{fm}/c$, a scenario in agreement both with calculations based on transport theory and hydrodynamic models. While in the great majority of those studies the plasma equilibration is an initial state assumption for simulations of relativistic heavy ion collisions, investigating how it is achieved in a very short time by an initial anisotropic and not thermalized system is one of the main goals of this thesis. Besides plasma instabilities, a possible mechanism causing initial field decay and quark-gluon plasma production is the Schwinger effect, which consists of a vacuum instability towards the creation of particle pairs by a strong electric field. First introduced in the context of quantum electrodynamics, the Schwinger formation of pairs in strong fields has been generalized for color-electric and color-magnetic fields and in the last forty years has been considered as a mechanism for color field decay and particle production in the framework of quark-gluon plasma physics.

In the first part of this thesis we will present our model of early times dynamics of the system produced in relativistic heavy ion collisions by an initial color-electric field which then decays to a plasma by the Schwinger effect. This means that we start from a color field configuration such that the ratio of longitudinal to transverse pressure $P_L/P_T = -1$, i.e. very far from the equilibrium condition $P_L/P_T = 1$. Our study is the first in which a Monte Carlo method is used to simulate the Schwinger effect in the context of high-energy collisions. Another of the main novelties of our work consists in the coupling of field evolution to plasma dynamics by solving consistently the classical field equations and the relativistic

Boltzmann equations; the self-consistent solution of the problem allows to take into account the backreaction of the color currents on the classical field, which has been often neglected in previous studies. Moreover, with respect to previous work where the relaxation time approximation is used to simplify the collision integral in the Boltzmann equation, we do not resort to such an approximation, but solve the relativistic kinetic equation with the full collision integral.

We will see that the color-electric field experiences a rapid decay for small η/s, in both 1+1D and 3+1D space-time configurations; looking at the ratio of longitudinal over transverse pressure P_L/P_T, we will show that the system acquires a substantial degree of isotropy in less than $1\,\mathrm{fm}/c$ for $\eta/s = 1/4\pi$, in agreement with the common lore of hydrodynamic approaches. For larger values of viscosity, the pressure ratio exhibits several oscillations, following those of the color field, and its asymptotic value is quite smaller than 1 meaning that the parton fluid does not isotropize.

Furthermore, the implementation of the three-dimensional expansion makes possible the study of the elliptic flows v_2; indeed, starting from an azimuthally anisotropic distribution of a pure color field, we are able to follow the development of collective flows during the system expansion within a single consistent scheme.

In the second part of this thesis, we extend our approach up to the implementation of a realistic initial condition in which the color-electric field is still along the beam direction but with strengths smoothly distributed in the transverse plane. This configuration, reproducing the initial multiplicity and spatial anisotropy of particle created in collisions at RHIC and LHC energies, allow to investigate also the effect of the pre-equilibrium dynamics on photon observables experimentally measured. We will discuss our results on the spectrum and the elliptic flow of photons emitted from the quark-gluon plasma produced in heavy ion collisions. There are

different sources of *direct photons* (i.e. those emerging directly from collision processes and not from hadronic decays), depending of their origin from different stages of the expanding fireball formed after the collision. Experiments can not distinguish between the different categories, hence theoretical models are necessary to identify these sources and their relative importance in the spectrum. In particular, with our approach we are interested in investigating the properties of pre-equilibrium photons and grasping their effect on direct photon spectrum and elliptic flow observed in ultra-relativistic heavy ion collision experiments.
Our main aim is to study the possible impact of the pre-equilibrium phase on the final photon production. To this end we compare the photon production starting from classical color field at $\tau_0 = 0^+$, as discussed above, with the standard initial condition of a plasma in thermal equilibrium expanding from $\tau_0 = 0.3 - 0.6\,\mathrm{fm}/c$.

We will show that the pre-equilibrium stage produces abundantly photons, comparable in number with those produced by the equilibrated quark-gluon plasma during the whole fireball lifetime. This early contribution enhances the spectrum mainly in a transverse momentum range ($p_T \gtrsim 2 - 3\,\mathrm{GeV}$) where thermal emission becomes less important. The pre-equilibrium phase has an impact also on the photon elliptic flow v_2 since photons coming from the early times evolution of the fireball suppress the contribution to the momentum anisotropy brought by QGP thermal photons.

The thesis is structured as follows. In Chapter 1 we will present the general features of QCD and the phase transition the ordinary matter experiences under extreme conditions. In chapter 2 we will describe the geometry and the dynamics of ultra-relativistic heavy ion collisions and the main probes and observables of the formation and the evolution of the quark gluon plasma. In Chapter 3 we will discuss transport Boltzmann equation from its classical formulation to the quantum-relativistic

generalization; then we will explain its numerical implementation. In Chapter 4 we will describe our model of the early times dynamics in which an initial color-electric field decays to a particle plasma through the Schwinger mechanism; then we will discuss our results in the cases of both the 1+1D and the 3+1D expanding system. In Chapter 5 we will present our results on the impact of the pre-equilibrium dynamics on bulk matter properties and on photon observables.

CHAPTER 1

QUANTUM CHROMODYNAMICS AND ITS DECONFINED PHASE

Quantum Chromodynamics (QCD) is a quantum-relativistic field theory which to current knowledge describes the dynamics of quarks and gluons, the only elementary particles subject to the strong interaction. It is a gauge theory constructed in analogy to the theory of electromagnetic interactions, Quantum Electrodynamics (QED), but it differs from QED in its non-Abelian nature, which provides peculiar features such as confinement and asymptotic freedom. QCD is part of a wider theory called the Standard Model (SM) of particle physics, which describes strong, weak and electromagnetic interactions and whose validity is supported by a large number of remarkably precise experimental tests.

1.1 Quantum Chromodynamics

1.1.1 Quarks and gluons in the Standard Model

So far as we know, all of the interactions between objects in our Universe occur through only four fundamental forces. Besides electromagnetic and gravitational forces, which we experience continuously in

our lives and therefore mankind began to investigate very early, there are other two forces, called the weak and the strong interaction, which act over very short distances and are confined to the scale of atomic nuclei. The strong interaction holds quarks together to form protons and neutrons at the energy densities of normal nuclear matter; nevertheless the peculiar features of strong interaction at very high energies make possible the existence of a new and strange form of matter that have attracted a lot of interest in the scientific community in last decades and is the subject of this thesis.

The Standard Model Lagrangian $\mathcal{L}_{SM}$ embodies our knowledge of strong, weak and electromagnetic interactions. It contains as fundamental degrees of freedom the spin one-half quarks and leptons, the spin one gauge bosons and the spin zero Higgs fields. Symmetry plays the central role in determining its dynamical structure: the Lagrangian exhibits invariance under $SU(3)_C \otimes SU(2) \otimes U(1)_Y$ gauge transformations.

In the Standard Model, the fundamental fermionic constituents of matter are the quarks and leptons. These particles are considered as truly elementary, because there is no experimental evidence of their compositeness, such as excited states or form factors associated with intrinsic structure. Both quarks and leptons have spin 1/2 and have electromagnetic charge, but only quarks own color charge; as a consequence, quarks suffer also strong interactions via the exchange of gluons, the gauge bosons associated to the $SU(3)_C$ symmetry group, i.e. the non-Abelian group of local phase rotations of the fields in the color space. The concept of color, as well as the quantum dynamics of color, was first proposed by Nambu in 1966 and the theory is now called *Quantum Chromodynamics*. Quarks exists in six flavours, u, d, s, c, b, t (*up*, *down*, *strange*, *charme*, *bottom*, *top*) in order of increasing mass. u, c and t quarks have electric charge $Q = 2e/3$, while d, s and b quarks have $Q = -1e/3$. Each quark flavour q has a correspondent antiquark $\bar{q}$ with opposite electric charge.

Each species of quark may have $N_C = 3$ different colours, conventionally called red, green and blue; the anti-quarks carry one unit of anti-color. Gluons have spin 1 and carry a non-neutral combination color/anti-color which leads to the existence of a gluon octet. The hadrons observed experimentally are all "colourless" bound states: they may be a composition of three quarks (antiquarks), named baryon (antibaryon), or a quark-antiquark pair, called meson. Data on exotic hadrons containing more quarks (tetraquaks and pentaquarks) exist and are currently under study. The fact that gluons, as force carriers, carry color charge make them able to interact with each other, as opposed to photons which carry no charge with respect to the interaction they mediate (they do not own electric charge).

1.1.2 QCD Lagrangian

QCD is a quantum theory but we may consider its classical formulation, the *Yang-Mills theory* for classical quark and gluon fields, to figure out many essential aspects.

The classical Lagrangian density of QCD is given by

$$\mathcal{L}_{cl} = \bar{q}_i^{\alpha} \left(i\gamma^{\mu} D_{\mu} - m\right)^{ij}_{\alpha\beta} q_j^{\beta} - \frac{1}{4} F^a_{\mu\nu} F_a^{\mu\nu}, \tag{1.1}$$

where q_i^{α} is the quark field with colour $\alpha = 1, 2, 3$ and flavour $i = 1, \ldots, N_f$, m is the mass matrix, which is color-independent and diagonal in the flavour space $m = \delta_{\alpha\beta}\,\mathrm{diag}(m_u, m_d, \ldots, m_t)$, and γ^{μ} are the Dirac matrices. D_{μ} is the covariant derivative acting on the color-triplet quark field and is defined

$$D_{\mu} = \partial_{\mu} + igt^a A^a_{\mu},$$

where A^a_{μ} $(a = 1, \ldots, 8)$ is the gluon field, g is the QCD dimensionless coupling constant (akin to the QED electric charge e) and t^a $(a = 1, \ldots, 8)$ are the generators of the fundamental representation of the Lie

algebra $SU(3)_C$, which satisfies the following commutation relation:

$$[t^a, t^b] = i f_{abc} t^c, \tag{1.2}$$

being f_{abc} the structure constant of the $SU(3)_C$ group. The covariant derivative acting on the color-octet gluon field is defined

$$\mathcal{D}_\mu = \partial_\mu + igT^a A^a_\mu, \tag{1.3}$$

where T^a $(a = 1, \ldots, 8)$ are the generators of the adjoint representation of the $SU(3)_C$ algebra given by $(T_a)_{bc} = -if_{abc}$.

The strength tensor of the gluon field is

$$F^a_{\mu\nu} = \partial_\mu A^a_\nu - \partial_\nu A^a_\mu - g f_{abc} A^b_\mu A^c_\nu;$$

defining $A_\mu \equiv t^a A^a_\mu$ and $F_{\nu\mu} \equiv t^a F^a_{\nu\mu}$, it may be written in a more compact way

$$F_{\mu\nu} = -\frac{i}{g}[D_\mu, D_\nu].$$

Color electric and color magnetic fields may be defined from $F^{\mu\nu}$ in analogy to the electromagnetic ones:

$$E^i = F^{i0}, \qquad B^i = -\frac{1}{2}\varepsilon_{ijk} F^{jk}, \tag{1.4}$$

where ε_{ijk} is a complete antisymmetric tensor with $\varepsilon_{123} = 1$.

The langrangian density so far introduced is invariant under a generic local transformation of the $SU(3)_C$ group

$$V(x) = \exp(-i\theta^a(x) t^a);$$

as a consequence quark and gluon fields transform as follows:

$$q(x) \to V(x) q(x), \qquad A_\mu(x) \to V(x) \left(A_\mu(x) - \frac{i}{g}\partial_\mu \right) V^\dagger(x).$$

Due to gauge invariance terms like $A^a_\mu A^\mu_a$ are forbidden in the Lagrangian, hence gluons are massless particles. The term $-m\bar{q}^\alpha_i q^i_\alpha$ does not break gauge invariance and therefore finite quark masses are allowed.

Applying the variational principle to the Lagrangian (1.1) classical equation of motion are obtained, that is the Dirac equation for quark fields

$$(i\gamma^\mu D_\mu - m)q = 0 \tag{1.5}$$

and the Yang-Mills equation for gluon fields

$$[D_\nu, F^{\nu\mu}] = gj^\mu,$$

where $j^\mu = t^a j^\mu_a$ e j^μ_a is the vector current of the fermionic field and is given by

$$j^\mu_a = \bar{q}\gamma^\mu t^a q. \tag{1.6}$$

In order to better understand the properties of the classical Lagrangian (1.1), we can decompose it into its different pieces:

$$\begin{aligned}\mathcal{L}_{cl} =& \bar{q}^\alpha_i (i\gamma^\mu \partial_\mu - m)^{ij}_{\alpha\beta} q^\beta_j - \frac{1}{4}(\partial_\mu A^a_\nu - \partial_\nu A^a_\mu)(\partial^\mu A^\nu_a - \partial^\nu A^\mu_a) \\ & - g\bar{q}^\alpha_i \gamma^\mu t^a_{\alpha\beta} A^a_\mu q^\beta_i \\ & + \frac{g}{2} f^{abc}(\partial_\mu A^a_\nu - \partial_\nu A^a_\mu) A^\mu_b A^\nu_c - \frac{g^2}{4} f_{abc} f^{ade} A^b_\mu A^c_\nu A^\mu_d A^\nu_e,\end{aligned}$$

whose diagrammatic representation is shown in Fig. 1.1.

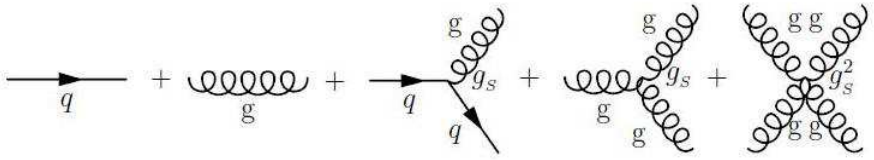

Figure 1.1: Feynman diagrams representing quark and gluon propagators and the three QCD interaction vertices.

The first line contains the kinetic terms for the gluon and the quark fields, which give rise to the corresponding propagators. The colour interaction between quarks and gluons is given by the second line. Finally, owing to the non-Abelian character of the colour group, the product $F^a_{\mu\nu} F^{\mu\nu}_a$ generates the self-interaction terms corresponding to three-gluon and four-gluon vertices shown in the last line. The strength of

all these interactions is given by a single universal coupling g_s, which is called the *strong coupling constant*. As already said, the existence of self-interactions among the gauge fields is a new feature which is not present in QED; it seems then reasonable to expect that these gauge self-interactions could explain properties like asymptotic freedom and confinement, which do not appear in QED.

The strength of the strong interaction is measured by the strong coupling constant $\alpha_s = g_s^2/4\pi$, which is similar to the fine structure constant of QED but has a different behaviour in function of the energy that will be explained in the next section.

1.1.3 Confinement and asymptotic freedom

Baryons and mesons are described by the colour–singlet combinations:

$$B = \frac{1}{\sqrt{6}}\epsilon^{\alpha\beta\gamma}|q_\alpha q_\beta q_\gamma\rangle, \qquad M = \frac{1}{\sqrt{3}}\delta^{\alpha\beta}|q_\alpha \bar{q}_\beta\rangle, \tag{1.7}$$

where α, β, γ indicate the color quantum number. In order to avoid the existence of non-observed extra states with non-zero colour, one needs to further postulate that all asymptotic states are colourless, i.e. singlets under rotations in colour space. This assumption is known as the *confinement* hypothesis, because it implies that free quarks can not be observed: since quarks carry colour they are confined within colorless bound states.

The running coupling constant of QCD, which can be derived renormalizing the theory[1], is:

$$\alpha_s(\kappa) = \frac{g^2}{4\pi} = \frac{1}{4\pi\beta_0 ln(\kappa^2/\Lambda^2_{QCD})}, \tag{1.8}$$

where the first coefficient of the QCD beta function

$$\beta_0 = \frac{1}{48\pi^2}(11N_c - 2N_f) \tag{1.9}$$

[1]The bare charge g and m entering the QCD Lagrangian are not physical values. The transition from the bare parameters to physical ones, i.e. to the quantities that can be (at least in principle) experimentally measured, is called renormalization.

is independent by the chosen renormalization scheme. In (1.8) Λ_{QCD}, called *QCD scale parameter*, is independent from the renormalization point κ and have to be experimentally determined. In order to estimate its value we need to specify the renormalization scheme used and the number of active quark flavours; for example, within the $\overline{MS}$ scheme for $N_f = 5$ we obtain $\Lambda_{QCD} = (217 \pm 24) MeV$ [1].

The negative contribution in (1.9) proportional to the number of quark flavour N_f is due to quark-antiquark loops and is similar to the QED result which corresponds to a screening of the interaction, which decreases with increasing energy or, equivalently, with decreasing distances. The gluonic self-interaction introduces an additional positive contribution proportional to the number of colors N_c which is responsible of the completely different behaviour of QCD with respect to QED. Indeed (1.9) is positive for $N_f \leq 5N_c$, condition satisfied by QCD, and from Eq. (1.8) follows that the QCD running coupling constant decreases with increasing κ, leading to the characteristic *asymptotic freedom* of QCD demonstrated in 1973 by Gross, Wilczek and Politzer [2] [3–5].

The electromagnetic coupling constant increases with increasing energy. Moreover, the larger the distance between electric charges, the weaker is the interaction due to the creation from the vacuum of electron-positron pairs (vacuum polarization) which screen the charges generators of the electromagnetic field. In QCD this screening is still present due to vacuum creation of quark-antiquark pairs, but gluonic self-interaction generates a further screening effect. In agreement with Eq. (1.9) the net effect is opposite and is named *antiscreening*.

Therefore, the QCD coupling constant becomes greater at low energy or large distances. This is a hallmark of the QCD confinement. In fact, the phenomenological potential between a quark and an antiquark in-

[2] Gross, Politzer and Wilczek won the 2004 Nobel Prize in physics "for the discovery of asymptotic freedom in the theory of the strong interaction" [2].

creases linearly with increasing distance between them: moving apart color charges becomes more difficult for larger separation distance. Indeed, over a critical separation the potential energy becomes big enough to create a new quark-antiquark pair from vacuum. In this way, quarks are always confined inside hadrons and can never find isolated. The non-observation of isolated quarks and gluons leads to postulate that only aggregates of quarks and gluons with zero total color charge have finite energy, while colored compounds should have infinite energy. Thus their absence is explained. Colour confinement is a consequence of QCD generally accepted but has never been established in rigorous way.

From Eq. (1.8) we see that the running coupling constant decreases logarithmically with increasing κ. When $\kappa \gg \Lambda_{QCD}$, $\alpha_s(\kappa) \to 0$ and the use of perturbation theory is justified. At lower energy the coupling constant becomes greater and perturbation theory is no more valid. For $\kappa \to \Lambda_{QCD}$, $\alpha_s(\kappa) \to \infty$; hence Λ_{QCD} indicates the energy scale at which the strong coupling constant diverges.

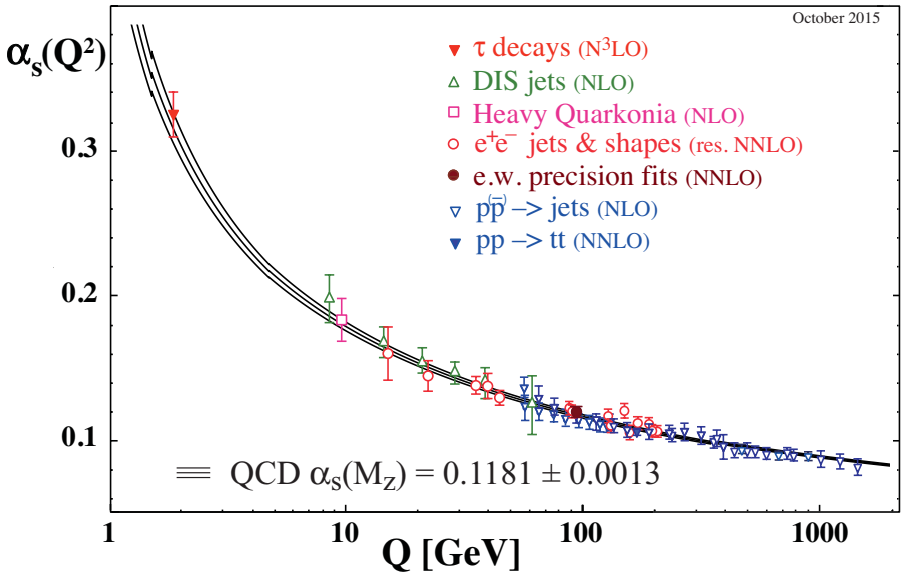

Figure 1.2: Summary of measurements of α_s as a function of the energy scale Q. The respective order of QCD perturbation theory used in the extraction of α_s is indicated in brackets. The figure is adapted from [6].

Fig. 1.2 shows the QCD effective coupling constant $\alpha_s(Q^2)$ determined through several experiments at discrete energy scales Q, including results up to N^{3}LO (next-to-next-to-next-to leading order). Thanks to the results from the Tevatron and from the LHC, the energy scales at which α_s is determined now extend up to more than 1 TeV. There is a clear signature and proof of the energy dependence of α_s, in full agreement with the QCD prediction of asymptotic freedom. Typical values of $\alpha_s(\kappa)$ are:

$$\alpha_s(100\,GeV) \simeq 0.12, \qquad \alpha_s(10\,GeV) \simeq 0.18, \qquad \alpha_s(2\,GeV) \simeq 0.30.$$

We can get an intuitive picture of the features of QCD that lead to the confinement and to the asymptotic freedom assimilating the interaction between a $q\bar{q}$ to some kind of rubber band [7]. If we try to separate the quark form the antiquark the force joining them increases. At some point, the energy on the elastic band is larger than $2mq'$, so that it becomes energetically favourable to create an additional $q'\bar{q}'$ pair; then the band breaks down into two mesonic systems, $q\bar{q}'$ and $q'\bar{q}$, each one with its corresponding half-band joining the quark pair. Increasing more and more the energy, we can only produce more and more mesons, but quarks remain always confined within colour–singlet bound states. Conversely, if one tries to approximate two constituent quarks into a very short-distance region, the elastic band loses the energy and becomes very soft: quarks behave then as free particles.

1.1.4 Non perturbative approaches to QCD

We have seen that the QCD effective coupling constant $\alpha_s(\kappa) = g_s^2/4\pi$ decreases with increasing energy. Therefore at high temperatures it is possible to study QCD within the perturbation theory. Although this approach allows to understand at least in a qualitative way some characteristics of quark-gluon plasma, it does not reveal the physics of a phase

transition which is inherently non-perturbative. Furthermore perturbation theory breaks down even at extremely high temperatures, because of the so-called *infrared problem*: one can not calculate corrections to pressure and self-energy in any order in g_s, but encounter serious mathematical difficulties already at $O(g_s^6)$ for the pressure and $O(g_s^4)$ for the self-energy [8].

A powerful method that overcomes the limits of perturbation theory is the *lattice QCD* (lQCD), which has been increasingly used and largely developed in recent years. This approach is highly efficient because, discretizing the QCD action on a space-time grid, one can make numerical simulations computing many interesting quantities of strongly interacting systems, such as pressure and energy density, and then the equations of state of hadronic and QGP phases [9–11].
However, besides the obstacles imposed by the limited computing power of modern computers, it is not possible at the moment to implement on a grid a system of quarks and gluons with finite chemical potential, due to the Fermi-Dirac statistics of the quarks. Nevertheless, the low-density region of the phase diagram can be investigated with alternative techniques, such as the Taylor expansion of thermodynamic quantities around zero chemical potential and the analytical continuation from imaginary chemical potentials [12–17].
Therefore it is important to resort also to other approaches in order to study the non-perturbative regime of QCD and explore the full structure of the phase diagram. To this end, various low-energy effective theories and phenomenological models were proposed, such as the MIT bag model, the hadron resonance gas model, chiral perturbation theory, the Nambu-Jona-Lasinio (NJL) model, the quark-meson (QM) model and Polyakov-loop extended versions of the NJL and QM models, which are able to describe many aspects of QCD reproducing some of its global symmetries.

1.2 QCD matter under extreme conditions

In the 1970s, first speculations about possible new states of matter at densities over the normal nuclear one [18, 19] and then also the insight that the structure of matter should become simple at high temperatures [20–23] began to motivate new theoretical and experimental researches to investigate the properties of nuclear matter at ultra-high energy densities.

As we have seen, the principle of asymptotic freedom states that the effective QCD coupling constant α_s falls with increasing momentum transfer q^2 or, equivalently, with decreasing distance between particles. In a thermal medium, the characteristic momentum transfer between massless particles is of order the temperature T, and thus the effective coupling between quarks and gluons must become weak when T becomes large. The complicated structure of nuclear matter at low temperatures, at which it is composed of hadronic particles, was thus expected to give rise at high temperatures to a relative simple plasma composed of weakly interacting quarks and gluons, called *quark-gluon plasma* [24–28].

A rough estimation of the deconfinement transition temperature can be obtained using the bag model: one can calculate the pressure depending on the degrees of freedom in a hadron gas and in the QGP and a phase transition occurs when the pressures become equal. The degrees of freedom for a gas of massless pions are 3, while for a QGP with $N_f = 2$ they are 16 for the gluons and 24 for quarks and antiquarks. Equating the resulting pressures leads to a transition temperature $T_c \approx 160\,\mathrm{MeV}$ at zero quark chemical potential. This corresponds to an energy density of $\epsilon \approx 1\,\mathrm{GeVfm}^{-3}$, about 7.5 times that of normal nuclear matter ($\epsilon_0 \approx 0.135\,\mathrm{GeVfm}^{-3}$). This value is close to the "limiting" temperature of matter composed of hadrons first postulated by Hagedorn and defined as the exponential slope of the mass spectrum of hadronic resonances [29].

In order to obtain more accurate information about the transition

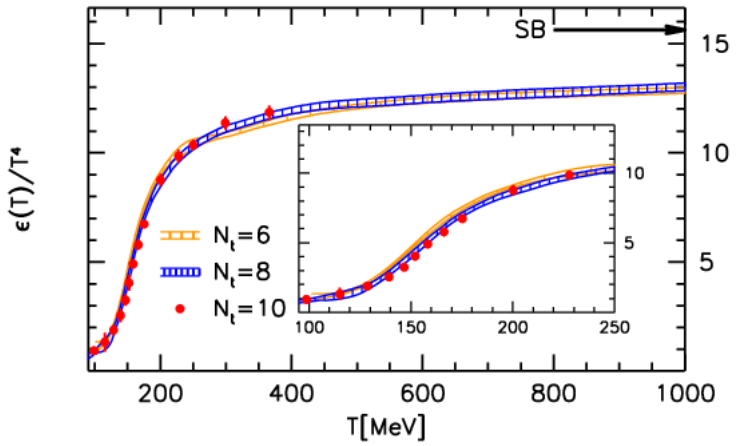

Figure 1.3: Temporal evolution of the energy density scaled by T^4 from lattice QCD calculations with $N_f = 2 + 1$ flavors (u, d and s quarks). The figure is adapted from [9].

temperature and the equation of state of QCD matter in the different temperature domains, one have to resort to exact calculations of the energy density by means of lattice QCD. Such computations show that there is a rapid rise of the energy density $\epsilon(T)$ of matter when the temperature reaches $T \approx T_c \sim 155\,\text{MeV}$, really close to the value found using the bag model. The energy density changes about an order of magnitude in a narrow range of temperatures $\Delta T \sim 10 - 20\,\text{MeV}$ as can be seen from Fig. 1.3. This rapid rise can be explained as a change in the degrees of freedom between the confined and deconfined phases, since the energy density is roughly proportional to the number of degrees of freedom.

1.2.1 Quark gluon plasma in nature

Understanding the properties of elementary particles at high temperature and density is one of the main goals of theoretical and experimental researches in contemporary physics. Through the study of properties of elementary particle matter exposed to such extreme conditions we hope to learn about the equation of state that controlled the evolution of the early Universe as well as the structure of compact stars.

QGP in the early Universe

While the history of the Universe after its first second is now tested by high quality observations of light element abundances and temperature anisotropies of the cosmic microwave background, the era of the first second is the less known and maybe more interesting. The Standard Model of particle physics predicts two transitions that occurred in that epoch after the inflation, a brief but violent period in which the Universe underwent an exponential expansion. The first transition happened at a temperature $T \sim 200\,\mathrm{GeV}$ and is responsible for the spontaneous breaking of the electroweak symmetry, which gives the masses of the elementary particles. The second transition, occurred at $T \sim 150\,\mathrm{MeV}$ about $10^{-5}\,\mathrm{s}$ after the Big Bang, is the quark–hadron transition: quarks and gluons condense to form a gas of nucleons and light mesons (the latter decayed subsequently). At the end of the first second, neutrinos and neutrons decouple from the radiation fluid. The quark–hadron transition and dissipative processes during the first second prepare the initial conditions for the synthesis of the first nuclei.

The QCD phase transition is the most dramatic event in that epoch because it correspond to a reduction of about a factor three in the number of degrees of freedom, as previously shown in Fig. 1.3. The impact of the QCD transition in the evolution of the Universe is evident in Fig. 1.4, where the effective number of relativistic helicity degrees of freedom as a function of the temperature are plotted. The two full lines show the effective degrees of freedom of the energy density g_ϵ and of the entropy density g_s (upper line) for the particle content of the Standard Model [30]. The rise of g starting at around 30 MeV is mainly due to muons and pions, but also heavier hadrons can be excited. At the temperature of the QCD transition (160 MeV in the figure) the number of degrees of freedom changes very rapidly, since quarks and gluons are coloured. At still higher temperatures again heavier particles are excited, but within

the SM of particle physics nothing spectacular happens, the electro-weak transition is only a tiny effect.

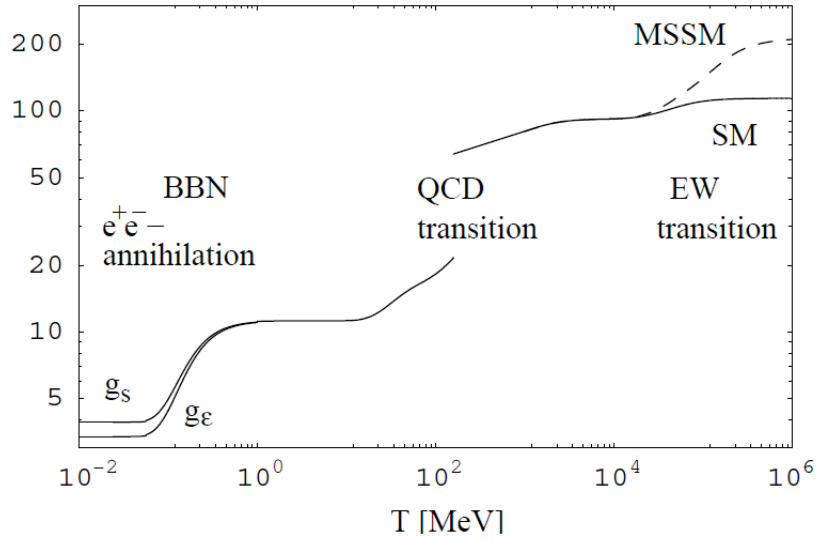

Figure 1.4: The effective number of degrees of freedom as a function of temperature. The full line is the prediction of the Standard Model of particle physics, the dashed line shows a Minimal Supersymmetric extension of the Standard Model. The figure is adapted from [30].

Quark matter in compact stars

Nuclear matter in deconfined phase can also be found in the core of super-dense stars, such as neutron stars and quark stars. Neutron stars are composed mainly of neutrons, with some protons and electrons. If the density in the centre of neutron stars reaches $5-10\,\rho_{nm}$, the gravitational collapse of stellar matter generates pressures comparable to what is required for the formation of QGP [31]: neutrons may dissolve into a hot plasma of quarks, with an almost equal number of quark u, d and s (the so-called strange matter), and this state of matter could be stable, making possible the existence of stars entirely made of strange matter, the quark stars.

Thus, the interior of neutron stars is a possible place in which QGP

may exist in condition of non-zero chemical potential and low temperature, a completely different region of the QCD phase diagram respect to the area of interest for the early Universe.

1.2.2 Exploring the QCD phase diagram in laboratory

The extreme constraints of temperature and density energy make the quark-gluon plasma quite rare in nature. On Earth we are limited to study this new state of matter in laboratory, producing the so-called "Little Bang", i.e. colliding heavy ions accelerated at speeds close to the speed of light. After the collision, the two nuclei deposit an enormous amount of energy inside a relatively small volume, thus creating the desired extreme conditions of temperature and density for a short time of order $10^{23} - 10^{22}$ s.

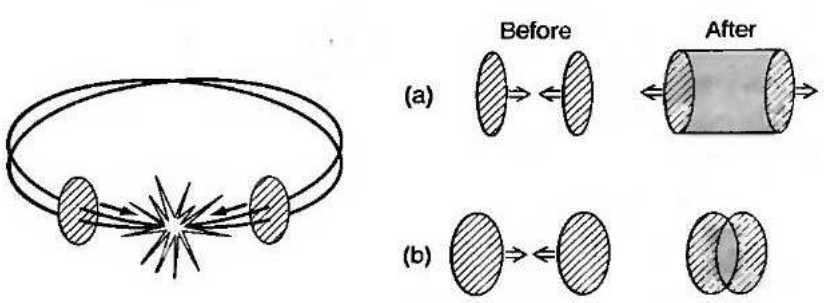

Figure 1.5: QGP formation at high temperature (a) and at high baryon density (b). Figure adapted from [32].

A large experimental program is devoted to the study of hot and dense matter created in relativistic heavy ion collisions. Suppose to accelerate two heavy nuclei (gold or lead ions for example) up to relativistic or ultra-relativistic energies and to cause a frontal collision, as shown in Fig. 1.5. At these energies, nuclei are similar to "pancakes" due to Lorentz contraction. When the center-of-mass energy per nucleon exceeds $5 - 10$ GeV, the colliding nuclei tend to pass through each other and while

they move away matter with low baryon density is formed between them at high energy density and temperature (Fig. 1.5 (a)). This is what happens at the Relativistic Heavy Ion Collider (RHIC) at Brookhaven National Laboratory (BNL) and the Large Hadron Collider (LHC) at CERN in Geneva. When the energy per nucleon is lower, the colliding nuclei tend to stick together (Fig.1.5 (b)); in this case one can achieve moderately high temperatures, $T \lesssim 150\,\mathrm{MeV}$, and large baryon density, $\rho \sim 4\rho_{nm} = 0.64\,\mathrm{fm}^{-3}$.

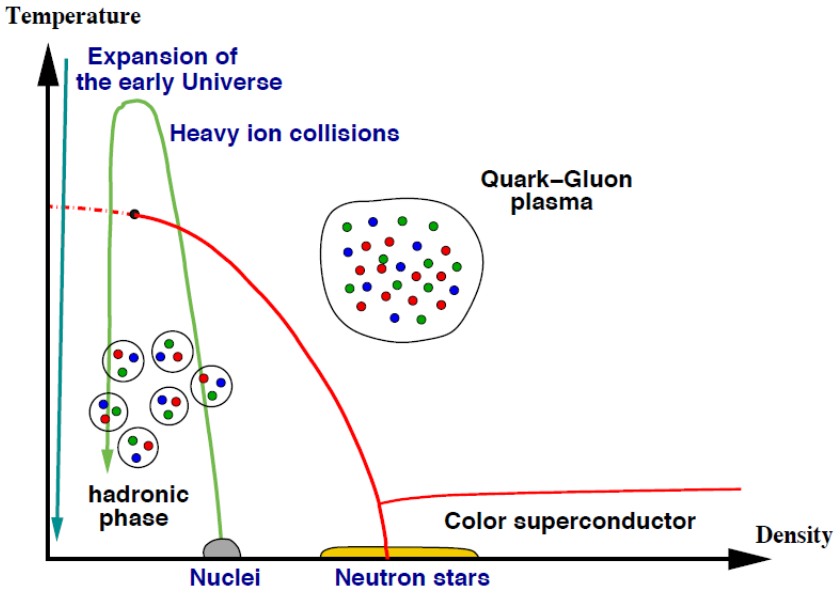

Figure 1.6: Schematic representation of the phase-diagram in QCD at finite temperature and non-zero quark density, as emerging from lattice calculations at zero (or small) quark density and from various theoretical considerations (like pQCD) in the other domains. The figure is adapted from [33].

Heavy ion collisions at different energies along with theoretical models allow to investigate the phase diagram of QCD, obtained varying the temperature T and the net quark density (or the quark chemical potentials μ_f), i.e. the difference between the density of quarks and that of the antiquarks. Fig. 1.6 is a cartoon of expected QCD phase diagram. It has been actually demonstrated only in special corners, like the decon-

finement phase transition with increasing T at zero (or small) density, that has been established on the lattice, and the areas denoted as 'nuclei' or 'neutron stars', which are rather well understood within nuclear theory. The 'colour superconductor' phase is a state of nuclear matter at high quark density predicted by perturbative QCD. The collision process at relativistic energies (case (a) of Fig. 1.5) is illustrated as the green curve in Fig. 1.6, which starts from the hadronic matter (nuclei), rises in temperature with low net baryon density into the QGP phase and then returns to the hadronic phase.

The possible phases of QCD and the precise location of the critical points are currently under investigation. Discovering and understanding the phase structure of QCD is one of the main purposes of the present and future theoretical and experimental research in the field of QCD under extreme conditions.

CHAPTER 2

QUARK-GLUON PLASMA IN HEAVY ION COLLISIONS

In the previous chapter we have seen that Quantum Chromodynamics (QCD) provides two important features of the dynamics of quarks and gluons. At low energy they are never observed as isolated particles but according to confinement may exist only in the form of neutral color objects, the hadrons, which are therefore the relevant degrees of freedom. High-energy perturbation theory applied to QCD predicts that because of asymptotic freedom the strong interactions between partons, i.e. quarks and gluons, become weak, hence they become the effective degrees of freedom. This new state of matter is called *quark-gluon plasma* (QGP).

The extreme conditions of temperature and density energy make this state of matter quite rare in nature. As explained in Chapter 1, it is thought to have fulfilled the Universe in the earliest moments after the Big Bang when the temperature was about five order of magnitude hotter than the center of the Sun, as well as to exist in the present day in the core of certain compact celestial objects such as neutron stars where the gravitational collapse of stellar matter produces pressures comparable to what is required for the formation of QGP.

Heavy ion collisions are the only way we can study in laboratory the properties of nuclear matter under extreme conditions, in the early stage of collisions between heavy nuclei accelerated at speeds close to the speed of light.

After a brief mention of past and present heavy ion colliders, an overall description of the geometry and dynamics of relativistic nuclear collisions will be given and then the more relevant experimental facts accumulated up to now and the main signature of the QPG will be introduced.

2.1 Heavy ion experiments

The first experiments with heavy ions at relativistic energies of 10 GeV per nucleon took place at Berkeley Bevalac at the beginning of 80s and continued towards the end of the decade at the Brookhaven National Laboratory (BNL) and at the European Organization for Nuclear Research (CERN). The Alternating Gradient Synchroton (AGS) at BNL accelerated beams up to ^{28}Si at 14 GeV per nucleon while at CERN the Super Proton Synchroton (SPS) accelerated ^{16}O at 60−200 GeV per nucleon. In 1995 SPS started to accelerate ^{208}Pb at 158 GeV per nucleon. These experiments sanctioned the beginning of ultra-relativistic heavy ions collisions (uRHICs) era.

In 2000 the first data from the Relativiatic Heavy Ion Collider (RHIC) at BNL were collected accelerating ^{197}Au ions at 200 GeV per nucleon. On February 10 of that year the SPS experiment announced the creation and observation of a new state of matter consistent with the QGP [34]. This observation has been recreated and verified by RHIC [35]. The experiments at RHIC have provided a large amount of observables that allowed to start a quantitative study of the QGP features [36–39].

RHIC collides two beams of heavy ions, each with an energy up to 100 GeV per nucleon. At top energy, the initial temperature reached in collisions between two gold nuclei is inferred to lie between 300 and 400 MeV

[40], well above the QCD phase-transition temperature of about 150 MeV [9]. RHIC is a flexible facility colliding a wide range of nuclei at various energies; this allows exploration of the phase diagram of QCD matter to experimentally identify the conditions for the phase transition into QGP. There are four experiments at RHIC: two larger, PHENIX (electrons, muons, hadrons and photons) [36] and STAR (hadron production over a large solid angle) [37], and two smaller, BRAHMS (particles identification over a broad range of rapidity) [38] and PHOBOS (total charged particle multiplicity and particle correlations) [39]. Each experiment was optimized for a different set of experimental observables, but common capabilities allow crucial cross checks.

In 2010 the heavy ion experiments at LHC started with a centre of mass energy of 2.76 TeV per colliding nucleon pair and in 2015 began to perform nucleus-nucleus ($A-A$) collisions with 5.5 ATeV, that is the highest energy accessible at LHC.

First results from Pb+Pb collisions at nearly 14 times higher energy at the LHC confirm the physics picture derived from RHIC data. The initial temperature at LHC is about 30% higher than at RHIC, which translate into an energy density $\epsilon_{LHC} \sim (1.3)^4 \epsilon_{RHIC}$ and a lifetime of the quark-gluon plasma about a factor of 2 larger.

Among the seven detectors constructed at the LHC, ALICE have been designed to the study of QGP. The other experiments are ATLAS (signs of new physics, including the origins of mass and extra dimensions), CMS (same purpose as ATLAS), LHCb (antimatter), TOTEM (total cross section, elastic scattering and diffraction dissociation), MoEDAL (monopole and exotic particle) and LHCf (measurement of neutral π^0 meson production in order to understand ultra high energy cosmic rays).

RHIC and LHC are therefore the two main colliders devoted to the study of the QGP at high temperature. To this goal, in these facilities two nuclei are accelerated close to the speed of light (nearly 99.995%c)

and are thus Lorentz contracted. When they collide with each other the nuclei slow down through multiple inelastic nucleon-nucleon scatterings, depositing energy into the collision zone. If the energy density reaches the critical value ($0.5 - 1\,\mathrm{GeV/fm^3}$) predicted from QCD for the phase transition, the QGP is produced between the two receding nuclei, which end up far away from the collision zone because high energy nucleons still have a big amount of momentum in forward/backward direction. Therefore, the net baryon number in the collision zone is small, while the temperature is extremely high.

The QGP created cools rapidly, expanding and emitting various types of radiation, and transforms into a hadron gas through the phase transition of QCD, after which the produced particles cease to interact with each other and move freely to the detector. Any observable measured to probe the partonic phase is therefore mixed with signals from the later hadronic phase; this is the main reason of the difficulty of extracting unambiguous signals for the QGP. It is therefore mandatory to understand the dynamics of such a collision and the evolution of the resulting fireball in order to extract any information about the early phases and the QGP. We go back to the initial formation and evolution of the QGP from the observational data with a procedure analogous to that used to study the early Universe measuring its "remnants", such as the cosmic microwave background, the abundance of atomic elements, etc. Actually, investigating formation and evolution of the QGP is a complicated task, since there are theoretical indications that it is not a simple gas of free quarks and gluons, it is rather a strongly interacting system. Indeed, the value of the viscosity over entropy density ratio is very low, $\eta/s \sim 0.1$, really close to the minimum limit conjectured for systems with coupling constant $g \to \infty$.

2.2 Collision geometry and dynamics

As the energies of the incoming nuclei in a heavy-ion collision are typically much larger than their rest masses, all velocities in the center-of-mass (CM) frame are close to c, the speed of light. Then the two nuclei are strongly Lorentz contracted along the beam direction, which is called the longitudinal direction and will be indicated in this thesis as the z-direction of the coordinate system. Thus in the CM frame the incoming nuclei appear as two tiny disk of thickness $2R/\gamma_{CM}$, where R is the nuclear radius and the amount of contraction γ_{CM} is given by

$$\gamma_{CM} = (1-\beta^2)^{-\frac{1}{2}} = (1-\frac{p_z^2}{E_{CM}^2})^{-\frac{1}{2}}, \tag{2.1}$$

where E_{CM} is the energy of one nucleus in the CM frame. However, due to the uncertainty principle, the longitudinal size of nuclei cannot be smaller than a value Δz which depends on the energy of the collision: if this is about 200 GeV then Δz is almost 1 fm. This implies a geometrical delocalization of the nucleons inside the nuclei that consequently pass each other and leave the region of the collision.

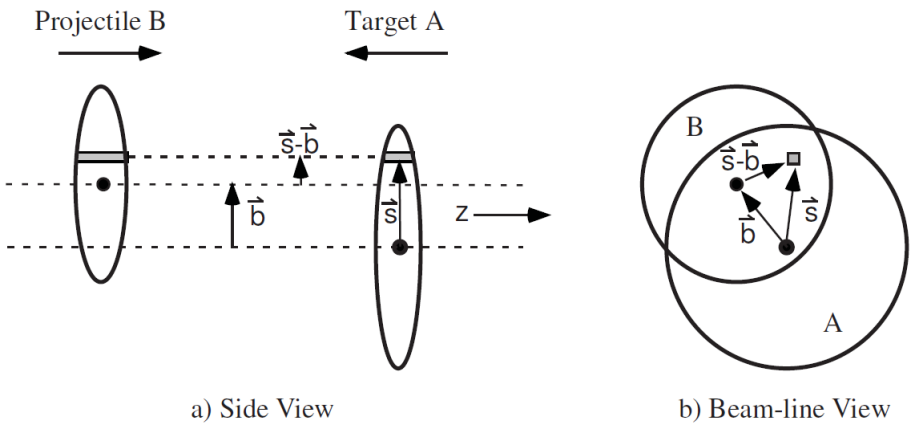

Figure 2.1: Schematic representation of the collision between the nuclei A and B at a given impact parameter b in transverse view (left) and in longitudinal view (right). Figure taken from [41].

In Fig. 2.1 a schematic representation of the collision between the nuclei A and B is depicted. Assuming that all nucleons of each incoming nucleus propagate along straight line, nucleons in the overlapped region are called *participants* whereas nucleons which do not meet any other nucleon are called *spectators*. This geometrical treatment of high energy nucleus-nucleus collisions is known as the participant-spectator model. The size of participant and spectator regions is determined by the impact parameter b, which is the distance between the centres of the two colliding nuclei and varies from one event to the other. A central collision with $b \simeq 0$ has a full overlap area and have about the maximum energy density. A peripheral collision of two nuclei with large impact parameter has a small overlap zone and tends to be similar to a $p - p$ (proton-proton) collision. The systems produced from the various initial geometries are thus different. Since the spectators keep its longitudinal velocity and emerge at nearly zero degrees in the collision, it is relatively simple to experimentally distinguish the spectators from the participants.

Experimentally, the collision geometry cannot be controlled. Nevertheless, in order to compare physical quantities in $A - A$ collisions to those in $p - p$ collisions, one needs to know how many binary nucleon-nucleon collisions N_{coll} there are in an $A - A$ collision. Moreover, we are interested to know whether an observable is related to N_{coll} or to the number of participating nucleons N_{part}. Collisions with different geometries correspond to different N_{coll} and N_{part}.

The *Glauber model* has been used to describe the collision geometry, estimating the initial spatial distribution of nucleons in the transverse plane, and to link experimental observables with a theoretical b, N_{coll} and N_{part} [41].

The use of such a geometrical model is justified by the fact that at high energies the De Broglie wavelengths of the nucleons are smaller than their transverse size, hence the total cross section of the nuclei is approximately

the sum of the individual nucleon-nucleon collision cross sections. Further assumptions are that the nucleons travel in straight lines and are not deflected after the collision. Thus, in multiple interactions each nucleon-nucleon collision can be considered as independent according to *eikonal approximation*.

The inputs for the Glauber model are the Wood-Saxon nuclear matter density and the inelastic nucleon-nucleon cross section. Monte Carlo simulations of the Glauber model are often carried out. Nucleons of incident and target nuclei are distributed randomly according to a nuclear density profile. At a given impact parameter $\mathbf{b}$ the impact parameter $\mathbf{s}$ of all the pairs of incident and target nucleons is determined in order to check whether they interact: a collision occurs when the nucleon-nucleon distance is within the range of the nucleon-nucleon inelastic cross section, i.e. $b < \sqrt{\sigma_{inel}^{NN}/\pi}$. The values of N_{coll} and N_{part} are the output of the Glauber model for a given b.

In order to obtain the expressions for the number of collisions and participants in the Glauber model, we introduce the *nuclear overlap function* $T_{AB}(b)$

$$\hat{T}_{AB} = \int \hat{T}_A(\mathbf{s})\hat{T}_B(\mathbf{s}-\mathbf{b})d^2s, \tag{2.2}$$

where s is the transverse coordinate; $\hat{T}_A$ and $\hat{T}_B$ are the *nuclear thickness functions* which give the probability to find a nucleon per unit of transverse area and are defined as

$$\hat{T}_A(\mathbf{s}) = \int \hat{\rho}_A(\mathbf{s}, z_A)dz_A, \tag{2.3}$$

being $\hat{\rho}_A$ the nuclear mass number density normalized to mass number A, which in a realistic situation for a heavy nucleus such as lead or gold is usually parametrized as a Wood Saxon distribution:

$$\rho_A(r) = \frac{\rho_{nm}}{1+\exp((r-R_A)/a)}, \tag{2.4}$$

where R_A is the nucleus radius and a is a length representing the surface thickness of the nucleus.

Through the nuclear thickness function and the nuclear overlap function it is possible to evaluate N_{coll} and N_{part} which are both strongly related to the impact parameter b:

$$N_{coll}(b) = A\,B\,\hat{T}_{AB}(b)\,\sigma_{inel}^{NN}, \tag{2.5}$$

$$N_{part}(b) = A \int \hat{T}_A(\mathbf{s}) \left\{ 1 - \left[1 - \hat{T}_B(\mathbf{s}-\mathbf{b})\sigma_{inel}^{NN} \right]^B \right\} d^2s \tag{2.6}$$

$$+ B \int \hat{T}_B(\mathbf{s}-\mathbf{b}) \{ 1 - \left[1 - \hat{T}_A(\mathbf{s})\sigma_{inel}^{NN} \right]^A \} d^2s. \tag{2.7}$$

The inelastic nucleon-nucleon cross section σ_{inel}^{NN} at RHIC ($\sqrt{s_{NN}} = 200\,\text{GeV}$) is equal to 40 mb while at LHC ($\sqrt{s_{NN}} = 5.5\,\text{TeV}$) is equal to 70 mb.

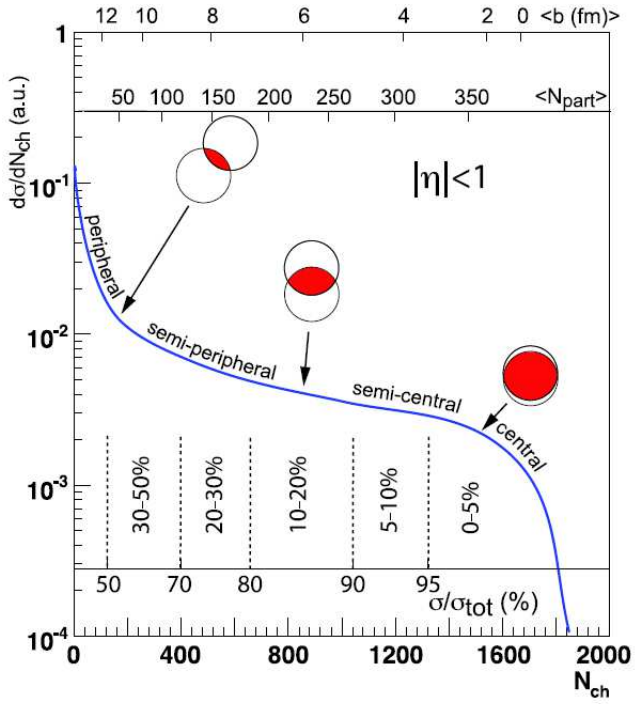

Figure 2.2: Qualitative behaviour of the correlation of the experimental observable quantity N_{ch} with Glauber calculated quantities b and $Npart$. Figure adapted from [41].

The number of binary collisions and the number of participants cannot be directly measured in experiments, therefore an observable needs

to be chosen to map the Glauber model simulation to experimental data for the centrality definition. A basic assumption is that the observable should be a monotonic function of the impact parameter. The inclusive charged particle multiplicity N_{ch}, which is a measurable quantity, can be used as a centrality definition observable: the larger the multiplicity the smaller the b. Exploiting the relation between b, N_{part} and N_{ch} it is possible to trace back to the impact parameter of the collision performing a subdivision of N_{ch} in terms of centrality class. The relation between N_{ch}, N_{part} and b is shown in Fig. 2.2. The dashed lines individuate typical centrality bins. The illustrations of various collision geometries in the beam-line view are also depicted for different centrality classes.

2.3 Space-time history of ultra-relativistic heavy ion collisions

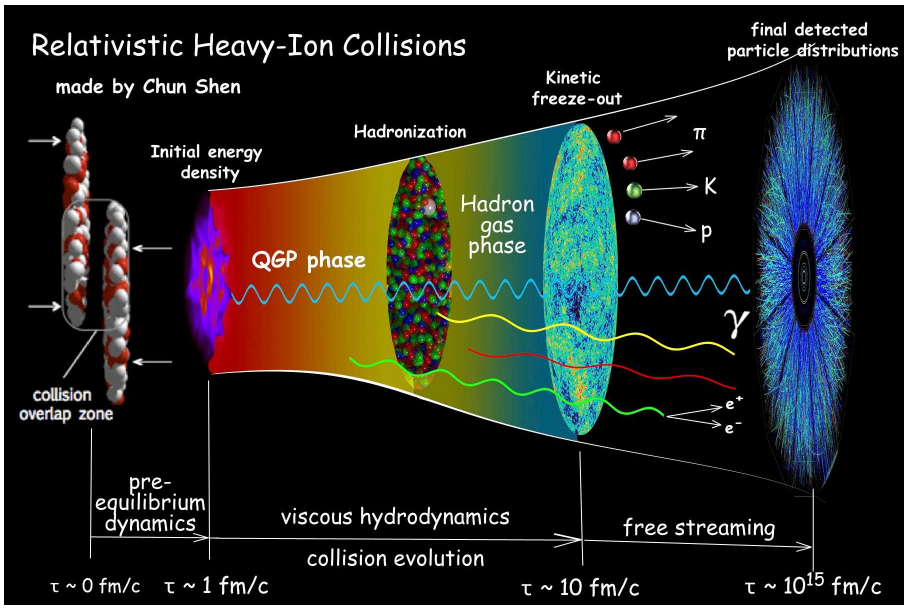

Figure 2.3: Evolution of a relativistic heavy ion collision through its many dynamical stages. Picture credit: Chun Shen (McGill University, Montreal QC, Canada).

A relativistic heavy ion collision evolves through many different stages, in which the dynamics is governed by different set of effective degrees of freedom. It is a very complicated task to follow the whole evolution of the fireball within an unified approach, due to the large range of densities and temperature explored during the collision evolution. Nevertheless transport kinetic models, which will be treated in the next chapter, allow to describe nearly the entire dynamical evolution of the system produced in relativistic heavy ion collisions by means of one single theoretical approach. Fig. 2.3 shows the different phases of a ultra-relativistic heavy ion collision (uRHIC) which are explained in the following.

Pre-equilibrium stage and thermalization

As already explained, the two incoming nuclei, in a relativistic classical picture, are Lorentz-contracted as pancakes and are approximately transparent, thus passing one through each other. In the region of the collision strong color-electric and color-magnetic fields are generated, causing an excitation of the vacuum and producing a dense matter consisting of gluons and quarks, which is highly out of equilibrium. This system according to current studies can thermalize in less than 1 fm/c, forming an equilibrated quark gluon plasma. In this very early collision stage, the primary collisions between fast partons inside the colliding nuclei generate hard particles with either a large mass or a large transverse momentum $p_T \gg 1\,\mathrm{GeV} \gg T$. Their creation involves large momentum transfer, therefore their production can be calculated in perturbative QCD. Hydrodynamic models cannot be used to describe the pre-equilibrium phase because this involves out of equilibrium processes. Hence to describe the successive stages of evolution using hydrodynamics it is necessary to know the initial condition for energy density and spatial density and estimate the time τ_0 at which the system reaches equilibrium. On the other hand, transport models can be used to describe both pre-equilibrium and

equilibrium stages if the kinetic evolution is coupled to a mechanism of particle production. In this thesis we follow this way, as we will explain in the following chapters.

Among the various models of particle production, the Glasma approach with Color Glass Condensate (CGC) initial condition gives the most efficient description of the very early stage of uRHICs [42–47]. High energy nucleus-nucleus collisions can be viewed as collisions of sheets of colored glass condensate whose degrees of freedom are those of high energy density gluonic fields.

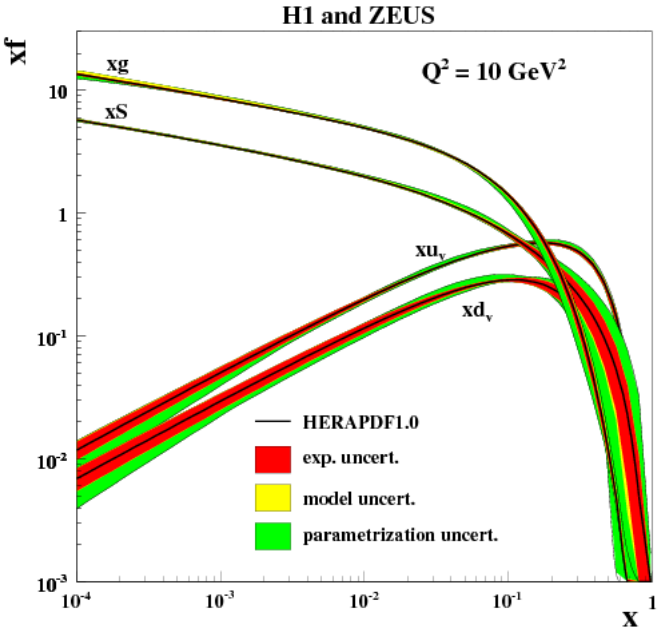

Figure 2.4: The parton distribution functions from HERA, $xu_v, xd_v, xS = 2x(\bar{U} + \bar{D}), xg$, at $Q^2 = 10\,\mathrm{GeV}^2$. Figure adapted from [48].

The idea of color-glass condensate was motivated by the rapid rising of the gluon density as a function of decreasing x, the Bjorken variable, for large momentum transfer Q^2, as shown in Fig. 2.4 [48]. As a consequence the transverse density of gluons also increases but eventually gluons overlap each other and saturate, because they must fit inside

the size of the hadron. In other words, a hadron may be viewed as a tightly packed system of gluons. In the momentum space there is a critical momentum Q_s which distinguishes between gluons tightly packed, those with $p < Q_s$, and free gluons, those with $p > Q_s$. Thus the gluon filling of the hadron is characterized by this saturation scale Q_s, which increases with both increasing energy and size of the nucleus; hence the total number of gluons may grow without limit.

Since the physical density of low-x gluons becomes large, the typical separation between gluons is small and their interaction strength becomes weak, that is $\alpha_s \ll 1$; the highly coherent gluons fill the phase space up to the maximal occupation number $\sim 1/\alpha_s$ and can thus be thought of as condensed. Because of their high speed and Lorentz time dilation, the partons of a nucleus do not evolve during the short duration of a collision; systems whose evolution happens over long time scales compared to natural ones are glasses. Hence the name Color Glass Condensate.

An infinitesimal time after the collision of the two sheets of CGC, a configuration of strong longitudinal color-electric and color-magnetic fields is produced; this form of matter is named *glasma*[1]. There are no transverse fields, except on the sheets of charge which are the sources for the glasma field. The space-time evolution of the glasma is given by the classical field equation of motion of $SU(3)$ Yang-Mills theory. In Fig. 2.5 the CGC before the collision and the formation of glasma after the collision is depicted.

The glasma fields decay in gluon pairs and in quark-antiquark giving rise to the quark-gluon plasma. Pair creation from decaying color flux tubes is due to the Schwinger mechanism, which will be explained in the fifth chapter.

Once produced, the partons in the plasma begins to collide reach-

[1]The word 'glasma' is a contraction of glass (from colored glass condensate) and plasma (from quark-gluon plasma).

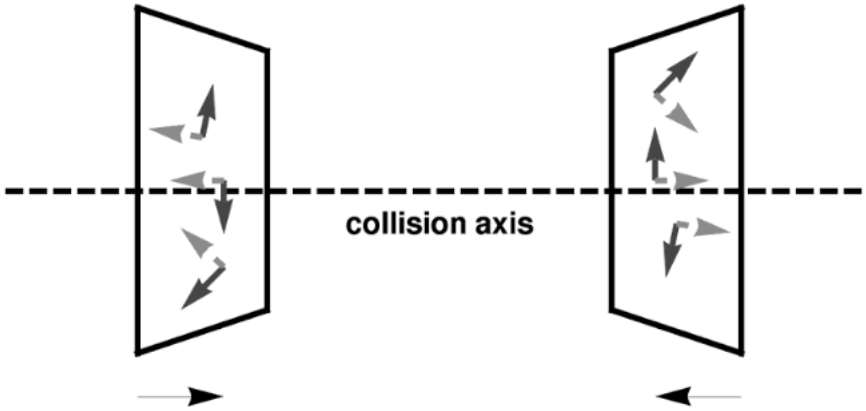

(a) Color glass condensate before collision

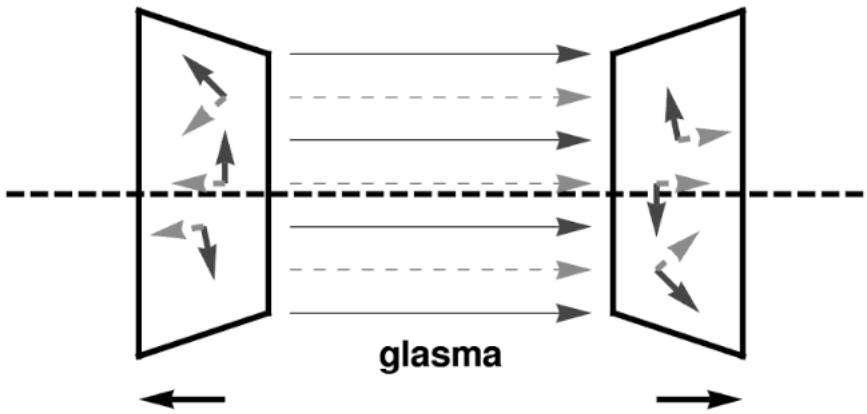

(b) Glasma fields after collision

Figure 2.5: (a) Before the collision, the two incoming nuclei can be viewed as thin sheets of color glass condensate, i.e. low-x gluons are described by a configuration of classical coherent and mutually orthogonal color electric and magnetic fields. (b) After the collision, in addition to the transverse CGC fields on the sheets there are longitudinal color electric and magnetic fields forming glasma. Figures adapted from [49].

ing a local thermal equilibrium. Experimental data suggest a very short thermalization time $\tau_{therm} < 1$ fm/c, which denotes the moment when local thermal equilibrium is achieved. This idea is supported by hydrodynamical simulations with an early starting time and is justified also by our studies based on kinetic transport theory. In fact we will dis-

cuss in the following chapters the dynamics of a parton plasma produced by color-electric flux tubes decaying through the Schwinger mechanism equilibrates within some fractions of fm/c.

Thermalization and isotropization of the system is mainly an effect of parton rescattering, but an interesting phenomenon that could speed-up equilibration is that of plasma instabilities: inhomogeneities in the glasma fields are amplified by plasma instabilities, which eventually lead to loss of coherence of the color fields and to a locally isotropized particle plasma [50–56]. Recently, the early isotropization problem has been studied also by means of anti–de Sitter/conformal field theory (AdS/CFT) methods [57, 58].

Hydrodynamical expansion

Once the system has reached thermal equilibrium it is characterized by an energy density well above the critical energy density of the QCD phase transition; thus the system is expected to be in the quark gluon plasma phase. Driven by thermal pressure gradients the QGP expands and cools down very quickly and the partons inside the bulk rescatter elastically and inelastically. The elastic collision lead the system towards kinetic equilibrium while inelastic collision cause a change in the relative abundances of the different flavours of partons until the system reaches chemical equilibrium.

This stage of the evolution of QGP is very well described by relativistic hydrodynamics or within a transport kinetic model. The latter will be used in this work and widely described in the next chapter.

In the hydrodynamical approach, the evolution equations of the system are obtained from the local conservations laws for energy-momentum and baryon number

$$\partial_\mu T^{\mu\nu}(x) = 0, \qquad \partial_\mu j^\mu_B(x) = 0. \tag{2.8}$$

$T^{\mu\nu}$ is the energy-momentum tensor that for a perfect fluid can be written

as

$$T^{\mu\nu}(x) = [\epsilon(x) + P(x)]\, u^{\mu}(x) u^{\nu}(x) - P(x) g^{\mu\nu}, \tag{2.9}$$

where $u^{\mu}(x)$ is the flow four-velocity and $g^{\mu\nu}$ is the metric tensor. $j^{\mu}_{B}(x)$ is the baryon number current given by

$$j^{\mu}(x) = n_B(x) u^{\mu}, \tag{2.10}$$

where n_B is the baryon number density defined in the local rest frame of the fluid.

In order to solve the five equations (2.8) an additional equation of the form $P = P(\epsilon, \rho)$, called the equation of state (EOS), is necessary. Indeed, the equations (2.8) together with the EOS form a closed system, which can be solved once the initial condition, i.e. energy density $\epsilon(x)$ and velocity profile $u^{\mu}(x)$, have been specified.

The ideal hydrodynamics described above is valid for a fluid in which dissipative effects are neglected. Nevertheless, the latter ones can be taken into account adding to the expression of the energy momentum tensor terms that consider a finite viscosity of the fluid. This turns out to be a non trivial extension because relativistically one has to go to second order gradient expansion. The last involves additional parameters and a self-consistent full derivation and implementation is still subject of studies. In fact it seems that the quark gluon plasma has a low but non zero shear viscosity η. More precisely, as already said, the value of the viscosity over entropy density ratio is really close to the minimum limit conjectured for systems with coupling constant $g \to \infty$, that is $\eta/s \sim 0.1$.

Hadronic phase and freeze-outs

When the energy density drops below a pseudo-critical value $\epsilon_c = 1\,\mathrm{GeV/fm^3}$ the phase transition from the parton plasma to a hadron gas take place. There are at least two different class of microscopic mechanisms of *hadronization*: fragmentation and coalescence. In the first

one each parton fragment into a jet of hadrons that carry a fraction of the momenta of the initial parton. This is the predominant way to hadronize in $p-p$ collisions for partons with transverse momentum greater than 2 GeV. In $A-A$ collision another mechanism of hadronization is likely to be dominant in producing hadrons up to $p_T \sim 5-6$ GeV: it consists in the recombination of two or three quarks that form respectively mesons or baryons [59, 60].

In the hadronic phase the hadrons rescatter one to each other until the distance between them is larger than the range of strong interactions $d_R \sim 1$ fm. Then at densities $\rho < d_R^3$ all scatterings stop and the hadrons decouple and free stream towards the detector; this is called *kinetic freeze-out*. In the hydrodynamic approach the hadronization is introduced by means of the Cooper-Frye formula, which consists in a freeze-out algorithm that stops the hydrodynamic evolution and transforms the hydrodynamic outputs, such as energy density, baryon density and flow, into hadron spectra, making use of the statistical model. This procedure correctly accounts for hadronization of the bulk, i.e. for partons with $p_T \lesssim 2$ GeV. Many efforts have being done in recent years to describe both the QGP phase, the hadronization and the hadronic phase within a transport kinetic model.

The kinetic freeze-out described above take place after the *chemical freeze-out*, i.e. the moment when the inelastic collisions stop. Indeed at low colliding energies the inelastic cross sections are typically smaller than the elastic cross sections, hence during the cooling down of the hadronic system the inelastic processes cease before the elastic collisions. As a natural consequence $T_{chem} > T_{kin}$, where T_{chem} is the temperature of the chemical freeze-out inferred from the studies of the ratios of hadron multiplicities and T_{kin} is the temperature of the kinetic freeze-out inferred from the studies of the transverse-momentum spectra [49].

2.4 Physical observables of QGP

The relativistic heavy ion collisions are dynamic processes with typical length and time scales of order 10 fm and 10 fm/c respectively. In order to probe the formation and the properties of the QGP we need to observe as many as possible particles and radiations emitted during the whole space-time evolution of the collision. A selection of the main physical observables which may give signatures of QGP is resumed in this section.

Each observables is the result of the entire evolution of the fireball and is therefore affected by the different stage we have explained in the previous section. Hence it is important to identify which observable brings information on a particular phase and how it may be influenced by other stages.

2.4.1 Global observables

An important task in heavy ion experiments is to understand how the initial kinetic energy is redistributed after the collision of the two nuclei in terms of observables, such as particle production and energy per particle. A related question is that of entropy production, as the initial nuclei form a very low entropy state and the final configuration has a very large entropy.

Yields and spectra

Global observables such as the emitted particle number per unit rapidity dN/dy and the observed transverse energy per unit rapidity dE_T/dy are related to the early-time entropy density s_0 and the early-time energy density ϵ_0 at the freeze-out time τ_f in the central $A-A$ collisions [61, 62].

The rapidity distribution of particles dN/dy is related to the initial entropy density through the formula

$$s_0 = \frac{\xi}{A_T \tau_0} \frac{dN}{dy}, \tag{2.11}$$

where τ_0 is the initial time, i.e. the time when the local thermalization is reached which is less than 1 fm/c, and A_T is the transverse overlap area of the colliding nuclei (for a central collision of two identical nuclei of radius R this is simply $A_T = \pi R^2$). ξ is the proportionality constant of the relation between entropy density and number density of particles assumed for a relativistic plasma:

$$s = \xi n; \tag{2.12}$$

for an ideal gas at high temperature $\xi = 3.6$ for bosons and $\xi = 4.2$ for fermions.

The transverse energy dE_T/dy is related to the initial energy density by the formula:

$$\epsilon_0 = \frac{1}{A_T \tau_0} \frac{dE_T}{dy}\bigg|_{y=0} \left(\frac{\tau_f}{\tau_0}\right)^{\lambda}, \tag{2.13}$$

where $\lambda = c_s^2$, being $c_s^2 = dp/d\epsilon$ the sound velocity, and then depends by the equation of state $\epsilon(p)$; $(\tau_f/\tau_0)^{\lambda}$ is a measure of the energy transfer due to the work done by the pressure during the hydrodynamical expansion. Thus we need information about the freeze-out time τ_f to evaluate ϵ_0 by data on dE_T/dy.

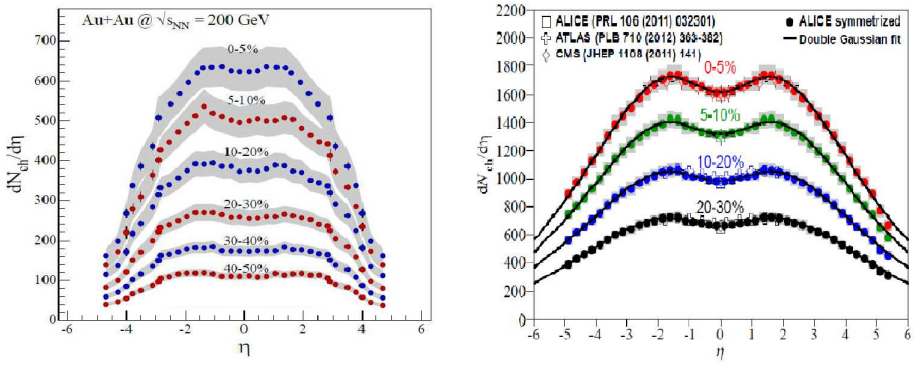

Figure 2.6: Pseudo-rapidity density of charged particles for different centrality bins at RHIC (left panel) and LHC (right panel). Figure adapted from [38] and [63] respectively.

Fig. 2.6 shows the overall multiplicity of charged particles observed in

collisions at RHIC and LHC for various collision centralities as a function of pseudo-rapidity. The figure in the left panel shows that the multiplicity in $\sqrt{s_{NN}} = 200$ GeV Au+Au collisions at RHIC is about $dN/d\eta = 625$ charged particles per unit of rapidity around $\eta = 0$ for central collisions. Integration of the charged particle pseudo-rapidity distributions corresponding to central collisions tells us that about 4600 charged particles are produced in each of the 5% most central collisions; since we only measure charged particles, and not the neutrals, we multiply this multiplicity by 3/2 to obtain the total particle multiplicity of about 7000 particles. The right panel shows that the multiplicity in $\sqrt{s_{NN}} = 2.76$ TeV Pb+Pb collisions at LHC is about $dN/d\eta = 1600$ charged particles per unit of rapidity around $\eta = 0$ for central collisions. The integral of the most central distribution $0-5\%$ corresponds to about 15000 charged particles.

2.4.2 Flow observables

One of the most important discoveries of heavy ion collisions is that the medium shows a high degree of collectivity, usually referred as flow.

As in the early stage of the collision nuclear matter is compressed, if the interactions between the constituents of the medium have large cross sections, density gradients are expected to translate into outward pressure, which causes the system to expand at relativistic speed.

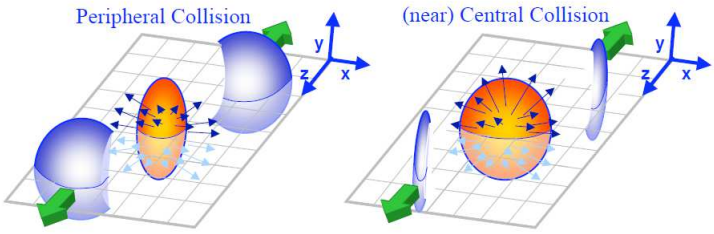

Figure 2.7: Qualitative picture of the shape of the nuclear overlap region between the two nuclei in a peripheral (left) and in a central (right) collision.

Experiments can probe this outward pressure with great precision by characterizing non central (intermediate impact parameter) nuclear collisions. In these reactions, the nuclear overlap region between the two nuclei is not circular in the transverse plane, but instead is strongly deformed, resulting elliptically shaped. The difference between the two cases is qualitatively shown in Fig. 2.7.

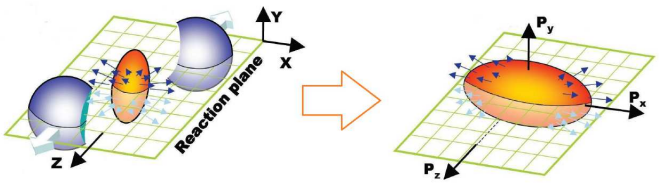

Figure 2.8: Schematic illustration of how the spatial anisotropy (almond shaped impact region in the reaction plane) after a non-central collision evolves in anisotropy in momentum space.

A measure of such deformation is given by the spatial eccentricity:

$$\epsilon(b) = \frac{\langle y^2 - x^2 \rangle}{\langle y^2 + x^2 \rangle} \tag{2.14}$$

which depends on the impact parameter b and it is initially non-zero and positive. The interactions inside the plasma transfer this spatial deformation into an anisotropy in momentum space, as depicted in Fig. 2.8. Hence the initial eccentricity influences the azimuthal momentum distribution of the emitted particles. Experimentally, the azimuthal distribution of particle emission is analysed with respect to the reaction plane in terms of a Fourier expansion of the transverse momentum spectrum as:

$$E\frac{d^3N}{d^3p}(b) = \frac{d^2N}{2\pi p_T dp_T dy}\left(1 + \sum_{n=1}^{\infty} 2v_n(p_T, b)\cos n(\phi - \Phi_R)\right) \tag{2.15}$$

where ϕ is the azimuthal angle of the particle and Φ_R is the azimuthal angle of the reaction plane in the laboratory frame. There are sophisticated experimental techniques which allow to determine the reaction plane angle in each nucleus-nucleus collision [36, 37, 39].

For a non central collision the density distribution has many non-zero Fourier coefficients, with the second coefficient by far the largest. The stronger the interactions among the particles, the greater is the translation of spatial anisotropy into momentum anisotropy of the final observed particles.

As the system expands, the spatial distribution becomes more isotropic, hence a large contribution to the flow must come from interactions in the first 4-5 fm/c after the collision [64]. This momentum anisotropy is preserved through the transition to the final observed hadron distributions.

The experiments do not directly measure pressure gradients or flow, but rather the coefficients of the ϕ angular distributions. The first two coefficients in (2.15) are the *directed flow* and the *elliptic flow*, respectively given by $v_1 = \langle \cos(\phi - \Phi_R) \rangle$ and $v_2 = \langle \cos 2(\phi - \Phi_R) \rangle$. The amplitude of elliptic flow grows with increasing impact parameter because the overlap region of the incoming nuclei becomes more asymmetric. Higher Fourier components of the angular distribution are also observed in the correlation data; these arise primarily from fluctuations in the initial positions of the nucleons within the nucleus (Fig. 2.9).

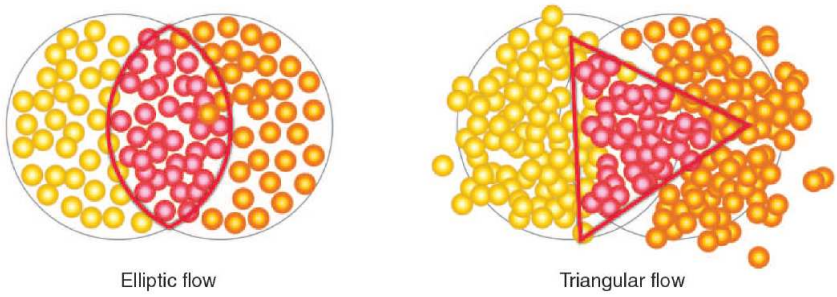

Figure 2.9: Elliptic (left) and triangular (right) flow patterns arise from the locations of individual nucleons at the instant when two nuclei interpenetrate. The nucleons of one nucleus are shown in yellow and the other in orange. Red indicates those nucleons in the overlap region, which actually collide. Figure from [65].

Elliptic flow

The elliptic flow v_2 is the largest contribution in the azimuthal asymmetry of the momentum distributions and can be determined from the following formula:

$$v_2(p_T, b) = \langle \cos 2\phi \rangle = \left\langle \frac{p_x^2 - p_y^2}{p_x^2 + p_y^2} \right\rangle, \tag{2.16}$$

which gives the exact shape of the ellipse.

Experiments have extensively measured the elliptic flow for a broad range of hadron species over a significant kinematic range [36, 37, 39]. In $p - p$ reactions a significant v_2 coefficient is observed owing to hard parton-parton scattering creating opposing jets of hadrons. In heavy ion reactions, the Fourier decomposition really measures particle emission directly correlated with the orientation of density gradients, as demonstrated by the fact that the v_2 for all charged particles at low-p_T scales linearly with the eccentricity of the nuclear overlap region.

The elliptic flow is the prominent indicator of the low viscosity and the fast thermalization of the matter created in heavy-ion collisions [66, 67]. Both hydrodynamical and parton cascade calculations have shown that the generation of the elliptic flow saturates in the first 4−5 fm/c making this observable sensitive to the QGP phase.

In Fig. 2.10 the elliptic flow coefficient v_2 for several hadron species is plotted as a function of their transverse momentum p_T, compared to calculations with hydrodynamical models. Up to $p_T \sim 1.5$ GeV, the elliptic flow $v_2(p_T)$ follows the hydrodynamical predictions for an ideal fluid, i.e. with negligible viscosity, as is expected from a medium in local thermal equilibrium with low viscosity. Provided that more then 99% of all final hadrons have $p_T < 1.5$ GeV, it is evident that a very low viscosity fluid is created in ultra-relativistic heavy ions collisions, giving the name of "almost perfect fluid" to the quark-gluon plasma. The fall of the hydrodynamic predictions for $p_T > 1.5$ GeV indicates a breakdown of

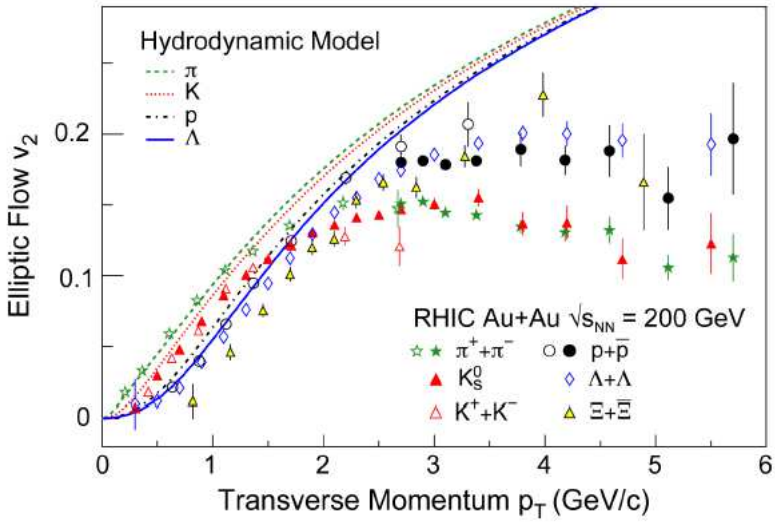

Figure 2.10: Elliptic flow as a function of transverse momentum of a variety of hadron species for gold-gold collisions at $\sqrt{s_{NN}} = 200$ GeV measured by the PHENIX [68] and STAR [69, 70] collaborations. Hydrodynamic calculations are indicated by lines. Figure from [71].

the local thermal equilibrium for particles with high momenta and, on the other hand, the necessity to include dissipative terms in hydrodynamics equations.

An important additional measurement from the PHOBOS experiment indicates that v_2 drops significantly for charged particles as one moves away from mid-rapidity [72, 73]. This observation contradicts many hydrodynamic calculations invoking the Bjorken scenario [62]. Additionally, some have interpreted this as evidence for incomplete equilibration and thus for a breakdown in the hydrodynamic assumption [74].

There is another important information from the figure: baryons have a considerable larger v_2 with respect to mesons. This difference has not found an explanation in the hydrodynamical framework but can be explained by the coalescence model for hadronization, which predicts that the v_2 of any hadronic species follows the partonic flow scaled by the number n_q of (recombined) constituent quarks in the hadron under

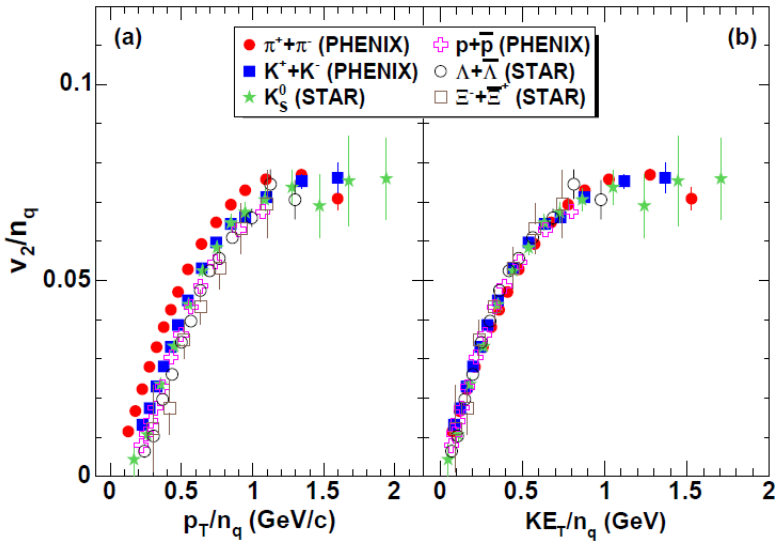

Figure 2.11: Scaling properties of azimuthal anisotropy at RHIC are evident from the behaviour of v2/nq vs pT /nq (left) and v2/nq vs KET /nq for several particle species obtained in minimum bias Au+Au collisions. Figure from [76].

consideration [59, 75]

$$v_2^{hadron} \simeq n_q v_2^{quark}(p_T/n_q), \tag{2.17}$$

with $n_q = 2$ for mesons and $n_q = 3$ for baryons. In fig 2.11 is shown the quark number scaling of the elliptic flow. Such a scaling clearly indicates that the flow is developed at the quark level, hence quarks are the true degrees of freedom of the matter created in relativistic heavy ion collisions. Actually, a 20% breaking of this scaling has been observed at LHC, but even in the coalescence model the scaling is approximated.

2.4.3 Hard observables

Jet quenching

In the first stage of a ultra-relativistic heavy ion collision particles with high transverse momentum are produced and propagate through the plasma interacting with the bulk matter and loosing energy. Such parti-

cles can be used to probe the plasma as proposed long time ago in [77–81]. The production of high p_T partons can be theoretically predicted using the perturbative QCD (pQCD) framework. The high energy partons lose energy in the plasma through elastic scattering with the components of the bulk and radiating gluons in a way similar to the bremsstrahlung photon emission in QED. The main differences between QED and QCD radiative energy loss are due to the non-Abelian nature of QCD: the emitted gluons itself carry color charges and interact with all the color charges in the medium (both quarks and gluons), whereas photons does not interact with themselves. Emitted gluons travel a random walk inside the plasma causing a non-linear dependence of the energy loss on the thickness of the medium. In the evaluation of the radiative energy loss must be also considered the Landau-Pomeranchuk-Migdal effect (LPM) that takes into account the coherence effect, due to the interaction of the hard partons with more than one scattering center. At high parton energy the radiative mechanism is the main responsible for the parton energy loss. The energy loss of high p_T partons causes an attenuation or disappearance of the hadrons jet resulting from the fragmentation of these high partons. This phenomenon of suppression is called jet quenching and is one of the most important probe of the formation of the QGP. The suppression is quantified by the nuclear modification factor R_{AA} which is given by the ratio between the spectrum of partons produced in $A-A$ collision and the one relative to $p-p$ collisions multiplied by the scaling factor N_{coll}:

$$R_{AA}(p_T) \equiv \frac{1}{N_{coll}} \frac{d^2N^{AA}/dp_T d\eta}{d^2N^{pp}/dp_T d\eta} \tag{2.18}$$

A $R_{AA} = 1$ meant that $A-A$ collision would be only a superposition of $p-p$ collisions. On the other hand a R_{AA} greater then one indicates the formation of a system different from the one created in $p-p$ collisions. One of the open challenge regarding the jet quenching is to explain the

difference in the suppression between the different hadron species. This is strongly related to the different energy loss experienced by quarks and gluons but also to the inelastic collisions which change the relative abundances of quarks and gluons.

Heavy quarks

Heavy-flavor particles (charm and bottom quarks) are particularly valuable probes for the properties of the medium produced in ultra-relativistic collisions of heavy nuclei. In the context of QGP physics they are considered heavy because their mass, m_Q, is large not only with respect to Λ_{QCD} but also to the temperature T of the plasma. This property has important implications [82, 83]. Fist of all, $m_Q \gg \Lambda_{QCD}$ allows to determine the initial heavy-quark spectra by means of pQCD and makes them a suitable probe of the out-of-equilibrium stage: the production time is much smaller than the QGP lifetime, $t_0^Q \ll t_{QGP}$, therefore heavy quarks pass through the entire evolution of the fireball; their equilibration time t_{eq}^Q is of the order of the QGP lifetime, but smaller than the light-quark one, $t_{eq}^Q \sim t_{QGP} \gg t_{eq}^q$, hence in principle they carry more information. Moreover, $m_Q \gg T$ implies that the momentum exchange by collisions (dominated by elastic processes) is $|q^2| \ll m_Q^2$, then the dynamics can be treated as a Brownian motion by means of a Fokker-Planck equation (derived from an expansion in momentum transfer of the Boltzmann equation) which constitutes a significant simplification for the study of transport properties; nevertheless, this approach is a good approximation for the b flavor, while in the case of c quarks a full Boltzmann treatment is more appropriate [84].

Gluon bremsstrahlung of heavy quarks differs from the case of massless parton considered in the previous section. Due to the large mass m_Q the radiation probability with respect to the light quark case is smaller at low p_T and the distribution of soft gluons radiated by heavy quarks is

suppressed because of the dead-cone-effect: gluon emission is restricted to angles higher then $\theta_0 = m_Q/E_Q$ with respect to the heavy quark direction [85].

The two key observables in heavy quark sector are the nuclear modification factor R_{AA} given by Eq. (2.18), which gives an estimate of the total energy loss experienced by heavy quark in the bulk medium, and the elliptic flow v_2 given by second Fourier coefficient of Eq. (2.15), which measures the azimuthal momentum anisotropy of heavy mesons. Both observables for heavy mesons and their decay products have been measured at RHIC and LHC facilities and it was surprisingly observed a low R_{AA} and a high v_2 comparable to those of light hadrons, giving raise to the so called $R_{AA} - v_2$ puzzle; the simultaneous description of these two observables and a consistent explanation of this puzzle is a challenge for all the existing models [86].

J/ψ suppression

J/ψ particles are bound states of a charm and anticharm $(c - \bar{c})$. They are produced mostly by the hard scatterings in the first stage of the collision. They are created also in $p - p$ collisions and in this case they can freely escape from the collision region. Instead, in the case of nucleus-nucleus collisions, the J/ψ are produced in the QGP phase and feel the screening effects of the medium. In fact, although the J/ψ meson is a tightly bound particle, in a quark-gluon plasma environment the charm-anticharm potential is screened, in a way similar to the analogous phenomenon called Debye screening in QED. As a consequence, the interaction between the $\bar{c}$ and c quarks is strongly weakened when $r_{c\bar{c}} > \lambda_D$, with λ_D the Debye screening length. For sufficiently high density λ_D is so small that the J/ψ dissociates leading to a suppression of the observed yield compared to $p - p$ or proton-nucleus collisions [87].

2.4.4 Electromagnetic probes

During the evolution of a nuclear collision photons and dileptons are created and may be used as signatures of the QGP. Such probes are very much important because, interacting only electromagnetically, they do not suffer further scatterings after their emission. Therefore photons and dileptons provide information related to the phase of the fireball evolution in which they originate. Unfortunately there are so many sources which can produce photons or dileptons that the analysis of such kind of observables is quite difficult.

For the purposes of this thesis photon observables of the quark gluon plasma deserve a more detailed analysis and therefore they will extensively treated in next chapters.

CHAPTER 3

BOLTZMANN TRANSPORT THEORY

Relativistic quantum transport theory plays an important role in the space-time description of matter under extreme conditions of high energy density and it is the most efficient approach to describe out-of-equilibrium situations.

Transport kinetic approaches aim to describe highly dynamical systems where the time dependence of the phenomena to be studied cannot be neglected.

Transport theory is one of the pillars on which this thesis is based and thus we dedicate this chapter to present its main features, from the classical relativistic formulation and its relation to relativistic hydrodynamics to the applications in quantum field theory. Finally, we explain how it can be numerically implemented in a box.

3.1 Classical relativistic transport theory

Considering a classical relativistic many-particle system, the probability to find a particle in the 8-dimensional phase space volume element $d^4x\, d^4p$ at the position x with momentum p is

$$dP(x,p) \equiv f(x,p) d^4x d^4p, \tag{3.1}$$

where $f(x,p)$ denotes the corresponding phase space density. $f(x,p)$ is a Lorentz scalar, while $x^\mu = (t, \boldsymbol{x})$ and $p^\mu = (p^0, \boldsymbol{p})$ are four-vectors. In a classical system the four-momentum is usually on-shell, such that not all components of p are independent but are related by the condition $p^0 = \sqrt{\mathbf{p}^2 + m^2}$ which express the energy in terms of the three-momentum and particle mass; we assume that this constraint is incorporated in the phase space density:

$$f(x,p)|_{p^0=\epsilon(\mathbf{p})} \equiv f(\mathbf{x}, \mathbf{p}, t).$$

In kinetic theory all macroscopic quantities are defined through the distribution function. If one is interested to the collective behaviour of the system or the behaviour of a typical particle, the knowledge of the one-body density $f(x,p)$ is equivalent to the full solution. Instead, in order to study the correlations among particles one should consider also two-body distributions $f(x_1, x_2, p_1, p_2)$ or even higher order many-body distributions. In general, this is quite complicated and not necessary, as physical quantities experimentally accessible, such as spectra, are expressed in terms of one-body distribution density, on which we restrict our attention.

For a system composed by N relativistic particles the phase space density can be written as

$$f(x,p) = \sum_{i=1}^{N} \delta^4 \left[x_i(\tau) - x\right] \delta^4 \left[p_i(\tau) - p\right],$$

where τ is the relativistic proper time.

The evolution of the one-body density $f(x,p)$ from one time-like hypersurface to another follows from the Liouville's theorem [88], which states: iff there are only conservative forces then the phase space density is a constant of motion.

From this theorem we derive the evolution equation for f in terms of

proper time τ as follows:

$$\begin{aligned} 0 &= \frac{d}{d\tau} f(x,y) \equiv \frac{d}{d\tau} \sum_i \delta^4 \left[x_i(\tau) - x\right] \delta^4 \left[p_i(\tau) - p\right] \\ &= \sum_i \left\{ \frac{dx_i^\mu}{d\tau} \frac{\partial}{\partial x^\mu} + \frac{dp_i^\mu}{d\tau} \frac{\partial}{\partial p^\mu} \right\} \delta^4 \left[x_i(\tau) - x\right] \delta^4 \left[p_i(\tau) - p\right] \\ &= \left\{ \frac{1}{m} p^\mu \frac{\partial}{\partial x^\mu} + \mathcal{F}^\mu(x) \frac{\partial}{\partial p^\mu} \right\} f(x,p), \end{aligned} \tag{3.2}$$

where we used the constancy of the density that is represented in terms of the particle trajectories $\{x_i(\tau), p_i(\tau)\}$ in the first line, carried out the differentiation in the second and employed definition of the four-velocity and equation of motion in the last; $\mathcal{F}^\mu(x)$ denotes external or self-consistent internal four-forces. This is the *relativistic Vlasov equation*.

The Vlasov equation (3.2) is appropriate for a system in which there are only conservative forces, because it does not take into account dissipative effects that arise from incorporating two-body correlations in the one-body treatment. More generally, allowing for scattering of particles into and out of phase space volume elements, the distribution function is no more a constant of motion, i.e. $(d/d\tau) f(x,p) \neq 0$, but changes as a consequence of collisions. Then the Vlasov equation is replaced by the Boltzmann equation:

$$\left\{ \frac{1}{m} p \cdot \partial_x + \mathcal{F}(x) \cdot \partial_p \right\} f(x,p) = \mathcal{C}[f](x,p), \tag{3.3}$$

where $\mathcal{C}[f]$ denotes the collision term.

In general, the exact equations are the coupled integro-differential equations for the many-particle distribution function:

$$f^{[j]}(\boldsymbol{x}_1, \boldsymbol{x}_2, ..., \boldsymbol{x}_j, \boldsymbol{p}_1, \boldsymbol{p}_2, ..., \boldsymbol{p}_j, t),$$

where j runs from 1 to the total number of particles N. The coupled equations have a hierarchical structure in which $f^{[j]}$ is related to $f^{[j+1]}$; this is the BBGKY (Bogoliubov-Born-Green-Kirkwood-Yvon) hierarchy.

The Boltzmann equation can be derived from this set of equations with the following assumptions.

- Only binary collisions contribute.
- The correlation between the two particles before the collision is neglected and the number of binary collisions is supposed to be proportional to the product of the distribution functions of the colliding particles and to a transition rate, which is a measure of the probability of the scattering process. As a consequence, the two-particle distribution reduces to a product of the one-particle distributions: $f(x_1, x_2, p_1, p_2) = f(x_1, p_1)f(x_2, p_2)$. This is known as Boltzmann's "Stosszahlansatz" (collision number hypothesis) or molecular chaos assumption.
- The distribution function varies slowly in space-time, i.e. the changes over a characteristic interaction length and during a characteristic interaction time are negligibly small.

In this way the collision term turns out to be a non-linear functional of the one-body densities.

In the non relativistic limit the Boltzmann-Vlasov equation Eq. (3.3) reduces to:

$$\left\{ \frac{\partial}{\partial_t} + \boldsymbol{v} \cdot \nabla_x + \boldsymbol{F} \cdot \nabla_p \right\} f(\boldsymbol{x}, \boldsymbol{p}, t) = \mathcal{C}[f](\boldsymbol{x}, \boldsymbol{p}, t). \tag{3.4}$$

We have seen that the Vlasov equation (3.2) is appropriate for systems with only conservative forces and thus describes non-dissipative phenomena, whereas the Boltzmann equation incorporates dissipative scattering processes which lead to entropy production.

If the system is close to local equilibrium or when the mean free path, i.e. the average distance traversed by a particle between two successive collisions, is very small, one may linearize the right-hand side of the

transport equation in $\delta f = f - f_0 \ll f$ obtaining the so called Relaxation Time Approximation (RTA), in which the collision term assumes the simple form:

$$\mathcal{C}[f] \simeq -\frac{1}{\tau_r}(f - f_0), \tag{3.5}$$

where τ_r denotes the relaxation time parameter, which characterizes the typical time scale for the system to relax towards the local one-body equilibrium distribution f_0. The relaxation time collision term could be derived rigorously as an approximation of a two-body scattering term but can also be seen as a phenomenological ansatz taking the dissipation into account. The relaxation time may be estimated by the mean free time between the collisions,

$$\tau = \frac{\lambda_{mfp}}{v} = \frac{1}{n\sigma_{tot}v},$$

where σ_{tot} is an averaged total cross-section of the binary collision, v is the averaged relative velocity of particles and n is the averaged particle density of the system.

The distribution function evolving through the Boltzmann equation (3.3) tends to a definite limit as time evolves and the state of the system turn into an equilibrium state. In this stable state the entropy of the system reaches its maximum value. Then the vanishing of entropy production in the whole space-time is a necessary condition for equilibrium. This requirement along with the fact that the equilibrium distribution function is a solution of the transport equation uniquely determines its form.

The equilibrium distribution function is expressed in terms of the density, the temperature and the global four-velocity of the system. All other thermodynamic variables may be evaluated explicitly as functions of these parameters, giving a exhaustive macroscopic description of a relativistic system in equilibrium.

A particular equilibrium solution of the Boltzmann equation (3.3) is the

Jüttner distribution,

$$f_J(x,p) \equiv \frac{1}{(2\pi)^3} \mathrm{e}^{-\beta(U\cdot p+\mu)},$$

where the local parameters $\{\beta \equiv 1/T, U^\mu, \mu\}(x)$ denote inverse temperature, flow four-velocity and chemical potential respectively.

In the non relativistic case this equilibrium function reduces to the Maxwell-Boltzmann distribution,

$$f_{MB}(x,p) \equiv \frac{1}{(2\pi T)^{3/2}} \mathrm{e}^{-\beta(\boldsymbol{p}-\boldsymbol{p}_0)^2/2m},$$

which is solution of the classical Boltzmann equation (3.4).

3.2 Relation to relativistic hydrodynamics

As we said in the previous section, in kinetic theory all the macroscopic observables are described by the phase space density $f(x,p)$ introduced in Eq. (3.1). The particle number four-current and the energy-momentum tensor are defined respectively:

$$j^\mu(x) \equiv \int \mathrm{d}^4p\, p^\mu f(x,y),$$
$$T^{\mu\nu}(x) \equiv \int d^4p\, p^\mu p^\nu f(x,y).$$

These are the main quantities of interest in the hydrodynamic description of matter, where one integrates out the momentum space information contained in the distribution function [89].

In ideal hydrodynamics the motion of the fluid, which characterize the evolution of the system, is given by the laws of conservation of energy-momentum and baryon number Eq. (2.8), where $T^{\mu\nu}$ and j^μ are determined through macroscopic quantities by Eq. (2.9) and (2.10) respectively.

It is straightforward to show that j^μ and $T^{\mu\nu}$, as defined in transport theory, satisfy the appropriate continuity equations related to mass (or

charge) and four-momentum conservation [90]. Using the Boltzmann equation (3.3) together with Eq. (3.5) we obtain:

$$\begin{aligned}\partial_\mu j^\mu &= \int d^4p p \cdot \partial_x f = -m \int d^4p \left(\mathcal{F} \cdot \partial_p f + \frac{f - f_0}{\tau_r} \right) \\ &= -\frac{m}{\tau_r} \int d^4p (f - f_0) \equiv -\partial_\mu \delta j^\mu,\end{aligned}$$

where we find a dissipative contribution δj^μ on the right-hand side, which vanishes only if the ordinary density equals the equilibrium density determined by f_0. This condition for ideal hydrodynamics has the underlying hypothesis that the mean free path is so small that the $f(x,p)$ is always at equilibrium during the evolution.

Similarly, one obtains:

$$\begin{aligned}\partial_\mu T^{\mu\nu} &= -m \int d^4p p^\nu \left(\mathcal{F} \cdot \partial_p f + \frac{f - f_0}{\tau_r} \right) \\ &= m\mathcal{F}^\nu \left(\int d^4p f \right) - \frac{m}{\tau_r}(j^\nu - j_0^\nu),\end{aligned}$$

where the second term on the right-hand side is related to a dissipative contribution $-\partial_\mu \delta T^{\mu\nu}$ to the energy-momentum tensor, while the first term presents the external or self-consistent force density acting on the system; j_0^μ is defined like j^μ with f replaced by f_0.

We have already said that a distribution function $f \neq f_{eq}$ is associated also to entropy production. Entropy may be useful even to delineate the bulk properties of matter produced in relativistic collisions; indeed, as we have seen in Section 4.2.1, it can be related to the observed particle multiplicities [62, 89].

The entropy four-current is defined as

$$S^\mu(x) \equiv \int d^4p \, p^\mu f(x,y)[1 - \log \frac{f(x,y)}{f_0(x,y)}];$$

proceeding similarly to what we have done for j^μ and $T^{\mu\nu}$ we obtain the

entropy production formula:

$$\partial_x \cdot S = \int d^4p\, p \cdot \partial_x [f(1 - \log \frac{f}{f_0})] = -\int d^4p\, (p \cdot \partial_x f) \log \frac{f}{f_0}$$
$$= m \int d^4p \left(\mathcal{F} \cdot \partial_p f + \frac{f - f_0}{\tau_r} \right) \log \frac{f}{f_0} = \frac{m}{\tau_r} \int d^4p\, (f - f_0) \log \frac{f}{f_0}.$$

Since $(\log x)(x-1) \geq 0$ for all $x \geq 0$ we recover Boltzmann's "H-theorem":

$$\partial_x \cdot S \geq 0,$$

expressing a positive entropy production which vanishes only in equilibrium, when $f = f_0$.

3.3 Collision integral

We have seen that the Vlasov equation (3.2) does not take into account collisions among particles. In order to consider those dissipative effects we need to add a collision term $C[f](x,p)$ on the right-hand side of the Vlasov equation, obtaining the Boltzmann equation (3.3).

Usually the collision term includes two-body collision process C_{22} and for high densities or in case of radiative processes $2 \to 3$ process C_{23}. In our model we consider only binary collisions. Assuming that there are no particle correlations before each collision (molecular chaos hypothesis), the C_{22} term is related to the product of the phase space densities of the colliding particles and is given by

$$\begin{aligned} C_{22} =& \frac{1}{2E_1} \int \frac{d^3p_2}{(2\pi)^3 2E_2} \frac{1}{\nu} \int \frac{d^3p_1'}{(2\pi)^3 2E_1'} \frac{d^3p_2'}{(2\pi)^3 2E_2'} (f_1' f_2' - f_1 f_2) \\ & \times |\mathcal{M}_{12 \to 1'2'}|\, (2\pi)^4 \delta^{(4)}(p_1' + p_2' - p_1 - p_2), \end{aligned} \tag{3.6}$$

where $\nu = 2$ if one considers identical particles in order to avoid double counting, otherwise $\nu = 1$. $\mathcal{M}_{i \to f}$ is the *invariant matrix element*, i.e. the transition amplitude for the scattering process. Along with the molecular chaos hypothesis it is also assumed that collisions are local: the difference

in space-time coordinates of the particles before and after the collision can be neglected. On the other hand, after a scattering the momenta of colliding particles are changed statistically according to the differential cross section.

If we have to deal with particles following the Fermi-Dirac statistics, we can account for the quantum effect of Pauli-blocking with the following substitution in the collision term:

$$f_1' f_2' - f_1 f_2 \longrightarrow f_1' f_2' (1 - f_1)(1 - f_2) - f_1 f_2 (1 - f_1')(1 - f_2'),$$

which does not allow scattering if the final momenta have occupation number equal to one. This is called the Boltzmann-Nordheim collision integral.

On the other hand, the Bose-Einstein statistics is included in the collision integral by substituting:

$$f_1' f_2' - f_1 f_2 \longrightarrow f_1' f_2' (1 + f_1)(1 + f_2) - f_1 f_2 (1 + f_1')(1 + f_2'),$$

which favours scattering if the final momenta have non-zero occupation number.

In this cases the solution of the local equilibrium condition $C[f] = 0$ is given by the Fermi-Dirac and Bose-Einstein distribution respectively:

$$f_{FD/BE}(x, p) = \frac{1}{(2\pi)^3} \frac{1}{\mathrm{e}^{(p \cdot u(x) - \mu(x))/T(x)} \pm 1}.$$

3.4 Quantum transport theory

In the previous section we have discussed how we get the correct quantum equilibrium distribution for a fermionic or bosonic many-particle system as fixed point of the relativistic transport equation.

Then we may ask whether there exists a quantum mechanical density function which yields the expectation value of operators in the form of

phase space integrals. One possible answer is provided by the Wigner function.

In quantum theory the evolution of a system may be described in terms of the density matrix operator:

$$\hat{\rho} = \sum_i w_i |\Psi_i\rangle\langle\Psi_i|,$$

and the expectation value of any observables can be computed as

$$\langle \hat{O}(t) \rangle = \mathrm{Tr}[\hat{\rho}(t)\hat{O}]. \tag{3.7}$$

For any operator one can define its Weyl transform:

$$\tilde{A}(x,p) = \int \frac{dy}{2\pi\hbar} \mathrm{e}^{ipy/\hbar} \langle x_+ | \hat{A} | x_- \rangle,$$

where $x_\pm = x \pm y/2$ and which satisfy the following property:

$$\mathrm{Tr}[\hat{A}\hat{B}] = \int \tilde{A}(x,p)\tilde{B}(x,p)dxdp. \tag{3.8}$$

The Weyl transform of the density operator is called *Wigner function*:

$$W(x,p) = \int \frac{dy}{2\pi\hbar} \mathrm{e}^{ipy/\hbar} \langle x_+ | \hat{\rho} | x_- \rangle = \int \frac{dy}{2\pi} \mathrm{e}^{ipy} \Psi^*(x_+)\Psi(x_-).$$

From Eq. (3.7) and the property (3.8) follows:

$$\langle O(t) \rangle = \int W(x,p)\tilde{O}(x,p)dxdp,$$

which shows that the Wigner function in quantum theory plays in many aspects the same role of the distribution function in statistical mechanics.

We can obtain the quantum version of the Vlasov equation for the evolution of the Wigner function simply performing a Wigner transformation of the Schroedinger equation or, equivalently, of the Heisenberg equation. Starting from this latter equation of motion for the density operator,

$$\frac{\partial \hat{\rho}}{\partial t} = [\hat{\rho}, \hat{H}],$$

with $\hat{H} = \hat{p}^2/2m + \hat{U}$, and applying the Wigner transform,

$$\int \frac{dy}{2\pi\hbar} e^{ipy/\hbar} \langle x_+| \left(\frac{\partial \hat{\rho}}{\partial t} - [\hat{\rho}, \frac{\hat{p}^2}{2m} + \hat{U}] \right) |x_-\rangle = 0,$$

after some calculations we get the equation of motion for the Wigner function:

$$\frac{\partial W}{\partial t} + \frac{p}{m}\frac{\partial W}{\partial x} + \sum_{k=0} \frac{1}{(2k+1)!} \left(\frac{\hbar}{2}\right)^{2k} U(x) (\overleftarrow{\nabla}_x \cdot \overrightarrow{\nabla}_p)^{2k+1} W(x,p) = 0. \tag{3.9}$$

No approximation has been made so far, hence this equation is exactly equivalent to the Heisenberg equation or to the Schroedinger equation.

If the gradient of the potential is not too strong, the summation over k index can be truncated at the first term, in which $\hbar$ does not appear explicitly, still accounting for quantum evolution; then the previous equation can be written as

$$\frac{\partial W}{\partial t} + \frac{p}{m}\frac{\partial W}{\partial x} + \nabla_x U \cdot \nabla_p W(x,p) = 0,$$

which has the same form of the classical transport equation. Since Eq. (3.9) contains only odd derivative of the potential, the previous equation remains exact for linear or quadratic potentials (for example an harmonic oscillator potential).

3.5 Transport equation in Quantum Field Theory

In quantum-relativistic field theory, in order to obtain a function analogous to the classical distribution function we start defining the Wigner operator:

$$\begin{aligned} \hat{W}_{\alpha\beta} &\equiv \int \frac{d^4y}{(2\pi\hbar)^4} e^{-ip\cdot y/\hbar} \bar{\psi}_\beta(x) e^{\frac{1}{2}y\cdot\partial^\dagger} e^{-\frac{1}{2}y\cdot\partial} \psi_\alpha(x) \\ &= \int \frac{d^4y}{(2\pi\hbar)^4} e^{-ip\cdot y/\hbar} \bar{\psi}_\beta(x_+) \psi_\alpha(x_-), \end{aligned}$$

where $\partial^\dagger$ and ∂ play the role of translation generator acting to the left and right respectively, the spinors are Heisenberg operators, $\hat{W}_{\alpha\beta}$ is a 4×4 matrix and the spinor indices α and β run from 1 to 4. The Wigner function is the ensemble average of the previous Wigner operator:

$$W(x,p) \equiv \langle : \hat{W}(x,p) : \rangle.$$

The brackets indicate ensemble averaging and the colons normal ordering with respect to the vacuum state. The physical interpretation of the Wigner function become clear if we note that in terms of the four momentum operator $\hat{p}_\mu = \frac{1}{2} i(\partial_\mu - \partial_\mu^\dagger)$ the integration over y gives formally

$$W_{\alpha\beta}(x,p) = \langle : \bar{\psi}_\beta(x)\delta^4(p-\hat{p})\psi_\alpha(x) : \rangle.$$

In this way $\mathrm{Tr}\, W(x,p)$ measures the scalar density at space-time point x_μ with momentum p_μ.

The Wigner function matrix can always be decomposed in terms of the 16 independent generators of the Clifford algebra. We choose the conventional basis $\Gamma_i = 1$, $i\gamma^5 = -\gamma^0\gamma^1\gamma^2\gamma^3$, γ^μ, $\gamma^\mu\gamma^5$, $\sigma^{\mu\nu}$, which under hermitian conjugation transforms in the following way:

$$\Gamma_i^\dagger = \gamma^0 \Gamma_i \gamma^0. \tag{3.10}$$

The expansion on this basis of the Wigner function reads:

$$\begin{aligned} W(x,p) = W_S(x,p) + i\gamma_5 W_P(x,p) + \gamma_\mu W_V^\mu(x,p) \\ + \gamma_\mu\gamma_5 W_A^\mu(x,p) + \frac{1}{2}\sigma_{\mu\nu} W_T^{\mu\nu}(x,p). \end{aligned}$$

The functions $W_S \equiv \frac{1}{4}\mathrm{Tr}W$, $W_P \equiv -\frac{1}{4} i \mathrm{Tr}[\gamma^5 W]$, $W_V^\mu \equiv \frac{1}{4}\mathrm{Tr}[\gamma^\mu W]$, $W_A^\mu \equiv \frac{1}{4}\mathrm{Tr}[\gamma^5\gamma^\mu W]$ and $W_T^{\mu\nu} \equiv \frac{1}{4}\mathrm{Tr}[\sigma^{\mu\nu} W]$ are all real due to property (3.10) and behave under Lorentz transformation like a scalar, a pseudo-scalar, a vector, an axial-vector and an antisymmetric tensor respectively. They represent physical current densities; for example the vector current is given by

$$j^\mu(x) = \langle \bar{\psi}\gamma^\mu\psi \rangle = \int d^4p\, \mathrm{Tr}[\gamma^\mu W(x,p)] = 4\int d^4p\, W_V^\mu(x,p),$$

where the trace is over spinor indices.

The pseudo-scalar W_P and axial-vector W_A parts vanish in the case of locally spin-saturated system [91] and the tensor part can be neglected in the classical limit [92], so that the Wigner function in this case can be written as

$$W(x,p) = W_S(x,p) + \gamma_\mu W_V^\mu(x,p). \tag{3.11}$$

The procedure to derive the quantum-relativistic transport equation for the Wigner function is similar to that used in the previous section, making the Wigner transformation of the field equation of motion. We consider a system described by a fermionic field which interacts through a scalar field and derive the transport equation in this simplified case.

From the Lagrangian of such a system,

$$\mathcal{L} = \bar{\psi}(x)(i\gamma_\mu\partial^\mu - g_s\sigma)\psi(x) - \frac{1}{2}m_s^2\sigma^2,$$

we obtain the following equation of motion for the fermionic field:

$$[i\gamma_\mu\partial^\mu - (m - g_s\sigma)]\psi(x) = 0. \tag{3.12}$$

The Wigner transformation of the previous equation is given by:

$$\int \frac{d^4y}{(2\pi\hbar)^4} \mathrm{e}^{-ip\cdot y/\hbar}\bar{\psi}_\beta(x_+)[i\gamma_\mu\partial^\mu - (m - g_s\sigma)]\bar{\psi}_\alpha(x_-) = 0;$$

after some calculations we get

$$\begin{aligned}&\left(\gamma\cdot p + \frac{i}{2}\gamma\cdot\partial - m\right)_{\beta\delta} W_{\delta\alpha}(x,p) \\ &+ \int \frac{d^4y}{(2\pi\hbar)^4}\mathrm{e}^{-ip\cdot y/\hbar}\langle :\bar{\psi}_\beta(x_+)\bar{\psi}_\alpha(x_-)\sigma(x_-): \rangle = 0.\end{aligned} \tag{3.13}$$

The previous equation is exactly equivalent to the Dirac equation (3.12), since no approximation has been made to obtain it. However to derive the usual expression of the quantum relativistic transport equation one makes two approximations.

- The evaluation of the integrals in Eq. (3.13) is considerably simplified if we use the Mean Field Approximation (MFA) in which the quantum fluctuations are neglected, treating the scalar field as a classical function and thus keeping it out from the expectation value.

- Using the so called semiclassical approximation the field can be expanded in a Taylor series at the spacetime point x and, if its gradient is not too strong, it is reasonable to truncate the expansion at the first order.

With the previous simplification the scalar field is given by

$$\sigma(x_-) \simeq \sigma(x) - \frac{y^\mu}{2}\partial^x_\mu \sigma(x); \tag{3.14}$$

substituting it in Eq. (3.13) we get:

$$\left(\gamma \cdot p + \frac{i}{2}\gamma \cdot \partial - m^*(x) - \frac{i}{2}\partial^x_\mu \sigma(x)\partial^\mu_p\right) W(x,p) = 0,$$

where $m^*(x) = m - \sigma(x)$ is the effective mass.

Including higher order derivatives in (3.14) we would get an expansion in terms of higher order derivatives of the field and of the Wigner function.

The previous equation can be decomposed in two equations, one for the imaginary part and the other for the real part. For the latter we have:

$$\left(\gamma \cdot p - m^*(x)\right) W(x,p) = 0,$$

whereas for the imaginary part we get:

$$\left(\gamma \cdot \partial - \partial^x_\mu m^*(x)\partial^\mu_p\right) W(x,p) = 0.$$

The real part contains the mass-shell condition; indeed, multiplying the left-hand side for $(\gamma \cdot p + m^*(x))$ and taking the trace over the Dirac indices we obtain

$$\left(p^2 - m^{*2}\right) W(x,p) = 0;$$

including more terms in the gradient expansion (3.14) would have brought terms breaking the mass-shell constraint.

Making use of the decomposition of $W(x,p)$ into scalar and vector components as shown in Eq. (3.11), writing all in terms of the scalar part $W_S(x,p)$ and using the relation between the latter and the one-body phase space distribution $f(x,p) = W_S(x,p)/m^*(x)$ we get:

$$\left(p\cdot\partial + m^*(x)\partial_\mu m^*(x)\partial_p^\mu\right) f(x,p) = 0. \tag{3.15}$$

This is the Vlasov equation which describes the evolution of the phase space density $f(x,p)$ for fermions interacting through a scalar field σ. The quantum effects are encoded in the fields, while the evolution of $f(x,p)$ appears as the classical one.

Dissipative effects arising from collisions are taken into account adding the collision integral $C[f]$ on the right-hand side of Eq. (3.15) and thus finding the quantum-relativistic Boltzmann transport equation for the system under consideration:

$$\left(p\cdot\partial + m^*(x)\partial_\mu m^*(x)\partial_p^\mu\right) f(x,p) = C[f](x,p). \tag{3.16}$$

The above equation describes the motion of particles considering both collisions, i.e. short range interactions, and mean field, i.e. long range effects. Therefore, a Boltzmann-like kinetic transport equation can be derived under pertinent approximation, as discussed above, also in the relativistic quantum field theory.

3.6 Numerical implementation of transport equation

In order to numerically implement the Boltzmann equation we divide the space into a three-dimensional lattice and we use the standard *test particle method* to sample the distribution function $f(x,p)$; the collision

integral $C[f]$ is solved by means of a *stochastic algorithm*.
Both techniques will be explained in this section.

3.6.1 Test particle method

The test particle method was introduced by Wong [93] and is used in almost all transport calculations [94–98]. In this method the phase space distribution function is sampled by means of a large number of so called test particles. Usually the test particles are chosen point-like both in coordinate and momentum space, hence the phase space distribution can be written as a sum of δ functions:

$$f(\boldsymbol{r},\boldsymbol{p},t) = \omega \sum_{i=1}^{N_{test}} \delta^{(3)}(\boldsymbol{r}-\boldsymbol{r}_i(t))\delta^{(3)}(\boldsymbol{p}-\boldsymbol{p}_i(t)),$$

where $\boldsymbol{r}_i(t)$ and $\boldsymbol{p}_i(t)$ indicate respectively the position and the momentum of the i-th test particle, N_{test} is the total number of test particles and ω is a renormalization factor, such that the integral over coordinates and momenta of the phase space distribution is equal to the total number of real particles $N_{particles}$:

$$\int d^3r \int \frac{d^3p}{(2\pi)^3} f(\boldsymbol{r},\boldsymbol{p},t) = \frac{\omega}{(2\pi)^3} N_{test} = N_{particles};$$

hence $(2\pi)^3/\omega$ is equal to the number of test particles per unit real particle. With the introduction of test particles the solution of the transport equation reduces to solve the classical equation of motion for the test particles. Indeed, it can be shown by means of the Liouville theorem that the phase space distribution given as a collection of point-like test particles is a solution of the Boltzmann equation (3.16) if positions and momenta of the test particles satisfy the relativistic Hamilton equations:

$$\dot{\boldsymbol{r}}_i = \frac{\boldsymbol{p}_i}{E_i}, \qquad \dot{\boldsymbol{r}}_i = -\nabla_r E_i + coll,$$

where the term *coll* contains the effect of the collision integral. The previous equation of motion are numerically implemented in the following

way:

$$\boldsymbol{r}_i(t+\Delta t) = \boldsymbol{r}_i(t-\Delta t) - 2\Delta t \frac{\boldsymbol{p}_i(t)}{E_i(t)}$$
$$\boldsymbol{p}_i(t+\Delta t) = \boldsymbol{p}_i(t-\Delta t) - 2\Delta t \nabla_r E_i + coll,$$

where the index i refers to the i-th test particle and Δt is the mesh time.

3.6.2 Stochastic method

The numerical implementation of the collision integral is based on the stochastic method introduced by Xu and Greiner in a parton cascade [99]. In this algorithm a probability P_{22} is associated to a collision between two particles; whether the collision happen or not is sampled stochastically: it will occur only if a number randomly extracted between 0 and 1 is lower than P_{22}. The probability P_{22} may be derived directly from the collision term (3.6) of the Boltzmann-Vlasov equation (3.16). Indeed, the collision probability per unit volume $\Delta^3 x$ and unit time Δt can be defined as the ratio between the number of collisions occurring in such unit box $\Delta^3 x$ during the time interval Δt and the total number of pairs present in the unit box:

$$P_{22} = \frac{\Delta N_{coll}^{2\to 2}}{\Delta N_1 \Delta N_2}. \tag{3.17}$$

The number of binary collision $\Delta N_{coll}^{2\to 2}$ can be derived directly from the collision term of the Boltzmann equation [99–102]: assuming two particles in a spatial volume element $\Delta^3 x$ with momenta in the range $(\mathbf{p}_1, \mathbf{p}_1 + \Delta^3 p_1)$ and $(\mathbf{p}_2, \mathbf{p}_2 + \Delta^3 p_2)$, the collision rate per unit phase space for such particle pair derived from Eq. (3.6) is given by

$$\frac{\Delta N_{coll}^{2\to 2}}{\Delta t \frac{1}{(2\pi)^3} \Delta^3 x \Delta^3 p_1} = \frac{1}{2E_1} \frac{\Delta^3 p_2}{(2\pi)^3 2E_2} f_1 f_2 \frac{1}{\nu} \int \frac{d^3 p_1'}{(2\pi)^3 2E_1'} \frac{d^3 p_2'}{(2\pi)^3 2E_2'} \left|\mathcal{M}_{12\to 1'2'}\right| (2\pi)^4 \delta^{(4)}(p_1 + p_2 - p_1' - p_2').$$

Employing the definition of cross section for particles with mass m_i,

$$\sigma_{22} = \frac{1}{4F} \frac{1}{\nu} \int \frac{d^3 p_1'}{(2\pi)^3 2E_1'} \frac{d^3 p_2'}{(2\pi)^3 2E_2'} \left|\mathcal{M}_{12\to 1'2'}\right| (2\pi)^4 \delta^{(4)}(p_1 + p_2 - p_1' - p_2'),$$

where $F = \sqrt{(p_1 \cdot p_2)^2 - m_1 m_2}$ is called invariant flux, $\Delta N_{coll}^{2\to 2}$ can be written in a more compact way:

$$\Delta N_{coll}^{2\to 2} = \frac{1}{(2\pi)^3} f_1 \Delta^3 p_1 \frac{1}{(2\pi)^3} f_2 \Delta^3 p_2 \Delta^3 x \Delta t \sigma_{22} \frac{F}{E_1 E_2}. \tag{3.18}$$

The total number of pair present in a unit box is given by

$$\Delta N_1 \Delta N_2 = \frac{1}{(2\pi)^3} f_1 \Delta^3 x \Delta^3 p_1 \frac{1}{(2\pi)^3} f_2 \Delta^3 x \Delta^3 p_2. \tag{3.19}$$

The relative velocity between the two particles can be computed from the invariant flux F:

$$v_{rel} = \frac{F}{E_1 E_2} = \frac{\sqrt{[s - (m_1 + m_2)^2][s - (m_1 - m_2)^2]}}{2E_1 E_2},$$

where $s = (p_1 + p_2)^2$ is the Mandelstam variable. Inserting Eq. (3.18) and Eq. (3.19) in (3.17) and employing the definition of σ_{22} and v_{rel}, the collision probability can be expressed as

$$P_{22} = v_{rel} \sigma_{22} \frac{\Delta t}{\Delta^3 x}.$$

If the test particle method is employed, P_{22} has to be divided by N_{test} in order to scale the cross section $\sigma \to \sigma / N_{test}$ and get the correct collision probability .

In [99] it is shown that the numerical solution obtained with the stochastic method converges to the exact solution of the Boltzmann equation in the limit $\Delta t \to 0$, $\Delta^3 x \to 0$. Hence we divide the space into sufficiently small spatial cells and we use sufficiently short temporal steps in such a way that the typical scales of spatial and temporal inhomogeneities of the particle densities are larger than $\Delta^3 x$ and Δt respectively; therefore the configuration of particles can be considered locally homogeneous both in space and time, a necessary condition to get stable results from this numerical algorithm. A particle may collide only with another particle in the same cell and the collision probability has to be calculated for each pair inside the cell and compared with a random number. This procedure is replicated for all cells in spatial lattice and for all time steps.

Strictly speaking, such collisions have not to be considered as real collisions but as a manner to map the evolution of the phase space induced by the matrix element $\mathcal{M}_{i\to f}$: this is the stochastic sampling.

3.6.3 Trasport theroy at fixed viscosity

Usually inputs of a transport approach are cross sections of a given set of microscopic processes, but in our approach we start from a fixed value of the viscosity over entropy density ratio η/s and compute cross sections according to the Chapman-Enskog (CE) equation [103], simulating a fluid with the desired shear viscosity [97, 103–107]. In this way we make a more direct link between transport theory, based on a description in terms of parton distribution functions, and hydrodynamical formulations, in which the dynamics is governed by macroscopic quantities. In the Chapman-Enskog approach η/s is related to the temperature T, the total cross section σ_{tot} and the density ρ [103]; therefore, we fix the shear viscosity and compute cell by cell the correspondent cross section by means of the relation

$$\sigma_{tot} = \frac{1}{5}\frac{T}{\rho\, g(a)}\frac{1}{\eta/s}, \tag{3.20}$$

which is valid for a generic differential cross section

$$\frac{d\sigma}{dt} \sim \frac{\alpha_s^2}{(t-m_D^2)^2}$$

as proved in Ref. [103]. In the above equation $a = m_D/2T$, with m_D the screening mass regulating the angular dependence of the cross section, while the function $g(a)$ reads

$$g(a) = \frac{1}{50}\int dy\, y^6 \left[\left(y^2+\frac{1}{3}\right) K_3(2y) - y\, K_2(2y)\right] h\left(\frac{a^2}{y^2}\right),$$

where K_n are the Bessel functions and the function h relates the transport cross section to the total one:

$$\sigma_{tr}(s) = \sigma_{tot}\, h(m_D^2/s),$$

being $h(\zeta) = 4\zeta(1+\zeta)[(2\zeta+1)\log(1+1/\zeta) - 2]$. The $g(a)$ is the proper function accounting for the correct relaxation time $\tau_\eta^{-1} = g(a)\,\sigma_{tot}\,\rho$ associated to the shear viscosity transport coefficient. For isotropic cross section, i.e. $m_D \to \infty$, the function $g(a)$ is equal to $2/3$ and Eq. (3.20) reduces to the relaxation time approximation with $\tau_\eta^{-1} = \tau_{tr}^{-1} = \sigma_{tr}\,\rho$, while for finite values of m_D, corresponding to anisotropic scatterings, $g(a) < 2/3$.

In the regime where viscous hydrodynamics applies the specific microscopic details of the cross section are irrelevant, hence our approach is an effective way to simulate a fluid at a given η/s by means of transport theory [107], with the advantage to start from the one-body distribution function instead of the energy-momentum tensor.

CHAPTER 4

MODELLING THE PRE-EQUILIBRIUM STAGE OF RELATIVISTIC HEAVY ION COLLISIONS

The understanding of early stage dynamics and of thermalization mechanisms that lead to the formation of the quark-gluon plasma is one of the most interesting and challenging open issue of ultrarelativistic heavy ion collisions. In Chapter 2 we have seen that in the standard initial scenario of such nuclear collisions, immediately after the two nuclei had passed one through each other a peculiar configuration of strong longitudinal color-electric and color-magnetic coherent fields named *glasma* is produced [42–47]; as the system expands quantum fluctuations cause the decay of the glasma to a parton liquid which thermalizes in $\tau_{eq} \lesssim 1\,\mathrm{fm}/c$, a scenario in agreement both with hydrodynamic models [67] and calculations based on transport theory [99, 107]. Quantum fluctuations in the glasma fields are amplified by plasma instabilities, particularly the Weibel instability, which eventually lead to loss of coherence of the color fields and to a locally isotropized and thermalized particle plasma [53, 54, 56, 108–112].

Among the other approaches, models based on the AdS/CFT correspondence [57, 58, 113–115], in which thermalization appears as the

formation of a black hole horizon in the dual theory, have been developed recently in order to study the early equilibration problem.
Besides plasma instabilities, a possible mechanism causing initial field decay and quark-gluon plasma production is the Schwinger effect. It was first introduced in 1936 by Heisenberg and Euler [116] and formalized in the context of quantum electrodynamics by Schwinger more than sixty years ago [117]. The Schwinger mechanism consists of a vacuum instability towards the creation of particle pairs by a strong electric field, and it is related to the existence of an imaginary part in the quantum effective action of an electric field; see Ref. [118] for a review.

In this chapter we present our model of early times dynamics of the system produced in relativistic heavy ion collisions by an initial color-electric field which then decays to a plasma by the Schwinger effect. One of the main novelties of our study consists in the coupling of field evolution to plasma dynamics by solving consistently the classical field equations and the relativistic Boltzmann equations; the self-consistent solution of the problem allows, among other things, to take into account the backreaction of the color currents on the classical field, which has been often neglected in previous studies. Moreover, since we solve the full kinetic equation without resorting to relaxation time approximation, we can explore the early time dynamics in a more suitable way than how has been done in [119]. Even more, we do not rely on linear response theory to relate the color currents to the electric field, thus going beyond what has been done previously in [120].

In this Chapter, we focus on a single flux tube of a given transverse area and with a longitudinal chromoelectric field that we assume homogeneous in the transverse plane. Although this geometry is a strong simplification of the realistic initial conditions relevant for heavy ion collision experiments, this implementation allows to better understand the physics which underlies the formation of the quark-gluon plasma and

to compute quantities which serve as indicators of thermalization and isotropization of the system and of timescales of such processes.

In the next chapter we will describe a more realistic initial condition, developed in order to simulate RHIC and LHC collisions and to investigate the effect of the pre-equilibrium dynamics on photon emission.

4.1 From chromoelectric flux tubes to the quark-gluon plasma

In order to describe the initial stage of relativistic heavy ion collisions we simulate the formation of a quark-gluon plasma resulting from the decay of color flux tubes created just after the collision of the two incoming nuclei. The production of the parton plasma is due to the Schwinger effect, whereas the dynamical evolution of the system particles+field is obtained coupling in a self-consistent way relativistic kinetic equations to field equations.

Due to the complexity of the physical problem, we do not insist on implementing the most realistic geometrical and dynamical conditions relevant for heavy ion collision experiments, in which one should take into account several flux tubes in the transverse plane more similar to the glasma configuration and express the color field evolution by means of Yang-Mills equations; rather we consider a simpler situation implementing an Abelian Flux Tube (AFT) model [42–44] with the following main ingredients:

- the initial condition consists of a longitudinal color-electric field which is produced by color charges in the colliding nuclei, hence neglecting initial color-magnetic fields and ignoring initial transverse fields originated from quantum fluctuations;
- the color-electric field decays into particle pairs by the Schwinger mechanism;

- the particles propagate in the medium colliding and interacting with the background color field;
- particle creation as well as particle currents affect in a self-consistent way the color-electric field;
- we neglect the non-Abelian term in the evolution equation of the electric field (see the next section for more details).

The last assumption allows the easiest implementation of the coupling of classical field equations to relativistic kinetic theory in the presence of the Schwinger mechanism. Nevertheless, even though the model is called Abelian, such nomenclature simply refers to the fact that in the evolution equation for the classical field self-interaction terms coming from non-vanishing structure constants of the color gauge group are neglected [49]. Gauge self-interactions are still present in this simulations, thanks both to the Schwinger effect which produces charged gluons from the classical field and to displacement currents which affect the evolution of the field.

Coupling field equations to kinetic equations for the many particle system produced through the Schwinger mechanism, we can follow the entire dynamical evolution of the system produced in relativistic heavy ion collisions, from the very early beginning to final stages, within one single theoretical approach.

4.1.1 Schwinger mechanism

The problem of pair formation in strong electric fields has been investigated recently by means of real-time lattice simulations [121, 122]; moreover non-Abelian generalizations of the Schwinger probability have been discussed in the case of both static and time-dependent fields [123–126]. In the last forty years, Schwinger particle production has been considered as a mechanism for the color field decay in the framework of quark-gluon plasma physics [49, 119, 120, 127–142].

In this subsection we describe our implementation of Schwinger particle production, assuming that the initial longitudial color field is polarized along the third direction of adjoint color space, meaning that only one particular color charge is present in the two colliding nuclei [119].
In the case of a static box, the decay probability of a color-electric field E in massless particles by means of the Schwinger effect is given by

$$\frac{dN_{jc}}{d\Gamma} \equiv p_0 \frac{dN_{jc}}{d^4x d^2p_T dp_z} = \mathcal{R}_{jc}(p_T)\,\delta(p_z)\,p_0 \tag{4.1}$$

with

$$\mathcal{R}_{jc}(p_T) = \frac{\mathcal{E}_{jc}}{4\pi^3}\left|\ln\left(1 \pm e^{-\pi p_T^2/\mathcal{E}_{jc}}\right)\right|, \tag{4.2}$$

where j and c are respectively flavor and color indices: $j = 0$ stands for gluons, while $j = 1, N_f$ labels quarks and the corresponding negative values of j labels antiquarks; the plus (minus) sign corresponds to the creation of a boson (fermion-antifermion) pair. The momentum component p_T and p_z refer to each of the two particles created from the vacuum; $\mathcal{E}$ is the effective force which acts on the tunnelling pair, depends on color and flavor and is given by

$$\mathcal{E}_{jc} = (g|Q_{jc}E| - \sigma_j)\,\theta\,(g|Q_{jc}E| - \sigma_j)\,,$$

where σ_j corresponds to the string tension depending on the flavor considered and $p_0 = \sqrt{p_T^2 + p_z^2}$ is the single particle kinetic energy. The Q_{jc} are color-flavor charges [49] which for quarks are

$$Q_{j1} = 1/2, \quad Q_{j2} = -1/2, \quad Q_{j3} = 0, \qquad j = 1, N_f;$$

for antiquarks the color-flavor charges are just minus the corresponding charges for quarks; finally for gluons the charges are

$$\begin{aligned} &Q_{01} = 1, && Q_{02} = 1/2, && Q_{03} = -1/2, \\ &Q_{04} = -Q_{01}, && Q_{05} = -Q_{02}, && Q_{06} = -Q_{03}. \end{aligned}$$

We have only six gluons, corresponding to the non-diagonal color generators, as we assume that the initial color field is polarized along the third direction of adjoint color space, therefore it cannot produce gluons with the same color; the two gluon fields corresponding to the diagonal color generators have vanishing coupling with the background field, hence they cannot be produced by the Schwinger mechanism.
Eq. (4.1) is then easily generalized to the case of an expanding box, as we will see in the next section.

4.1.2 Relativistic kinetic equations

In order to study the evolution of the system self-consistently we couple the dynamical evolution of the color field to the dynamics of the many-particle system produced by the decay. The latter is described by the relativistic Boltzmann transport equation which, in presence of a gauge field $F^{\mu\nu}$, is given by

$$\left(p^\mu \partial_\mu + g Q_{jc} F^{\mu\nu} p_\nu \partial_\mu^p\right) f_{jc}(x,p) = \frac{dN_{jc}}{d\Gamma} + C_{jc}\left[f\right], \tag{4.3}$$

where $f_{jc}(x,p)$ is the distribution function for flavor j and color c and $F^{\mu\nu}$ is the color-electromagnetic tensor. On the right hand side $dN/d\Gamma$ is the invariant source term, which describes the creation of quarks, antiquarks and gluons due to the decay of the color-electric field and is given by Eq. (4.1), and $C\left[f\right]$ represents the collision integral described in Section 3.3, which accounts for change of f due to collision processes and is responsible for a non-zero viscosity ($\eta/s \neq 0$). Considering only $2 \to 2$ body elastic scatterings, the collision integral ig given by

$$\begin{aligned} C_{22} = \int \frac{d^3p_2}{(2\pi)^3 2E_2} \frac{d^3p_1'}{(2\pi)^3 2E_1'} \frac{d^3p_2'}{(2\pi)^3 2E_2'} (f_1' f_2' - f_1 f_2) \\ \times \left|\mathcal{M}\right|^2 (2\pi)^4 \delta^{(4)}(p_1' + p_2' - p_1 - p_2), \end{aligned}$$

where we omit flavor and color indices for simplicity; $\mathcal{M}$ is the transition amplitude for the elastic process and is related to the differential cross

section through the formula

$$|\mathcal{M}|^2 = 16\pi\, s^2\, \frac{d\sigma}{dt},$$

being s the Mandelstam variable.

In our simulations Eq. (4.3) is numerically solved as explained in Section 3.6, using the test particles method to sample the distribution function and computing the collision integral by means of Monte Carlo methods based on the stochastic interpretation of the transition amplitude [97, 103–107, 143–145]. Moreover we use the approach at fixed η/s described in same section, choosing the shear viscosity over entropy density ratio of the fluid and computing cross sections by means of the Chapman-Enskog (CE) equation (3.20) [97, 103–107].

4.1.3 Maxwell equations

We couple relativistic kinetic theory to evolution equations of the electric field; assuming an abelian dynamics, they are given by the Maxwell equations:

$$\frac{\partial E}{\partial z} = \rho, \qquad \frac{\partial E}{\partial t} = -J, \tag{4.4}$$

where ρ and J corresponds to color charge density and color-electric current respectively. The color charge density is

$$\rho = g \sum_{j=-N_f}^{N_f} \sum_{c=1}^{3} Q_{jc} \int d^3p\, f_{jc}(p),$$

where the sum runs over quarks, antiquarks and gluons. The color-electric current is given by the sum of two contributions:

$$J = J_M + J_D, \tag{4.5}$$

where J_M is the *matter current* and J_D is the *displacement current*, following the nomenclature of Ref. [119]. Indeed, the Schwinger effect can be thought as a dielectric breakdown in which dipoles are produced by

quantum tunnelling, hence changing the local dipole moment of the vacuum and giving rise to a polarization current; then charges move in the medium due to the residual electric field producing a conductive current. We notice that, even if the equation of motion of the classical field is abelian, there is a sign of the non-abelian nature of QCD because the background field interacts with gluon quanta via J_D.

The matter current is a generalization in the case of color charges of the usual electric current density and is given by

$$J^{\mu}_{M} = g \sum_{j=-N_f}^{N_f} \sum_{c=1}^{3} Q_{jc} \int \frac{d^3p}{p_0}\, p^{\mu}\, f_{jc}(p).$$

The displacement current arises from the polarization of the vacuum owing to the decay of the electric field by the Schwinger mechanism; it is given by the time derivative of the local dipole moment induced by the particle pop-up from the vacuum, in the same way a time variation of the local dipole moment in a medium gives rise to a change in the local electric field [146]. The dipole moment can be computed as $2p_0/E$, where p_0 is the kinetic energy of the particles coming out from the vacuum; in the reference frame where particles are produced with vanishing longitudinal momentum the displacement current can be written as

$$J_D = \sum_{j=0}^{N_f} \sum_{c=1}^{3} Q_{jc} \int \frac{d^3p}{p_0} \frac{dN_{jc}}{d\Gamma} \frac{2p_T}{E}.$$

where the sum runs over gluon and quark-antiquark pairs. Color charges and currents present in Eq. (4.4) depend on parton distribution functions as well as the kinetic equations (4.3), hence allowing to solve field and particles equations in a self-consistent way and to take into account the back-reaction of particles on the field.

4.2 Boost-invariant 1+1D expanding color flux tube

We have widely tested the model of the chromoelectric flux tube with Schwinger particle production explained in the previous section in a static box of 5 fm sides and periodic boundary conditions for particle propagation; these results are discussed in detail in Refs. [147, 148] and provide a further check of the numerical solution of Eq. (4.3).

In this section we focus on the case of a longitudinally expanding background [147], assuming the expansion takes place along the direction of the electric field, which will be labelled as the z direction hereafter and corresponds to the beam axis in an heavy ion collision; moreover, the dynamics is assumed invariant for boosts along the longitudinal direction. This scenario is interesting because it is close to the description of the central rapidity region in the early stage of a relativistic heavy ion collision. Due to the symmetry of the system, assuming at initial time a homogeneous color-electric field in the transverse plane as well as along the beam direction, it will remain homogeneous in the transverse plane during the whole dynamical evolution, then depending only on $(z,\, t)$ coordinates. Along with the field, both the currents and the invariant distribution functions will depend only on time and longitudinal coordinate and not on transverse coordinates.

The evolution equations for the color-electric field are given by the pair of Maxwell equations (4.4), where both current and charge density are computed in the laboratory frame. Assuming boost invariance along the longitudinal direction implies that E depends only on proper time $\tau = \sqrt{t^2 - z^2}$. We can combine the two Eqs. (4.4) to form a boost-invariant equation, namely

$$\tau \frac{dE}{d\tau} = z\rho - t\, J;$$

using the well-known relations from relativistic kinematics $z = \tau \sinh \eta_s$

and $t = \tau \cosh \eta_s$ that link the spacetime coordinates t and z to the longitudinal proper time τ and the spacetime rapidity $\eta_s = \frac{1}{2} \ln \frac{t+z}{t-z}$, the previous equation can be rewritten as

$$\frac{dE}{d\tau} = \rho \sinh \eta_s - J \cosh \eta_s, \tag{4.6}$$

where the right hand side corresponds to the electric current computed in the reference frame where the time is the proper time. The previous equation is in agreement with the boost invariant form of Maxwell equation used in [119, 120].

We solve Eq. (4.6) adopting a finite difference scheme and preparing a box with a square region in the transverse plane,

$$-x^{max} \leq x \leq x^{max} \qquad \text{and} \qquad -y^{max} \leq y \leq y^{max},$$

and with cells in spacetime rapidity, fixing the range of η_s in which we distribute the produced particles as:

$$-\eta_s^{max} \leq \eta_s \leq \eta_s^{max} \qquad \text{with} \qquad \eta_s^{max} = 2.5.$$

This implementation corresponds to have a box with a longitudinal expansion since from relativistic kinematics $z^{max} = t \tanh \eta_s^{max}$, which corresponds to a wall moving at ultrarelativistic speed along the longitudinal direction.

In order to take into account the longitudinal expansion Eq. (4.3) has to be modifed as [119]

$$E \frac{dN}{d^4x d^2p_T dp_z} = \mathcal{R}(p_T) \delta(w) v, \tag{4.7}$$

where $\mathcal{R}(p_T)$ depends only on transverse momentum and is not influenced formally by the expanding geometry; the two boost-invariant variables w and v are defined as

$$w = t p_z - z p_0, \qquad v = p_0 t - z p_z;$$

$\delta(w)$ affects the longitudinal momentum distribution by forcing for the produced pairs the condition

$$p_z = \frac{z}{t} p_0 = p_T \sinh y,$$

with $p_0 = \sqrt{p_T^2 + p_z^2}$; such a condition is equivalent to assume that momentum rapidity y of the produced pair is equal to his spacetime rapidity η_s.

The procedure we implement to create pairs in the case of boost invariant longitudinal expansion is the following. At each time step and for each rapidity slice, given the value of E and of the slice volume, we compute the expected pair number N integrating Eq. (4.1) over the volume; then we distribute the N pairs uniformly in the transverse plane and with transverse momentum p_T according to the distribution in Eq. (4.2). As the pairs have to pop up from the vacuum with vanishing total and longitudinal momenta, for a given p_T we extract randomly the azimuthal angle ϕ, which uniquely determines $p_y = p_T \sin\phi$ and $p_x = p_T \cos\phi$ of one of the particles in the pair; then the momentum direction of the second particle is given by $\pi - \phi$.

In this section we study the effect of this boost-invariant longitudinal expansion on particle production from the decay of a chromoelectric flux tube with a transverse area of $1\,\mathrm{fm}^2$; moreover, for simplicity we restrict in this section to the formation of only gluon pairs through the Schwinger effect. Simulations improved with expansion of the system in three dimensions and Schwinger production of both gluons and quarks will be presented in the following section, whereas the more realistic case in which a color-electric field smoothly distributed in the transverse plane decays forming a quark-gluon plasma at RHIC and LHC energies will be treated in the next section.

We show computations at fixed value of the viscosity over entropy density ratio, choosing different values such as $\eta/s = 1, 3, 10$ and the limit case of $\eta/s \to \infty$. We have checked that calculations at fixed total cross

section give similar results. The relation among the total cross section and η/s we have used in the simulation is the Chapman-Enskog relation with an isotropic cross section (3.20). The extreme case of $\eta/s \to \infty$ corresponds to a zero total cross section, that is the case of a collisionless plasma.

4.2.1 Particles formation

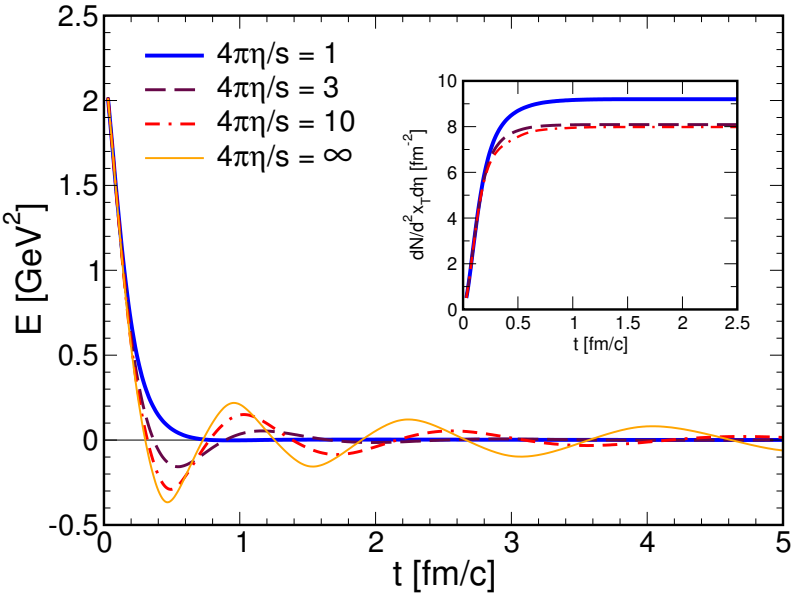

Figure 4.1: Chromoelectric field strength (main panel) and particle number produced per unit of transverse area and unit rapidity (inset panel) as a function of time. The electric field is averaged in the central rapidity region $|y| < 0.5$.

In the mail panel of Fig. 4.1 we plot the chromoelectric field strength averaged in the central rapidity region $|y| < 0.5$ as a function of time for different values of η/s. The electric field is averaged at midrapidity because in this region, within a 10% of accuracy, one has $t \approx \tau$ with t corresponding to the laboratory frame in which the system expands, so a comparison with Ref. [119], where the dynamics is followed in τ, is more meaningful. The initial value we have used in the simulations is $E(t = 0) = 2.2\,\mathrm{GeV}^2$, in agreement with the LHC case of Ref. [119],

but we obtain qualitatively similar results by varying this value. We find that the chromoelectric field experiences a rapid decay for small values of η/s. This is due to the fact that in this case the coupling among particles is large, meaning collisions are very effective in randomizing particle momenta in each cell, hence damping conductive currents that may sustain the field. On the other hand, for intermediate and large values of η/s the electric field is affected by strong fluctuations during temporal evolution.

In the inset of Fig. 4.1 we plot the number of produced gluons per unit of transverse area and unit rapidity versus time for $4\pi\eta/s = 1, 3, 10$. We find that regardless of the value of η/s we use in the simulation, the particles are produced at very early times, approximately within 0.5 fm/c, with the only expectation of very few particles produced at later times in the case $4\pi\eta/s = 10$. We have checked that changing the initial value E_0 of the electric field does not modify the production time in a considerable way unless E_0 is very small, namely $E_0 \ll 1\,\mathrm{GeV}$. Moreover, the value of η/s affects the conversion of the initial classical field to gluons only within a few percent: for example, comparing the results for $4\pi\eta/s = 1$ and $4\pi\eta/s = 3$ we find in the latter case a lowering of less than 10% on the number of particles produced.

4.2.2 Plasma thermalization

In this subsection we discuss our results about plasma thermalization and the achievement of the hydrodynamic regime. These quantities are very important because they show that the system thermalizes within a timescale in agreement with what is assumed *a priori* both in hydrodynamic simulation and in computation based on IP-Glasma initial conditions, while in our case the fast thermalization is a dynamical result of our model.

In the left panel of Fig. 4.2 we plot the proper kinetic energy density

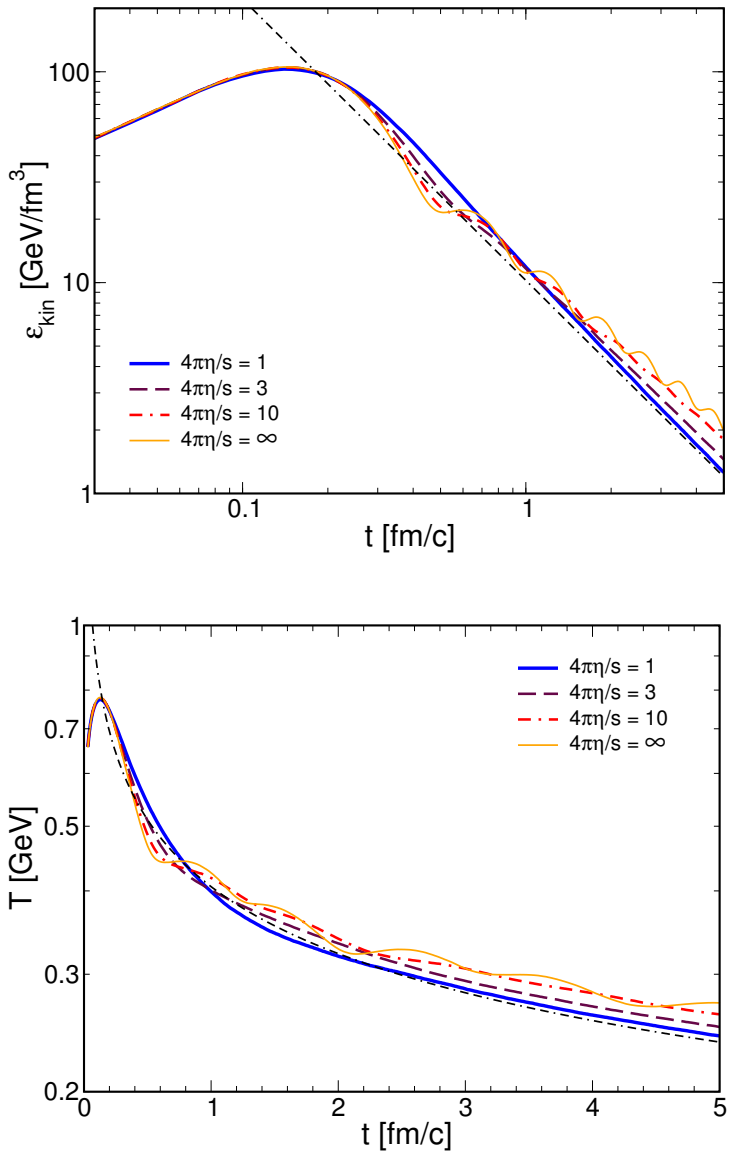

Figure 4.2: Proper kinetic energy density (top panel) and local temperature (bottom panel) as a function of time. All the quantities are averaged in the central rapidity region $|y| < 0.5$ and viscosity has been fixed using an isotropic cross section.

ε_{kin}, i.e. the kinetic energy computed in each cell in the local rest frame of the fluid, versus laboratory time; the quantity is averaged at midrapidity ($|y| < 0.5$) and computations for three different values of viscosity, fixed using an isotropic cross section, are shown. Calculations at fixed total

cross section give similar results. We find that in the case of small η/s, which corresponds to the case of a system with a large collision rate, the energy density decays asymptotically as $\varepsilon_{kin} \propto t^{-4/3}$, as is expected in the ideal hydrodynamic limit in the case of a one-dimensional expansion, in agreement with Ref. [120]. This is an interesting result because it shows, among other things, that within relativistic transport theory we are able to simulate the evolution of a fluid in the hydrodynamic regime of a very small η/s, that is large collision rate.

For the cases of larger η/s we find that the proper kinetic energy experiences a power-law decay with a superimposed oscillation pattern. The thin dashed line in the figure corresponds to $t^{-4/3}$. These results are in good agreement with those of Ref. [119].
In the right panel of Fig. 4.2 we plot the local temperature of the plasma as a function of time; it is obtained by data shown in the left panel of Fig. 4.2 by assuming a perfect gas equation of state which gives $T \propto \varepsilon_{kin}^{1/4}$ with the proportionality constant being related to the number of active degrees of freedom in the system. Our temperature is higher than the one cited in Ref. [119] because in the latter study both quarks and gluons have been considered in the plasma, while in our case we only include gluons. The thin dashed line corresponds to $t^{-1/3}$, which is the behaviour expected for a one-dimensional expansion of non-viscous fluids.

In Fig. 4.3 we plot the gluon spectra at midrapidity $|y| < 0.5$ for two different values of the viscosity: left panel corresponds to $4\pi\eta/s = 1$, right panel to $4\pi\eta/s = 10$. For each value of viscosity the spectrum at three different times is shown, namely $t = 0.2,\ 1.0,\ 5.0\,\mathrm{fm}/c$. The thin solid black line corresponds to a thermal spectrum,

$$\frac{dN}{p_T dp_T dy} \propto p_T\, \mathrm{e}^{-\beta p_T},$$

which describes a thermalized system in three spatial dimensions at temperature $T = 1/\beta$. The thermal spectrum at $t = 1\,\mathrm{fm}/c$ is computed by taking the temperature at that time from the right panel of Fig. 4.2.

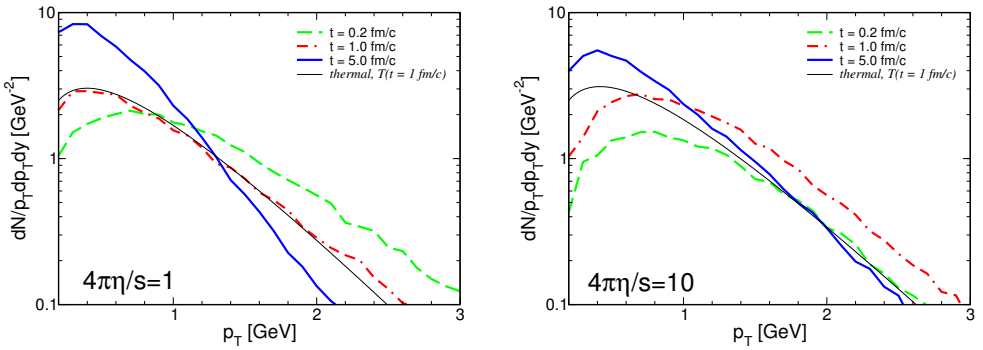

Figure 4.3: Gluon spectra at midrapidity $|y| < 0.5$ for $\eta/s = 1$ (upper panel) and $\eta/s = 10$ (lower panel). For each value of η/s the spectrum at three different times is shown.

We find that for $4\pi\eta/s = 1$ the system efficiently thermalizes within 1 fm/c, as evident by comparing the thermal spectrum (black thin line) with simulation data (dot-dashed thin red line). For $4\pi\eta/s = 10$ the spectrum of produced gluons at $t = 1\,\mathrm{fm}/c$ is in disagreement with the corresponding thermal spectrum, meaning the system is not completely thermalized in three dimensions. Moreover, the very mild change in the slope of the spectrum we measure from $t = 1\,\mathrm{fm}/c$ to $t = 5\,\mathrm{fm}/c$ shows that the system does not cool down efficiently in this case, as is expected because the larger the viscosity the larger is the energy dissipated into heat; therefore the system cools down more slowly than in the case of small viscosity, which can be confirmed also by looking at the orange curve in Fig. 4.2.

4.2.3 Plasma isotropization

In this subsection we show our results for the evolution of the ratio P_L/P_T for the system produced by the decay of the color field, where P_L and P_T stand for longitudinal and transverse pressure respectively. The computation of this quantity is important because, as we will discuss, at initial time the system is very anisotropic, but the interactions and the decay of the classical field might lead to an almost isotropic state

during the early evolution of the system. Moreover, it is a common assumption of hydrodynamic calculations that the quark-gluon plasma is very close to an isotropic system and isotropization occurs quickly: we show how the quick (partial) isotropization scenario can be realized within a consistent calculation. The results of this subsection, along with those about thermalization shown in the previous one, allow to draw a picture in which thermalization and isotropization arise within the time range required by hydrodynamic simulations, therefore offering a dynamical justification to early thermalization and isotropization of hydrodynamics.

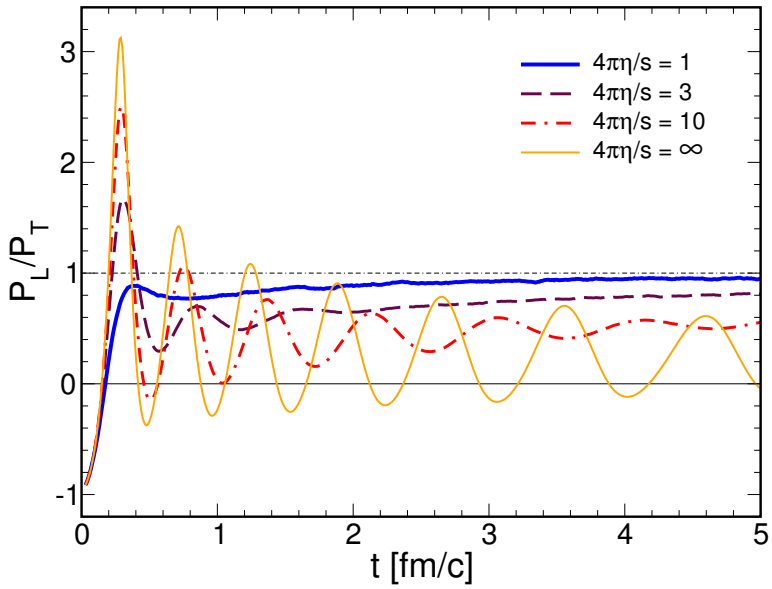

Figure 4.4: Ratio of longitudinal pressure over transverse pressure P_L/P_T as a function of time. The pressures are averaged in the central rapidity region $|y| < 0.5$. The different lines correspond to different values of viscosity η/s, which has been fixed using an isotropic cross section.

In Fig. 4.4 we plot the time evolution of the ratio P_L/P_T for several values of η/s. The pressures are computed cell by cell in the local rest frame of the fluid and then averaged in the rapidity range $|y| < 0.5$. The initial longitudinal pressure is negative and $P_L/\varepsilon = -1$, because at initial time the system is made of pure chromoelectric field for which the

energy-momentum tensor is given by

$$T^{\mu\nu} = \mathrm{diag}\left(\varepsilon, P_T, P_T, P_L\right),$$

where $\varepsilon = E^2/2$, $P_T = \varepsilon$ and $P_L = -\varepsilon$. Then, as soon as particles are produced, they give a positive contribution to the longitudinal pressure and the field magnitude decreases, eventually leading to a positive pressure. We find that, regardless of the value of η/s, the time needed to the total longitudinal pressure to be positive is about $0.2\,\mathrm{fm}/c$. Collisions among particles tends to bring the system towards an isotropic state, for which $P_L = P_T$. In the case of a static box simulation, regardless of the value of η/s, the system is very efficient in removing the initial pressure anisotropy, since in this case collisions always lead to the equilibrium state with $P_L/P_T = 1$, even though isotropization times are different for different viscosities [147, 148]. Nevertheless, in the case of an expanding box collisions may not have enough time to bring the system to a perfect isotropic state, especially for large viscosities, because at a certain point during the expansion the distance between particles become greater than their mean free path.

We notice from Fig. 4.4 that for $4\pi\eta/s = 1$ the large collision rate among particles remove the initial pressure anisotropy quite efficiently and quickly: in this case $P_L/P_T \simeq 0.8$ within $0.6\,\mathrm{fm}/c$; then the ratio tends to increase towards 1 within the time evolution of the system. This would justify the use of viscous hydrodynamics which commonly starts simulations at $\tau_0 \approx 0.6\,\mathrm{fm}/c$ assuming an isotropic state at that time.

On the other hand, for larger viscosities the system reaches a less isotropic state with $P_L/P_T < 1$ and the oscillations of the electric field strength in Fig. 4.1 lead to many oscillations of P_L/P_T, which are damped by collisions during the system evolution: the larger the η/s of the fluid, the larger are the oscillations of P_L/P_T and the lower is the maximum value reached by the pressure ratio; moreover such oscillations are damped

more efficiently for smaller viscosities. We can better understand this correlation comparing the cases $4\pi\eta/s = 1$ and $4\pi\eta/s = 10$ in Fig. 4.4: in the latter case P_L/P_T experiences many oscillations which follow the alternation of maxima of $|E|$, corresponding to minima of P_L (since the field gives a negative contribution to P_L), and zeros of E, corresponding to maxima of P_L; moreover, at large times P_L/P_T is quite smaller than one. The different behaviour of the temporal evolution of the pressure ratio we find for different values of the viscosity is in agreement with the results of Ref. [119].

In Fig. 4.5 we show the temporal evolution of the ratios P_L/ϵ and P_T/ϵ, where ϵ corresponds to the total energy density that is the sum of the energy densities of particles and fields. The results for three different viscosities are plotted: $4\pi\eta/s = 1$ in the top panel, $4\pi\eta/s = 3$ in the middle panel and $4\pi\eta/s = 10$ in the bottom panel. In all of the three plots the red solid curve corresponds to P_L/ϵ and the thin green curve to P_T/ϵ, whereas the thin black dashed line indicates to the conformal isotropic limit $\epsilon = 3P$. Our results are in agreement with the same quantities computed in Ref. [52], where a classical Yang-Mills simulation with a 3 + 1D expanding geometry is considered. Even though the theoretical framework of Ref. [52] is different, it is very interesting that the final results are comparable to those of our Fig. 4.5. In the weakest coupling case considered in Ref. [52], namely $g = 0.1$, P_L asymptotically approaches zero, a behaviour which we might obtain using viscosities larger then $\eta/s = 10/4\pi$ that we have not considered in the present study. However, the case $g = 0.5$ of Ref. [52] produces P_L/ϵ and P_T/ϵ which lie between our results for $\eta/s = 3/4\pi$ and $\eta/s = 104\pi$.

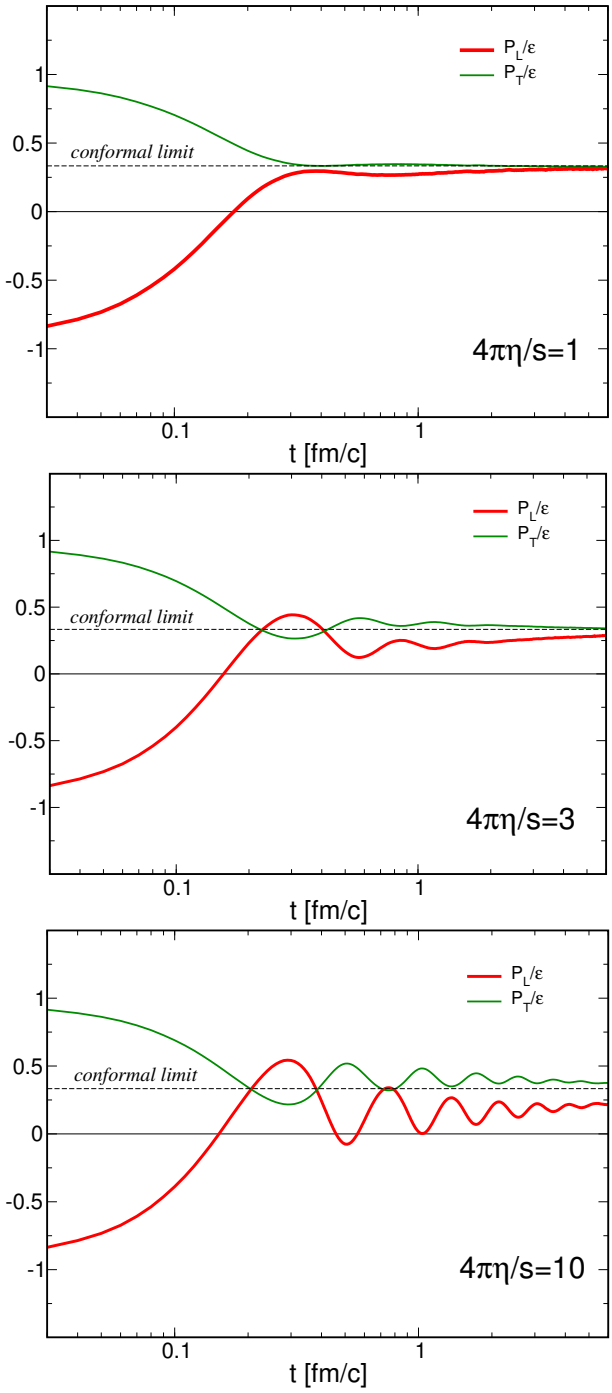

Figure 4.5: Ratios P_L/ϵ and P_T/ϵ versus time for $4\pi\eta/s = 1$ (top panel), $4\pi\eta/s = 3$ (middle panel) and $4\pi\eta/s = 10$ (bottom panel). All the quantities are averaged in the central rapidity region $|\eta| < 0.5$ and viscosity has been fixed using an isotropic cross section.

4.3 Production and 3+1D expansion of a quark and gluon plasma

The 1+1D expansion case discussed in the previous section is interesting because a longitudinal expansion characterizes the very early times on ultra-relativistic heavy ion collisions. In this section we show results for the more realistic case of a 3+1D expanding flux tube with the same initial condition of the one-dimensional expanding system: a homogeneous longitudinal color-electric field. Furthermore, in this case we implement the Schwinger conversion of color field not only in gluon pairs but also in quark-antiquark pairs, restricting to the case $N_f = 2$ in which only quarks with flavors u and d (and the corresponding antiquarks $\bar{u}$ and $\bar{d}$) can be produced by means of the Schwinger formula (4.1).

While in the longitudinal expansion transverse components of the color-electric field do not develop since J_x and J_y are zero due to periodic boundary conditions in the transverse plane, in the three-dimensional expansion we allow for formation of longitudinal as well as transverse components of currents and field. As for the case of the 1+1D expansion, we neglect the magnetic component of the initial color field. Nevertheless, in this case a magnetic field can be produced dynamically, even if absent in the initial condition, because of the transverse components of the electric field ($d\mathbf{B}/dt = -\nabla \times \mathbf{E}$); however, we have checked that the magnitude of the transverse components of $\mathbf{E}$ as well as of its curl are negligible, hence the magnetic field behaves just as a very small fluctuation and should not affect the dynamics of the plasma.

For a three-dimensional expanding flux tube, the Maxwell equations for the color-electric field are given by

$$\nabla \cdot \mathbf{E} = \rho, \qquad \frac{\partial \mathbf{E}}{\partial t} = -\mathbf{J}, \tag{4.8}$$

where t is the time in the laboratory frame and the current and the charge density depend also on transverse coordinates x and y. The initial field is

only longitudinal (as in the case of one-dimensional expansion), whereas transverse components of **E** will be generated by transverse currents according to Eq. 4.8.

Even in this case we assume boost invariance along the longitudinal direction; this implies that E_z depends on the proper time τ. Combining the two Eqs. 4.8 we obtain the following equation for the longitudinal component of the electric field:

$$\frac{dE_z}{d\tau} = \rho \sinh \eta_s - J_z \cosh \eta_s - \sinh \eta_s \left(\frac{\partial E_x}{\partial x} + \frac{\partial E_y}{\partial y} \right), \tag{4.9}$$

where the color-electric current and charge density are computed in the local rest frame of the fluid. The equations for the transverse electric field components are:

$$\frac{\partial E_x}{\partial t} = -J_x, \qquad \frac{\partial E_y}{\partial t} = -J_y. \tag{4.10}$$

In order to solve Eqs. (4.9) and (4.10) we use a finite difference scheme and a discretized spacetime using (x, y, η_s) coordinates.

The numerical implementation of the simulation is analogous to that used for the 1+1D expanding system of the previous section, but in this case there are no boundary conditions on the transverse plane. Even the procedure of particles production is equivalent to that used for the longitudinal expansion, but with Eq. (4.7) evaluated in each cell in (x, y, η_s) rather than in rapidity slices.

In the following we discuss the effect of a three-dimensional expansion on particle production from the decay of a flux tube with a transverse area of $28\,\mathrm{fm}^2$ and with homogeneous initial chromoelectric field $E_z = 2.2\,\mathrm{GeV}^2$; furthermore, unlike the 1+1D case in which we restricted to the formation of only gluon pairs, in this section we allow for production of both gluon and quark pairs through the Schwinger mechanism.

These simulations constitute the base and a numerical check for the results presented in the next chapter. Indeed, in order to describe photon

production of heavy ion collisions, we will consider more realistic initial conditions with a color-electric field smoothly distributed in the transverse plane that decays forming a quark-gluon plasma which expands in all spatial directions and emits photons through some basic scattering processes.

As in the previous section, we show computations at fixed value of the viscosity over entropy density ratio ($\eta/s = 1, 3, 10$) using the Chapman-Enskog formula with an isotropic cross section (3.20) to relate total cross section to the fixed η/s.

4.3.1 Conversion of color field to particles

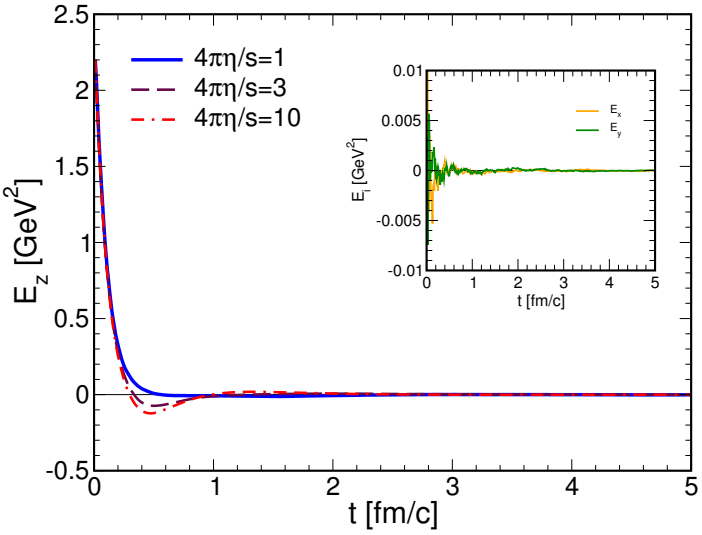

Figure 4.6: Longitudinal (main graph) and transverse (inset) components of the color-electric field strength averaged in the central rapidity region $|y| < 0.5$ as a function of time. The different curves correspond to different values of η/s.

In Fig. 4.6 we plot the components of the color-electric field strength averaged in the central rapidity region $|y| < 0.5$ as a function of time. The behaviour of the longitudinal component E_z, plotted in the main panel for three different values of viscosity, is similar to the one of the 1+1D case treated in the previous section; nevertheless, after a quick decay in less

than 0.5 fm/c for all values of viscosity, E_z experiences fluctuations for large viscosity that are weaker than those found in the one-dimensional case, as we can see comparing maroon dashed lines ($4\pi\eta/s = 3$) and red dot-dashed lines ($4\pi\eta/s = 10$) of this figure and Fig. 4.1 (main panel); this is due to the fact that in the 3+1D case the transverse expansion of particles damps longitudinal currents which sustain the electric field. In the inset graph the transverse components of the electric field are shown for $4\pi\eta/s = 1$; such components are tiny and do not affect the dynamics of the system, since there is no substantial formation of electric currents in the transverse plane.

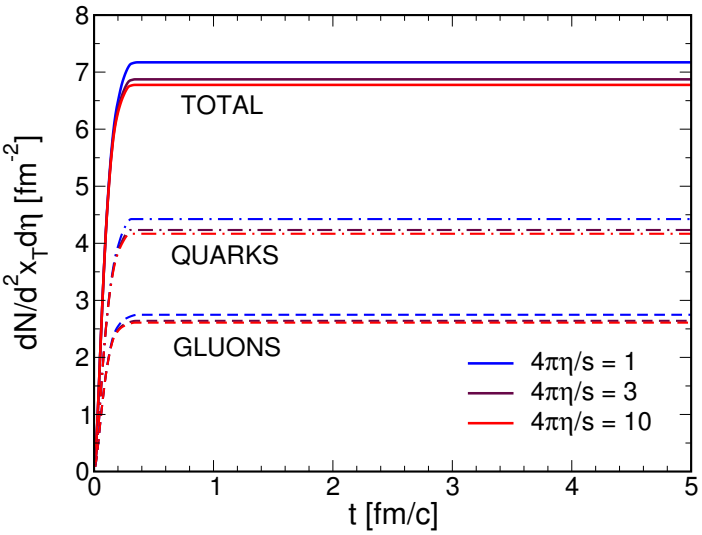

Figure 4.7: Particle number produced per unit of transverse area and rapidity as a function of time. Full lines correspond to the total particle number, while with dashed and dot-dashed lines are indicated gluon number and quark number respectively. The different curves correspond to different values of η/s.

In Fig. 4.7 we show the number of particles produced per unit of transverse area and rapidity versus time for three values of viscosity: besides the total number of particles produced (full lines), the gluon number (dashed lines) and the quark number (dot-dashed lines) are plotted. We find that as in the 1+1D result particles are produced very early, within

0.5 fm/c, independently of the value of η/s, which affects very mildly the conversion of the initial field to a plasma. For a system of massless particles in a volume V in equilibrium at a temperature T the particle number can be computed as

$$N = \rho V = \gamma \frac{V}{(2\pi)^3} \int d^3p \, \mathrm{e}^{-p/T} = \gamma \frac{VT^3}{\pi^2},$$

where γ is the degeneracy factor; then the ratio between quark and gluon numbers reduces to the ratio of the degeneracies, which for $N_f = 2$ is given by $\gamma_q/\gamma_g = 24/16 = 1.5$. We can see from Fig. 4.7 (right panel) that the quarks over gluons ratio is about 1.6 in our case, meaning that when the field is totally converted to particles the system has reached a nearly chemically equilibrated phase.

We notice from Fig. 4.7 that this mechanism of particle production allows a very quick quark-gluon plasma formation, with a copious amount of quarks; this is in disagreement with previous works supporting a scenario in which at initial times the high energy system is made mainly of gluons, obtained from the decay of the glasma flux tubes, and the dynamical evolution lead to a locally thermalized and nearly chemically equilibrated quark-gluon plasma. Inelastic collisions would anyway quickly drive the system to a chemical equilibrated plasma. Nevertheless those studies end up with a final state which consists mainly of quark-antiquark pairs rather than gluons, in agreement with our result. In the next chapter we will discuss the effect of this fast quark-gluon plasma formation on photon production, since processes that emit photons always involve quarks.

4.3.2 Plasma isotropization and thermalization

We now study thermalizaton and isotropization of the quark-gluon plasma for a realistic 3+1D expanding system.

In Fig. 4.8 the ratio of longitudinal pressure P_L over transverse pressure P_T as a function of time is plotted. Pressures are computed cell by

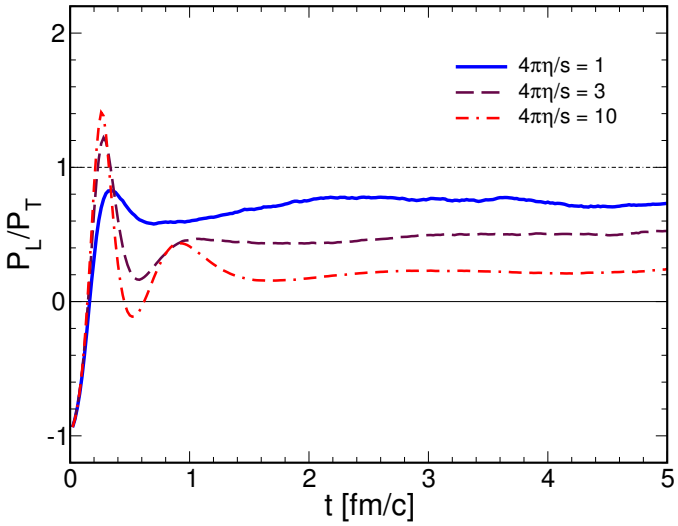

Figure 4.8: Longitudinal over transverse pressure ratio as a function of time for several values of η/s. Pressures are averaged at mid-rapidity $|y| < 0.5$ and in a central region of the transverse plane.

cell in the local rest frame of the fluid and then averaged in the midrapidity region $|y| < 0.5$ and in a central portion of transverse plane. At initial time $P_L/P_T = -1$ since the initial color-electric field is purely longitudinal, as in the case of the one-dimensional geometry discussed in the previous section. While particles pop-up from the vacuum, producing a positive longitudinal pressure, the field strength decreases; at $\sim 0.2\,\mathrm{fm}/c$ the longitudinal pressure and then the pressure ratio become positive, regardless of the value of the viscosity. The qualitative behaviour of the pressure ratio is similar to that found in the 1+1D case, as we can see comparing this figure to Fig. 4.4: the larger the viscosity of the fluid the larger are the oscillations of P_L/P_T, which follow those of the field strength. Therefore oscillations of P_L/P_T are more efficiently damped in this case than in the one-dimensional expansion: while in the latter case oscillations affect all the evolution of the pressure ratio almost for $4\pi\eta/s = 10$, in the 3+1D expansion oscillations of P_L/P_T are damped in the first 3 fm/c for $4\pi\eta/s = 10$ and even early for smaller viscosities. For $4\pi\eta/s = 1$ the pressure ratio is about 0.6 at $1\,\mathrm{fm}/c$, then reaching the

value 0.7 as the most isotropic value, hence maintaining a higher level of anisotropy respect to the 1+1D case; this fact, visible also for larger viscosities, is due to the transverse expansion which, causing a quicker dilution of the system, makes collision less efficient in isotropizing particle momenta.

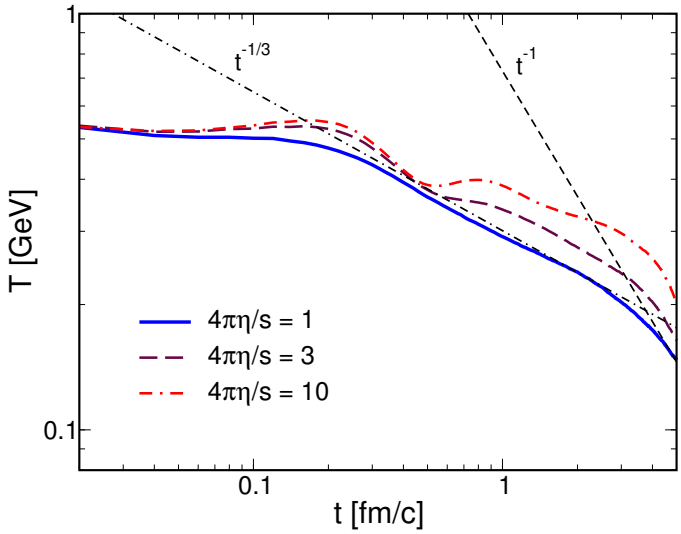

Figure 4.9: Temporal evolution of the local temperature, averaged in the central rapidity region $|y| < 0.5$ and in a central portion of the transverse plane. The different curves correspond to different values of η/s.

In Fig. 4.9 we plot the temporal evolution of the local temperature of the fluid, defined by the ratio $T = E/3N$ as in the case of a thermalized system. T is evaluated in the local rest frame of the fluid and averaged in the same rapidity and transverse plane regions of the pressures. We find that the temperature scales as $t^{-1/3}$ for about $t = 1 - 2$ fm and as t^{-1} for $t > 4$ fm, meaning the longitudinal expansion characterizes early times after particles production ceases while the three-dimensional expansion becomes dominant at later times. These time dependences of temperature are in agreement with expectations from ideal hydro for a longitudinal and three-dimensional expansion respectively, see for example [67, 149].

4.3.3 Effect of quark production

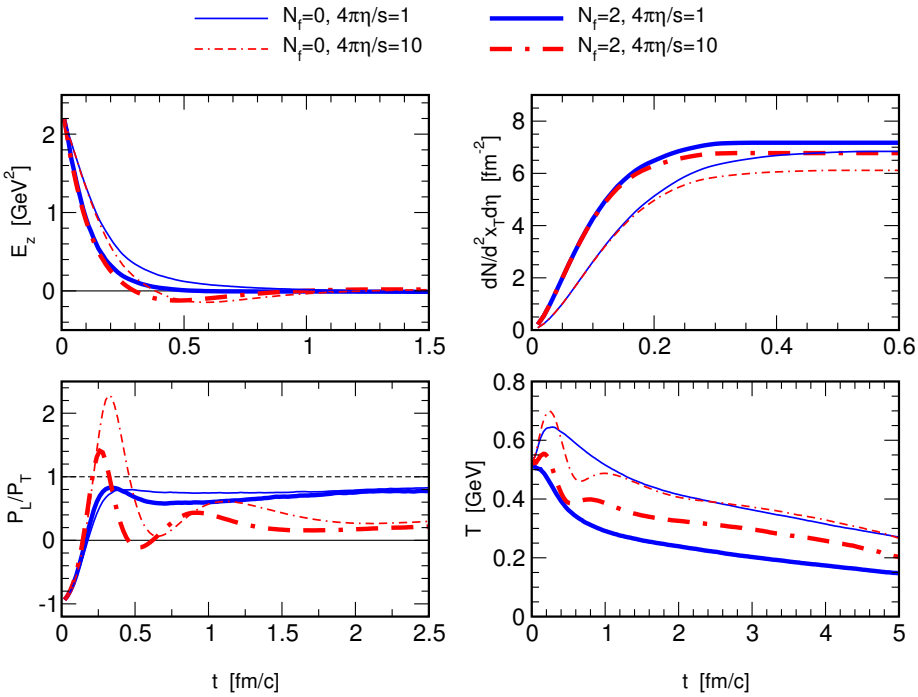

Figure 4.10: Comparison of longitudinal field decay (upper left panel), total particle number per unit transverse area and rapidity (upper right panel), pressure ratio P_L/P_T (lower left panel) and local temperature T (lower right panel) as a function of time in the case of a gluon plasma (thin curves) and a quark-gluon plasma (thick lines). Field strength, pressures and temperature are averaged at midrapidity $|y| < 0.5$ and in a central region of the transverse plane. The different colors correspond to different values of viscosity η/s.

In Fig. 4.10 we compare the quantities previously discussed with those obtained with simulations starting with the same initial condition (tube with transverse area of $28\,\mathrm{fm}^2$ and with constant longitudinal chromo-electric field $E_z = 2.2\,\mathrm{GeV}^2$) but for creation of only gluon pair by the Schwinger effect. In the upper left panel the field strength E_z, in the upper right panel the total particle number per unit rapidity and transverse area $d^2N/d^2x_T d\eta$, in the lower left panel the pressure ratio P_L/P_T and in the lower right panel the local temperature $T = E/3N$ are plotted as a function of time. Thick and thin lines correspond to simulations

with $N_f = 2$ and $N_f = 0$ respectively, whereas blue and red curves indicate computation with η/s equal to $1/4\pi$ and $10/4\pi$ respectively. Field strength, pressures and temperature are averaged at midrapidity $|y| < 0.5$ and in a central region of the transverse plane. All the quantities show that in the quark-gluon plasma formation case the dynamics of field conversion to particles as well as of equilibration of the system is quicker than in the case of only gluon creation; this is simply due to the fact that in the latter case there are less channels through which the color field can convert in particle pairs by means of the Schwinger mechanism. However, the qualitative behaviour and timescales of all the quantities considered does not change in a remarkable way when turning from quark-gluon plasma formation to the case in which only gluon are produced.

CHAPTER 5

PRE-EQUILIBRIUM CONTRIBUTION TO PHOTON PRODUCTION

As introduced in Chapter 2, radiation of photons is considered to be an important and efficient probe to scrutinise the properties of the quark-gluon plasma. While hadrons are emitted from the freeze-out surface after suffering also hadronic scatterings, photons are radiated during the whole spacetime history of the expanding fireball. Because of their electromagnetic nature and being $\alpha_{em} \ll \alpha_s$, photons mean free path is much larger then the typical size of the system; then, once produced, photons leave the fireball almost undisturbed, and reach the detector with an unaltered imprint of the circumstances of their production.

In this chapter we discuss our results on the spectrum and the elliptic flow of photons emitted from the quark-gluon plasma produced in heavy ion collisions at both RHIC and LHC energies. Simulating the space-time evolution of the fireball by solving the relativistic Boltzmann transport equation and including two-particle scattering processes with photon emission allows us to make a first step in the description of photons produced both in the pre-equilibrium phase and in the thermal QGP phase within a unique theoretical framework.

Therefore our approach allow us to consider not only a standard Glauber initialization, like the one commonly used in hydro calculations, but also an initial condition based on the dynamics of a classical gluon field which produces quarks and gluons since the very beginning of the evolution by means of the Schwinger effect.
With this study we aim at spotting the impact of early stage non-equilibrium dynamics on the photon production.

5.1 Direct Photons

Although radiation of photons is a promising tool to probe the QGP, a big issue concerning his diagnostics is the large background. Indeed, we are interested only in photons emerging directly from a collision process, called *direct photons*, but more than 90% of all detected photons - the inclusive photon yield - come out from the decay of final state hadrons. This huge background have to be eliminated in order to recover the direct photon signal; several experimental techniques have been developed to this end, such as invariant mass analysis [150, 151], mixed event analysis [152], internal conversion method [153, 154], tagging of decay photons technique [155, 156]. However, the identification of decay photons is a really complicated task and experimental data on direct photon production could not be obtained very accurately so far, especially those on flow observables.

In a heavy ion collision there are different sources of direct photons, depending of their origin from different stages of the expanding fireball formed after the collision:

- *prompt* photons, which originate from initial hard scatterings;
- *pre-equilibrium* photons, produced before the medium gets thermalized;

- *thermal* photons from the quark-gluon plasma as well as from the hadron gas;
- *jet conversion* photons, which come out from passage of jets through the plasma.

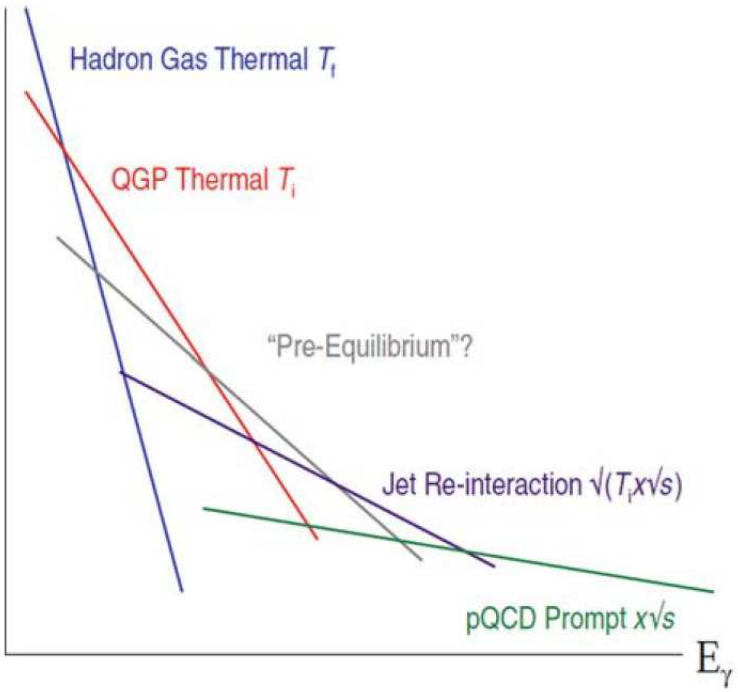

Figure 5.1: Schematic diagram of different sources of photons and their relative p_T spectra. Figure taken from [157].

In Fig. 5.1 we represent qualitatively the contribution of each photon source to the direct photon spectrum. Experiments can not distinguish between the different sources, hence theoretical models are necessary to identify these sources and their relative importance in the spectrum. In particular, with our approach we are interested in investigating the properties of pre-equilibrium photons and grasping their effect on photon observables of ultra-relativistic heavy ion collisions.

5.2 Implementation of photon production

At the leading order in the electromagnetic and strong coupling, the photon production processes are the *QCD Compton scattering* and the *quark-antiquark annihilation* shown in the diagrams of Fig. 5.2, which generate the leading logarithmic contribution to the photo-production rate. Although these processes were originally believed to give the complete leading order contribution [158–160], it was later demonstrated that the two-to-three processes known as *bremsstrahlung* and *inelastic pair annihilation* contain collinear enhancements which make them contributing at the same order in coupling, $O(\alpha_{em}\alpha_s)$, as the two-to-two processes of Fig. 5.2 [161–163]. A complete calculation in leading order, including also the *Landau-Pomeranchuk-Migdal* (LPM) effect (a suppression of these processes due to multiple scatterings during the photon emission), was first made by Arnold, Moore and Yaffe [163] which provided a parametrised form for the rates.

The great majority of models available until now, especially those using hydrodynamics formulations, integrate these rates over a spacetime volume in order to obtain the the total photon emission. This procedure assumes, among other things, that the system producing photons is in local thermal equilibrium, therefore this approach cannot describe photon emission in the pre-equilibrium phase where the system is out of equilib-

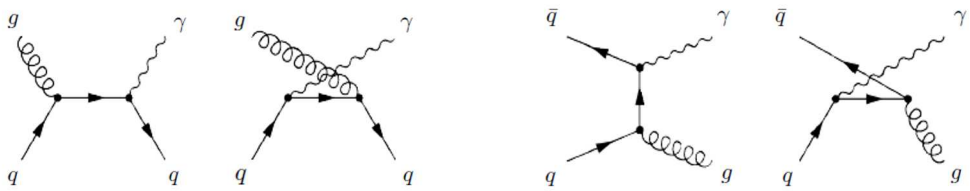

(a) QCD Compton scattering (b) quark-antiquark annihilation

Figure 5.2: Feynman diagrams of the two-to-two particle processes constituting the dominant contribution to the photo production rate. Time may be viewed as running from left to right.

rium. We go beyond this approach by computing the collision integral with the inclusion of the scattering processes rather than integrating a thermal rate.

For this thesis we have implemented in the collision integral of the relativistic Boltzmann equation the $2 \to 2$ scatterings of Fig. 5.2, i.e. the QCD Compton scattering $q/\bar{q} + g \to q/\bar{q} + \gamma$ and the quark-antiquark annihilation $q + \bar{q} \to g + \gamma$, whose differential cross sections, in terms of the Mandelstam variables s, t and u [1], are given respectively by

$$\begin{aligned} \frac{d\sigma^{compton}}{dt} &= -\frac{\pi\alpha\alpha_s}{3s^2}\frac{u^2+s^2}{us}, \\ \frac{d\sigma^{annihil}}{dt} &= \frac{8\pi\alpha\alpha_s}{9s^2}\frac{u^2+t^2}{ut}. \end{aligned} \tag{5.1}$$

We have done numerical tests of our implementation of photons production processes, comparing the results of our code with known analytical results.

The thermal emission rate of photons with energy E and momentum p from a system at temperature T is related to the imaginary part of the photon self-energy by the following relation

$$E\frac{dR}{d^3p} = \frac{-2}{(2\pi)^3}\mathrm{Im}\Pi^{R,\mu}_{\mu}\frac{1}{\mathrm{e}^{E/T}-1}, \tag{5.2}$$

where $\Pi^{R,\mu}_{\mu}$ is the retarded photon self-energy at finite temperature T. This relation is valid in the perturbative [164, 165] as well as non-perturbative [166] limits. It is also valid to all orders in the strong interactions and to order e^2 in the electromagnetic interactions. If the photon self-energy is approximated by carrying out a loop expansion to some finite order, then the formulation of Eq. (5.2) is equivalent to relativistic kinetic theory. This connection was first illustrate by Kapusta, Lichard and Seibert [158], which computed analytically thermal emission rates of photons.

[1] For a generic two-to-two scattering $a + b \to c + d$ the Mandelstam variables are invariant quantities encoding energy, momentum and angles of particles in the process and are defined as $s = (p_a + p_b)^2 = (p_c + p_d)^2$, $t = (p_a - p_c)^2 = (p_b - p_d)^2$ and $u = (p_a - p_d)^2 = (p_b - p_c)^2$.

Using relativistic kinetic theory formulation, the contribution to the photon production rate of a process i can be written as [158, 159]

$$\begin{aligned} R_i =& \mathcal{N} \int \frac{d^3p_1}{(2\pi)^3 2E_1} \frac{d^3p_2}{(2\pi)^3 2E_2} \frac{d^3p_3}{(2\pi)^3 2E_3} \frac{d^3p}{(2\pi)^3 2E} \left|\mathcal{M}_i\right|^2 \\ & \times (2\pi)^4 \delta^{(4)}(p_1 + p_2 - p_3 - p) f_1(E_1) f_2(E_2) \left[1 \pm f_3(E_3)\right], \end{aligned} \tag{5.3}$$

where $\mathcal{N}$ is a degeneracy factor, E and p are respectively energy and momentum of the emitted photon, $\mathcal{M}_i$ represents the transition amplitude for the considered process and the functions f_i are the Fermi–Dirac or Bose–Einstein distribution. The plus or minus sign in the last part of the equation accounts for Bose enhancement or Pauli suppression respectively. For massless particles the amplitude of a process can be computed through the relation $|\mathcal{M}|^2 = 16\pi\, s^2\, d\sigma/dt$ using the appropriate differential cross section, which for the QCD Compton scattering and the quark-antiquark annihilation is given by Eq. (5.1).

The total cross section can be obtained by integrating $d\sigma/dt$ of the process under consideration over t. The differential cross sections (5.1) have a singularity at $t = 0$ and/or $u = 0$ and the total cross section is infinite as the processes involve exchange of massless particle. A simple way to obtain finite cross section consists in isolating the region of phase space causing the divergences, performing the integration over

$$-s + k_c^2 \leq t \leq -k_c^2, \qquad 2k_c^2 \leq s \leq \infty, \tag{5.4}$$

being $T^2 \gg k_c^2 > 0$ an infrared cutoff. In the limit $k_c^2 \to 0$ and using Boltzmann distributions in the final state, the photon emission rates for the two processes in Fig. 5.2 reads [158]

$$\begin{aligned} E\frac{dR^{compton}}{d^3p} &= \frac{5}{9}\frac{2\alpha_{em}\alpha_s}{\pi^4} T^2 \mathrm{e}^{-E/T} \left[\ln\left(\frac{4ET}{k_c^2}\right) + \frac{1}{2} - C_{Euler}\right], \\ E\frac{dR^{annihil}}{d^3p} &= \frac{5}{9}\frac{2\alpha_{em}\alpha_s}{\pi^2} T^2 \mathrm{e}^{-E/T} \left[\ln\left(\frac{4ET}{k_c^2}\right) - 1 - C_{Euler}\right]. \end{aligned} \tag{5.5}$$

In these equations the factor 5/9 arises from the sum of the squares of the electric charges of the u and d quarks, the factor $\alpha_{em}\alpha_s$ comes from the

topological structure of the diagrams, a factor T^2 comes from phase space which gives the overall dimension to the rate, $\mathrm{e}^{-E/T}$ is the Boltzmann factor for photons of energy E and the logarithm arises due to the infrared behavior. If the infrared divergence is regulated in a different way, for example by giving the quarks a thermal mass rather than putting a cutoff on the four-momentum transfer, the constant terms in parentheses may change but the dominant logarithmic behaviour is still present.

In order to check if we have correctly implemented photon production processes, we performed simulations in a static box of volume V at fixed temperature T with periodic boundary conditions for particle propagation and computed the thermal photon emission in such a condition. In this case, assuming a system of massless particles in which there are no external forces, the transport equation (3.3) becomes:

$$p \cdot \partial_x f(x,p) = \mathcal{C}[f](x,p), \tag{5.6}$$

which we solve using the stochastic algorithm and the test particle method described in Chapter 3. As we have already mentioned in the previous chapter, for such a system in a volume V in equilibrium at temperature T the particle number is given by

$$N = \rho V = \gamma \frac{V}{(2\pi)^3} \int d^3p \, \mathrm{e}^{-p/T} = \gamma \frac{VT^3}{\pi^2},$$

where γ is the degeneracy factor. These particles are distributed uniformly in coordinate space while in momentum space, being the system in thermal equilibrium, we employ the Boltzmann distribution:

$$\frac{dN}{N\, E^2\, dE} = \frac{1}{2T^3} \mathrm{e}^{-E/T}.$$

We simulated thermal emission putting in the collision integral the cross sections given by Eq. (5.1) with the strong running coupling constant α_s appropriate for the box temperature. Turning on separately one process or the other, we computed the rate $R = dN/d^4x$, i.e. the number of

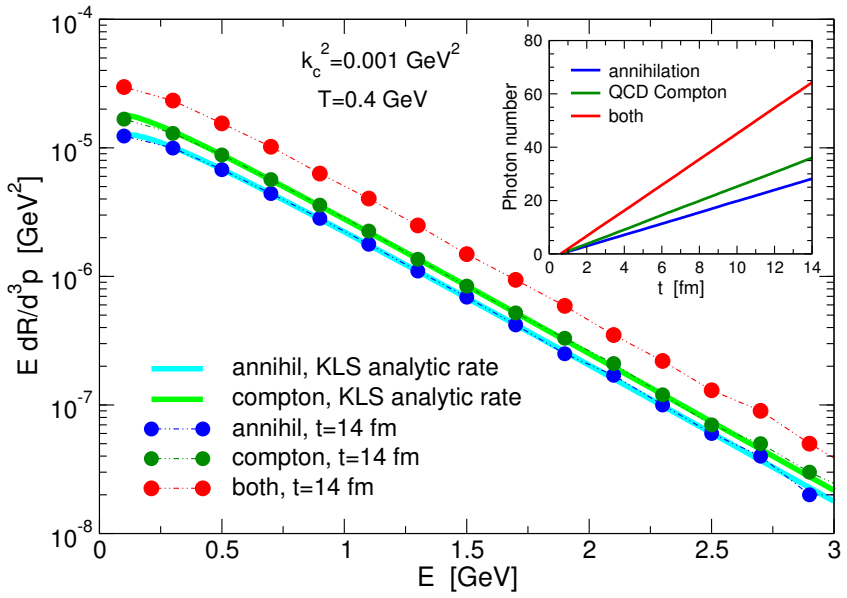

Figure 5.3: Comparison of photon production rates for QCD Compton scattering (dark green points) and quark-antiquark annihilation (blue points) with KLS analytic rates [158] of the two processes (full lines). For completeness, the result with photon emission from both processes is also shown (red points). The simulations are made in a static box at $T = 0.4\,\mathrm{GeV}$.

reactions per unit time per unit volume which produce a photon, and compared it with the correspondent analytical KLS result in Eq. 5.5 for several values of temperature. As we can see from Fig. 5.3, where the case with $T = 0.4\,\mathrm{GeV}$ is reported, the rates coming out from our simulations agree very well with the KLS analytical computations.

In order to perform more realistic simulations of QGP photon production, which we will show in the next section, we have used in our code the differential cross sections 5.1 with an effective temperature-dependent strong coupling constant such to reproduce the complete leading order photon production rate [163] for the whole range of temperature explored in relativistic heavy ion collisions. In Fig. 5.4 we compare the photon spectrum obtained with our simulation in a static box at three different temperatures with the correspondent analytical result evaluated by AMY [163], showing a very good agreement for $p_T \gtrsim 0.7\,\mathrm{GeV}$.

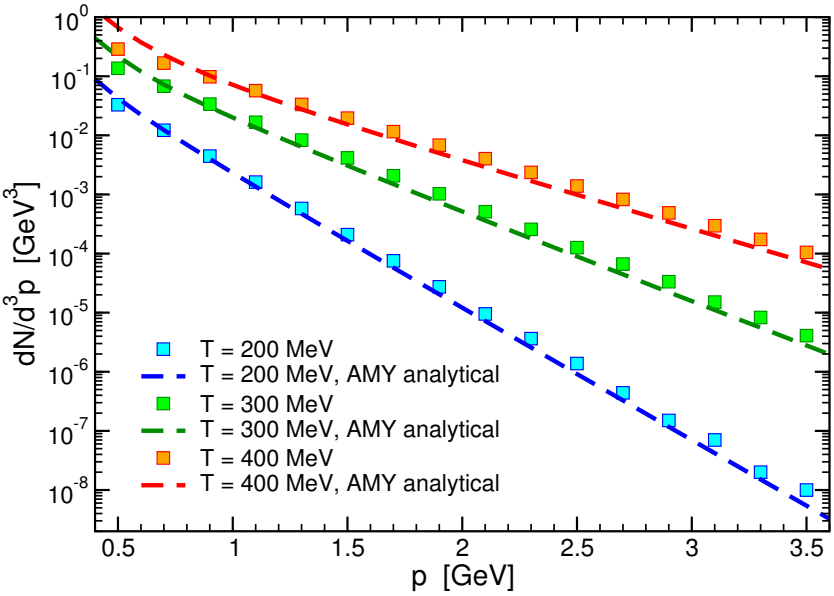

Figure 5.4: Comparison of photon production spectra obtained in our simulation (squares) with the correspondent AMY analytical results [163] (dashed lines). The three data sets correspond to $T = 0.4\,\mathrm{GeV}$ (orange points), $T = 0.3\,\mathrm{GeV}$ (green points) and $T = 0.2\,\mathrm{GeV}$ (cyan points). In our simulations $k_c = 0.1\,\mathrm{GeV}^2$ and an effective temperature-dependent strong coupling constant are used.

5.3 Effect of pre-equilibrium on photon production

In this section we discuss the effect of pre-equilibrium stage on direct photon production. For this purpose we compare simulations starting at $t_0 = 0.01\,\mathrm{fm}/c$ with the model described in the previous chapter to simulations with an equilibrium initial condition.

For simulations at RHIC energy we refer to Au-Au collisions at $\sqrt{s} = 200\,A\mathrm{GeV}$, for those at LHC we refer to Pb-Pb collisions at $\sqrt{s} = 2,76\,A\mathrm{TeV}$; in this study we focus on collisions at 20-40% centrality, which corresponds to an impact parameter $b \simeq 8.1\,\mathrm{fm}$ at RHIC and $b \simeq 8.5\,\mathrm{fm}$ at LHC.

The equilibrium initialization is based on the Glauber model, with a spacial distribution given by the standard mixture $0.85N_{part} + 0.15N_{coll}$

and a thermalized momentum spectrum in the transverse plane at the initial temperature T_0: simulations of the plasma fireball created at RHIC starts at $t_0 = 0.6\,\mathrm{fm}/c$ with $T_0 = 340\,\mathrm{MeV}$; for simulations at LHC energy the maximum temperature is $T_0 = 510\,\mathrm{MeV}$ at the starting time $t_0 = 0.3\,\mathrm{fm}/c$. We named these cases *Th-Glauber* following the nomenclature of Ref. [106], while we refer to simulations with the Abelian flux tube model described in Chapter 4 as *AFTm*.

In the AFTm simulation we assume the initial chromo-electric field is boost invariant in the longitudinal direction and smooth in the transverse plane, with the specific configuration given by a Glauber-type distribution:

$$E_z^0(x,y) = E_{max}^0 \left(c_c\,\rho_{coll}(x,y) + c_p\,\rho_{part}(x,y)\right), \tag{5.7}$$

with $c_p = 1 - c_c$. The two free parameters E_{max}^0 and c_c are fixed in order to match at $t_0 = 0.6\,\mathrm{fm}/c$ for RHIC and at $t_0 = 0.3\,\mathrm{fm}/c$ for LHC particle multiplicity and eccentricity of the bulk medium with those of the Th-Glauber case at the same time.
For RHIC collisions at $b = 8.1\,\mathrm{fm}$ we obtain an initial longitudinal field with

$$E_{max}^0 = 3.0\,\mathrm{GeV}^2 \qquad \text{and} \qquad c_c = 0.70, \tag{5.8}$$

while for LHC collisions at $b = 8.5\,\mathrm{fm}$ the initial configuration of E_z has

$$E_{max}^0 = 6.0\,\mathrm{GeV}^2 \qquad \text{and} \qquad c_c = 0.85. \tag{5.9}$$

The shape of the initial field in the two cases is shown in Fig. 5.5.

All the results of this section are obtained with a viscosity over entropy density ratio $4\pi\eta/s = 1$, which is fixed using an anisotropic cross section through the Chapman Enskog relation Eq. (3.20).

5.3.1 Quark-gluon plasma properties

In this subsection we show quantities related to the properties of the bulk medium, i.e. the plasma of quarks and gluons. We have already

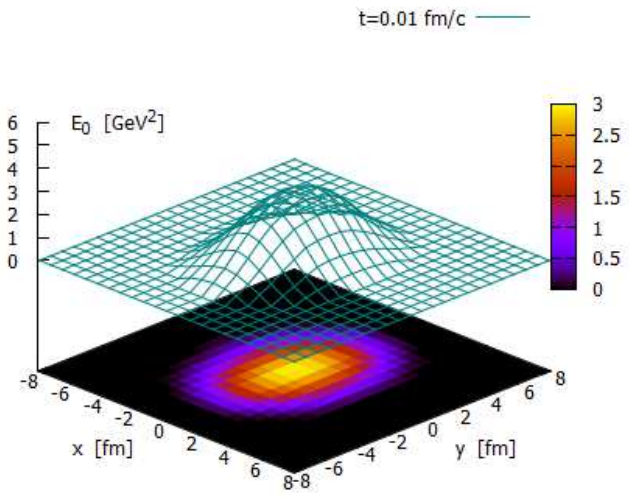

(a) RHIC

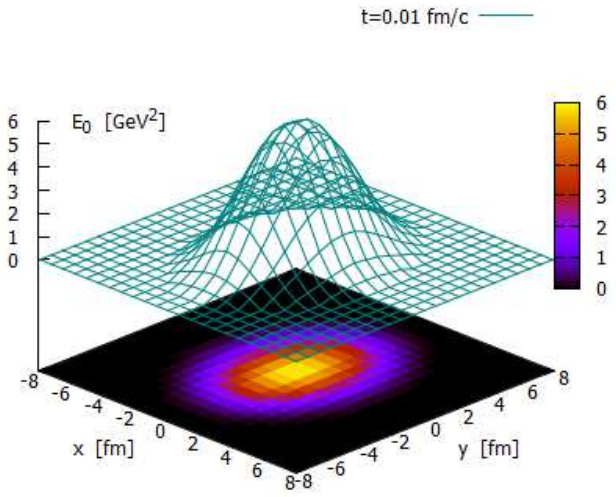

(b) LHC

Figure 5.5: Configuration of the initial longitudinal color-electric field for simulation with impact parameter $b = 8.1\,\mathrm{fm}$ at RHIC (a) and $b = 8.5\,\mathrm{fm}$ at LHC (b) energies. The maximum value is $E^0_{max} = 3.0\,\mathrm{GeV}^2$ for RHIC and $E^0_{max} = 6.0\,\mathrm{GeV}^2$ for LHC.

discusses in Section 4.3 some important quantities indicating thermalization and isotropization of the quark-gluon plasma in the AFTm case; even though we used in those simulations a simplified initial condition of a circular flux tube with homogenous chromoelectric field, qualitative behaviour and time scales of all the quantities considered are very similar to those obtained with the more realistic initialization explained in this Chapter and shown in Fig. 5.5. Here we collect other results on the quark-gluon plasma medium produced through the Schwinger mechanism and compare them with the same quantities computed with the Th-Glauber initialization.

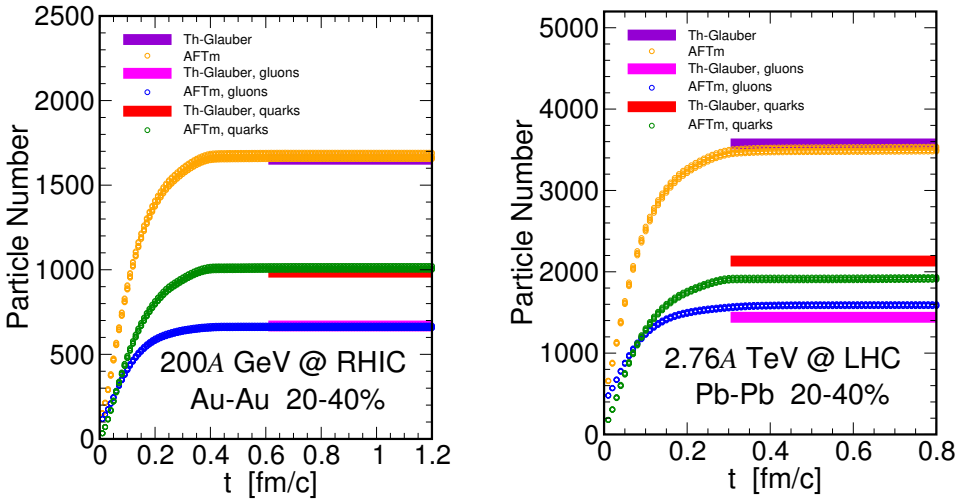

Figure 5.6: Gluon number, quark number and total particle multiplicity for 20-40% central collisions at RHIC (left panel) and LHC (right panel) energies. All calculations are performed with $4\pi\eta = 1$.

The total particle multiplicity in simulations with Th-Glauber initial condition is fixed in such a way that dN/dy for charged particle correctly reproduces the experimental one; even the AFTm simulations show the correct experimental charged particle multiplicity, since the shape of the initial field is fixed to match at $t_0 = 0.6\,\mathrm{fm}/c$ for RHIC and at $t_0 = 0.3\,\mathrm{fm}/c$ for LHC particle multiplicity and eccentricity of the bulk medium with those of the Th-Glauber case. The total particle number

for the two initializations and for both RHIC and LHC collisions is shown in Fig. 5.6 along with the gluon and quark numbers.

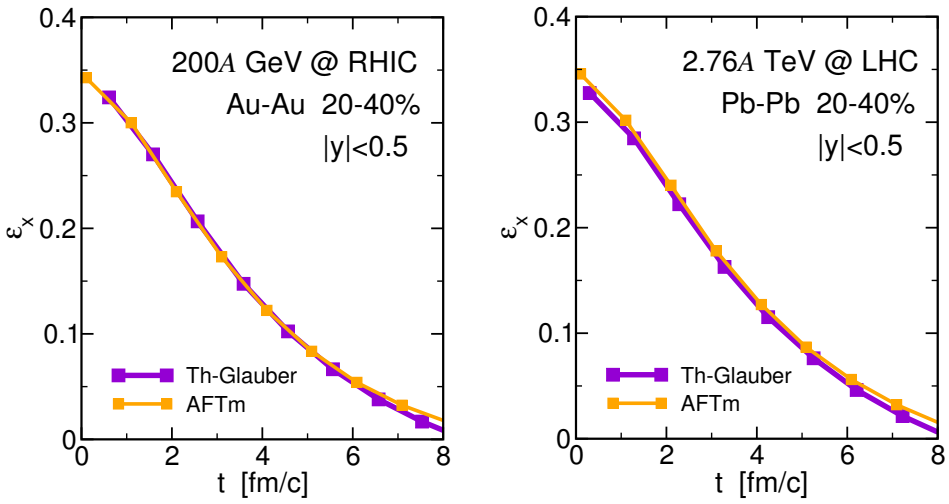

Figure 5.7: Time evolution of eccentricity averaged at midrapidity $|y| < 0.5$ for RHIC collisions at impact parameter $b = 8.1\,\mathrm{fm}$ (left panel) and for LHC collisions at $b = 8.5\,\mathrm{fm}$ (right panel). All calculations are performed with $4\pi\eta = 1$.

In Fig. 5.7 we plot the space eccentricity ϵ_x averaged at midrapidity $|y| < 0.5$ as a function of time for RHIC (left panel) and LHC (right panel) collisions at 20-40% centrality. For each of the two collision types, we represent by indigo line the results obtained with Glauber initialization and by orange line those obtained by the AFT initialization. Regardless of the collision energy, the bulk eccentricity at initial times is the same for the Th-Glauber and the AFTm cases due to the matching before explained; we find the even its time evolution is very similar for the two different initializations.

In the top panel of Fig. 5.8 we plot the gluon (left panel) and quark (right panel) spectra $dN/d^2p_T dy$ integrated over the momentum rapidity range $|y| < 0.5$ for both Th-Glauber and AFTm case reproducing RHIC initial conditions at impact parameter $b = 8.1\,\mathrm{fm}$. For the Th-Glauber case we shown spectra at the starting time $t_0 = 0.6\,\mathrm{fm}/c$ of the simulation (dashed lines) and final spectra (full lines with points); for the AFTm

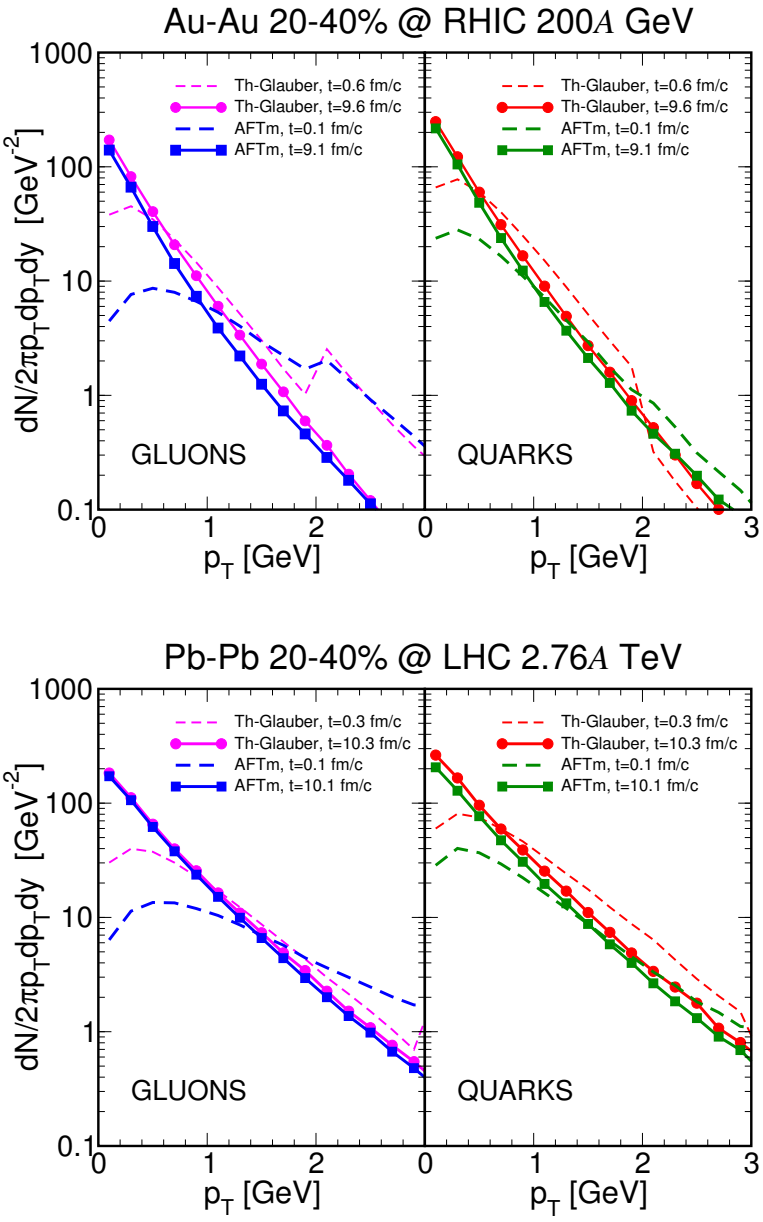

Figure 5.8: Time evolution of spectra at RHIC (top panel) and LHC (bottom panel) energy obtained by equilibrium initial condition (magenta and red curves) and with the AFT model (blue and green lines). For each collision type, gluon spectra are shown in the left panel and quark spectra in the right panel. All calculations are performed with $4\pi\eta = 1$.

simulation besides final spectra we plot those at $t = 0.1\,\mathrm{fm}/c$, which are not actual initial spectra, since at the initial time of the simulation

($t = 0.01\,\mathrm{fm}/c$) the system is made of a pure longitudinal color electric field. In the bottom panel of Fig. 5.8 the same spectra are shown in the case of LHC collisions at $b = 8.5\,\mathrm{fm}$. We find that at $t = 0.1\,\mathrm{fm}/c$ the AFTm spectrum is far from a spectrum thermalized in the transverse plane, as is expected since particle formation through Schwinger effect is not ended (see points in Fig. 5.6). Moreover, we notice that for both RHIC and LHC collisions final spectra are very similar with the two simulations.

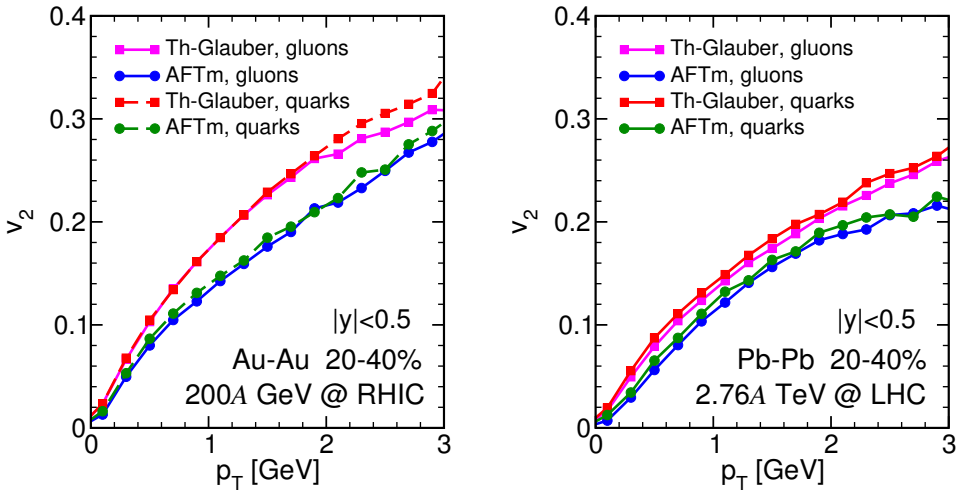

Figure 5.9: Differential elliptic flow v_2 of gluons and quarks at RHIC (left panel) and LHC (right panel) energies obtained by equilibrium initial condition (magenta and red curves) and with the AFT model (blue and green lines). All calculations are performed with $4\pi\eta = 1$.

In Fig. 5.9 we plot the elliptic flow $v_2(p_T)$ for RHIC (left panel) and LHC (right panel) collisions at impact parameter $b = 8.1\,\mathrm{fm}$ and $b = 8.5\,\mathrm{fm}$ respectively, corresponding to 20-40% centrality. We find that, even though the eccentricity at mid-rapidity shown in Fig. 5.7 has the same evolution for both simulations with the different initialization, the final elliptic flow is lower in the AFTm case, meaning that the pre-equilibrium dynamics delays the conversion of the space eccentricity to momentum anisotropy. As we will see in the next section, this fact has an impact on the formation of the photon elliptic flow which reflects

the degree of anisotropy at the emission time as photons do not further interact with the medium.

5.3.2 Photon observables at RHIC and LHC

Here we show results about spectrum and elliptic flow of photons focusing on the impact of the pre-equilibrium stage, which the majority of models developed until now cannot explore. Simulations commonly starts at a certain initial time assuming that the quark-gluon plasma is in local equilibrium. The main novelty of our work is that thermalization and isotropization are dynamical achievement in our simulations, instead of being assumed a priori. In this way we can study the impact on observables of the initial phase that, as we have shown in Chapter 4, is strongly anisotropic, not thermalized and with negative pressure. The aim of this chapter is to spot the impact of early stage non-equilibrium dynamics on photon production.

Our present formulation of the problem misses some ingredients for a complete description of photon production, such as hadronic thermal emission; this put comparison with data on a preliminary level. Instead, secondary processes like jet-photon conversion affect significantly the spectrum at higher transverse momenta, a p_T-range which is not the focus of our work. However, with our model we are in condition to capture the essential influence of early times dynamics on the subsequent evolution of the fireball created in relativistic heavy ion collisions.

Photon spectrum

In Fig. 5.10 we plot our result for final photon spectrum (main panel) and time evolution of photon number (inset panel) obtained in the Th-Glauber and in the AFTm cases for RHIC collisions at 20-40% centrality, corresponding to an impact parameter $b = 8.1\,\mathrm{fm}$. The dashed blue lines are obtained with the equilibrium initial condition, while the solid

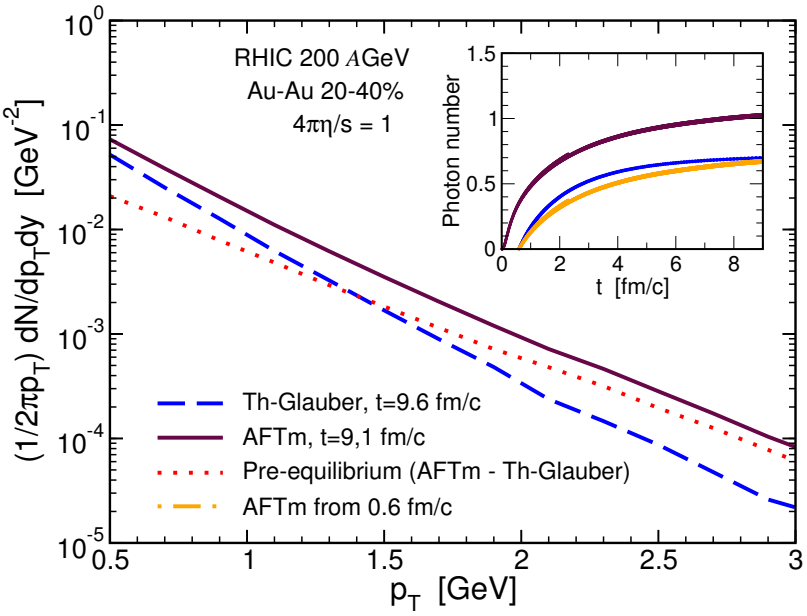

Figure 5.10: Photon spectrum at midrapidity $|y| < 0.5$ (main panel) and total photon number (inset panel) obtained by AFTm (solid maroon line) and Th-Glauber (dashed blue line) simulations. The dot-dashed orange curve corresponds to an AFTm simulation in which photon production is enabled from $t = 0.6\,\mathrm{fm}/c$.

maroon lines are the result of the AFTm simulation. In the inset panel we show also the curve obtained with the AFTm model in which photon production is artificially started at $t = 0.6\,\mathrm{fm}/c$; comparing the latter with the Th-Glauber case, we notice that the time evolution of the photon number is similar in the two simulations, meaning the system evolves in the same way after $t = 0.6\,\mathrm{fm}/c$ with Glauber and non-equilibrium initial conditions. Thus, we can consider the differences between AFTm and Th-Glauber curves as due to pre-equilibrium photons. In the main panel the red curve, being the difference between the AFTm and the Th-Glauber lines, accounts for the equilibrium contribution to the total photon spectrum at RHIC energy; it is evident that the pre-equilibrium stage gives a substantial contribution to the total photon production from the quark-gluon plasma for $p_T \gtrsim 1.5\,\mathrm{GeV}$. This fact emerges also from the photon number shown in the inset panel, as we find that the

pre-equilibrium photons constitute the 30% of the total produced in our AFTm simulation.

We stress that we do not compute photon production by integrating photon rate over a space-time volume, as it is done in hydrodynamics calculations. Indeed, we use scattering matrix elements in the collision integral; this allows to follow photon production since the very early stage as soon as particles pop up from the vacuum.

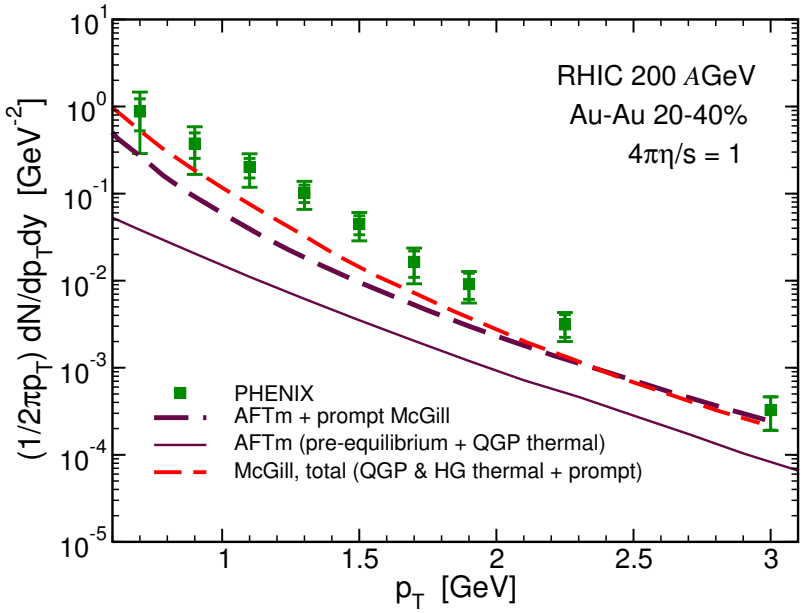

Figure 5.11: Comparison of our final photon spectrum with the one obtained by Paquet et al. from the McGill University [168] (dot-dashed red line). In the dashed indico curve McGill's prompt photons are added to our AFTm result (thin solid maroon line). Experimental data are from PHENIX Collaboration [167].

In Fig. 5.11 we compare the direct photon spectrum obtained by our AFTm simulation with experimental data [167] and with the photon spectrum computed in Ref. [168]. The latter includes not only QGP thermal photons but also thermal hadronic emission as well as prompt photons, while does not take into account photon production before QGP equilibration. In the figure we plot also our result in which prompt photons from Ref. [168] are added. We notice that we need to include in

our simulations hadronic thermal production which would enhance the direct photon yield mainly at $p_T \lesssim 2\,\mathrm{GeV}$. On the other hand our model allows to describe pre-equilibrium photons which play an important role at higher transverse momenta ($p_T > 2\,\mathrm{GeV}$) where, as shown in Fig. 5.11, our result is comparable with the one of Ref. [168]. Therefore, the inclusion of hadronic thermal photons will reduce the tension between theory and experimental data.

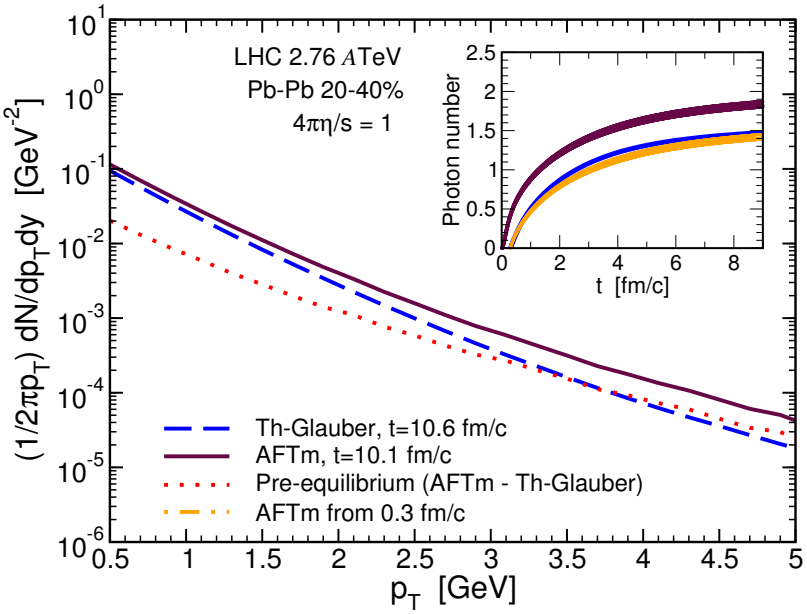

Figure 5.12: Photon spectrum at midrapidity $|y| < 0.5$ (main panel) and total photon number (inset panel) obtained by AFTm (solid maroon line) and Th-Glauber (dashed blue line) simulations. The dot-dashed orange curve corresponds to an AFTm simulation in which photon production is enabled from $t = 0.3\,\mathrm{fm}/c$.

In Fig. 5.12 we show the photon spectrum (main panel) and the photon number (inset panel) found with the Th-Glauber (dashed blue line) and the AFTm (solid maroon line) simulations at LHC energy. As in the RHIC case, we find an impact of the pre-equilibrium stage on the total photon number produced from the parton plasma: the photon number is enhanced of about 25% by the pre-equilibrium contribution. For what concern the spectrum, photons from the early stage become important

for $p_T \gtrsim 3\,\mathrm{GeV}$, but do not affect considerably the total result at lower transverse momenta.

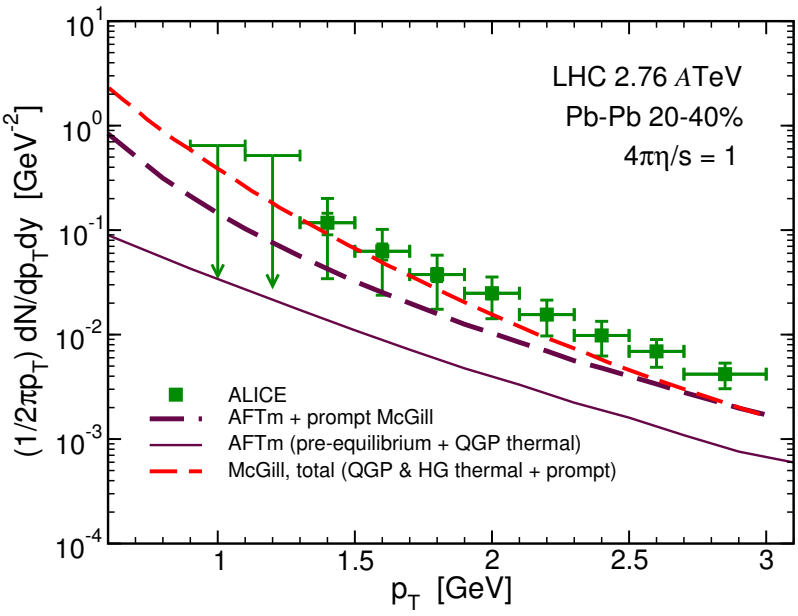

Figure 5.13: Comparison of the final photon spectrum obtained by Paquet et al. from the McGill University [168] (dot-dashed red line) with our results. In the dashed indigo curve McGill's prompt photons are added to our AFTm result (thin solid maroon line). Experimental data are from ALICE Collaboration [169].

In Fig. 5.13 we compare our photon spectrum obtained by the AFTm initialization with experimental data [169] and with the McGill result of Ref. [168]. The latter corresponds to the dot-dashed red line and contains contribution of thermal photons (from both QGP and hadron gas) and prompt photons; the thin solid maroon line is our AFTm result, including QGP thermal photons as well as pre-equilibrium photons; adding to this curve prompt photons from Ref. [168] we obtain the dashed indigo curve. As discussed before for the RHIC case, also our LHC simulation shows that the photon production from the quark-gluon plasma (pre-equilibrium and thermal) is comparable with the McGill result at high transverse momenta ($p_T \gtrsim 2.5\,\mathrm{GeV}$), but the description of the experimental photon spectrum need the inclusion of thermal hadronic emission.

Photon elliptic flow

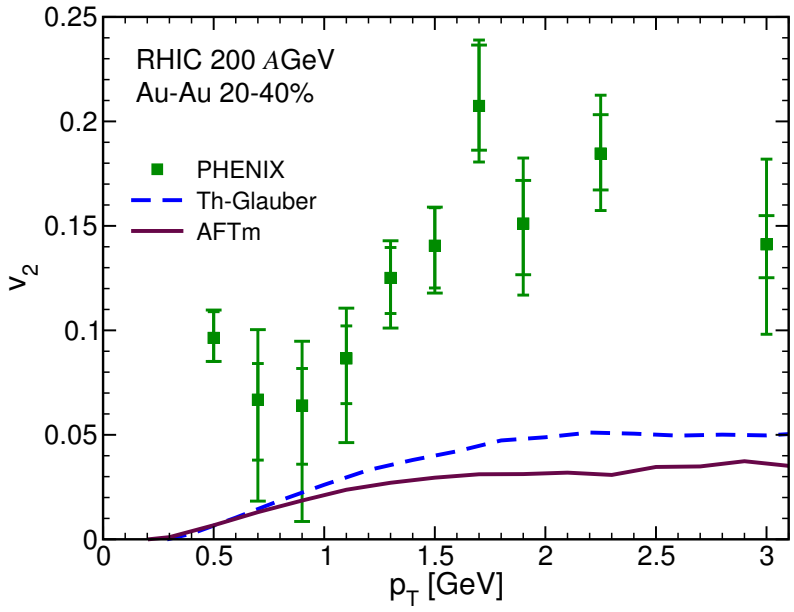

Figure 5.14: Elliptic flow $v_2(p_T)$ at midrapidity $|y| < 0.5$ for different initial conditions and $4\pi\eta/s = 1$. The calculations refer to Au-Au collisions at $\sqrt{s} = 200\,\text{GeV}$ and $b = 8.1$ fm. Experimental data are from the PHENIX Collaboration [170].

In Fig. 5.14, we show our results for the differential elliptic flow for the case of a Au-Au collision at $\sqrt{s} = 200\,\text{GeV}$ with impact parameter $b = 8.1\,\text{fm}$, which corresponds to the 20–40% centrality class at RHIC. The dashed blue curve indicates simulation with Glauber equilibrium initial condition, while the solid maroon line is the result with the AFTm initialization; green points are experimental data for direct photon $v_2(p_T)$ in the pertinent centrality class from the PHENIX Collaboration. In both cases the calculated elliptic flow systematically underestimates data, especially for the AFTm initialization, in which photons coming from the early times evolution of the fireball suppress the contribution to the momentum anisotropy brought by QGP thermal photons. However, we remind that our simulations do not include any hadronization process, so we cannot describe the thermal photon emission from hadrons, which

is expected to give a substantial contribution to the final elliptic flow: since photon azimuthal asymmetry reflects the one of the system at the emission time, we expect that thermal photons from hadron gas would bring a much higher momentum anisotropy, thus reducing the tension between our model and the data once the experimental uncertainties are taken into account. This further step is currently under progress.

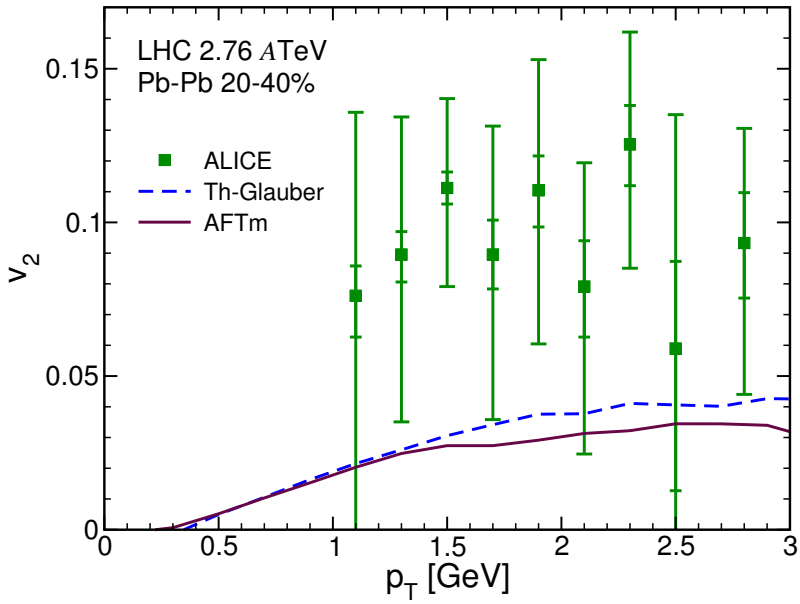

Figure 5.15: Elliptic flow $v_2(p_T)$ at midrapidity $|y| < 0.5$ for Pb-Pb collisions at $\sqrt{s} = 2.76\,\text{TeV}$ and $b = 8.5\,\text{fm}$. Simulations at fixed viscosity $4\pi\eta/s = 1$ with the two inizializations are shown, along with experimental data obtained by the ALICE Collaboration [171].

We obtain similar results at LHC energy, as we can from Fig. 5.15 where our computations of elliptic flow for $b = 8.5\,\text{fm}$ are shown. Again, the dashed blue line corresponds to our hydrolike calculation, in which the initial distribution is assumed to be thermalized in the transverse plane, while the solid maroon line is the results obtained with the non-equilibrium initial condition of the AFT model. In the figure we also plot experimental data for $v_2(p_T)$ in the 0-40% centrality class from the ALICE Collaboration [171]. Both the two simulations with different initialization undershoot experimental points but, considering the statistical

and systematic errors, the tension between our results and data will be reduced after the inclusion of thermal photons from the hadronic gas. With respect to the RHIC case, for LHC simulations we expect a higher impact of hadronic thermal photons; indeed, due to the longer lifetime of the quark-gluon plasma the elliptic flow of the bulk medium is completely developed in the QGP phase, then hadrons bring a higher level of momentum anisotropy that transfer to the thermal photons emitted. Thus a significant quantity of the final photon elliptic flow develops during the hadronic phase.

The recent observations of direct photons by the PHENIX and the ALICE Collaborations gave rise to a "puzzle" for the theoretical understanding of photon production: on one hand a large direct photon yield seems to favour photon emission at early time when the temperature of the fireball is high, but photons produced in this stage are expected to possess low momentum anisotropy; on the other hand the large elliptic flow observed, comparable in size to that of pions, indicates that photons are emitted at later time when the flow of matter is largely developed.

The tension in reproducing consistently both spectrum and elliptic flow of direct photons is a common issue of all current theoretical approaches and its solution is one of the more challenging aspects of the present research on the quark-gluon plasma physics.

CONCLUSIONS

In this thesis we have investigated the pre-equilibrium stage of ultra-relativistic heavy ion collisions, focusing on the time scales and the mechanisms responsible of the isotropization of the matter produced from an initial color-electric field and concentrating on the impact of this out-of-equilibrium phase on collective flows of the bulk matter and on photon observables. This studies have been performed within the framework of transport kinetic theory. Solving the relativistic Boltzmann-Vlasov equation coupled to color fields for the phase space distribution function $f(x, p)$ allows to follow the entire space-time evolution of the quark-gluon plasma by means of a single self-consistent scheme: starting at $t = 0^+$ with particle formation from the decay of an initial color field, we are able to describe the relaxation of the system toward a thermalized and isotropic state and investigate the development of anisotropic flows at final times.

We have build a model in which gluon and quark pairs are produced by means of the Schwinger mechanism from the decay of color-electric flux tubes, which are expected to be produced in the early stage of ultra-relativistic heavy ion collisions. The Schwinger effect consists in a vacuum instability towards the creation of particle pairs by a strong electric field

and is considered as a possible mechanism for color field decay and particle production in the context of quark-gluon plasma physics. We have coupled the evolution equation of the initial field to the relativistic transport equation which describes the dynamics of the many particle system and leads to an isotropic and thermalized state by means of collisions. This self-consistent solution of the problem allows, among other things, to take into account the backreaction of the color currents on the classical field, which has been often neglected in previous studies. According to the general understanding of high-energy nuclear collisions, this work is relevant not only for heavy ion collisions but also for proton-nucleus and proton-proton collisions, once the pertinent configuration of the initial color flux tubes is adopted.

We have studied the effect of different ratios of viscosity to entropy density η/s on quantities such as decay time of the color-electric field and isotropization and thermalization rates of the produced fluid. To this end, we have formulated transport theory in terms of a fixed value of η/s rather than insisting on a set of specific microscopic processes. Thus, we can simulate the fireball evolution with the same language of hydrodynamics but in a wider range of transverse momentum of particles and also in out-of-equilibrium phases. Indeed, in the great majority of hydrodynamical simulations of relativistic heavy ion collisions the plasma equilibration is an initial state assumption, while with our model we have investigated how it is achieved in a very short time by an initial anisotropic and not thermalized system.

We have focused first on the boost invariant longitudinal expansion of a single flux tube with a longitudinal color-electric field homogeneous in the transverse plane. In particular, we have found that the decay time of the color-electric field is a small fraction of fm/c. We have computed the time evolution of the longitudinal to the transverse pressure ratio P_L/P_L, which at initial time is equal to -1 since the system is made of

a pure color field; longitudinal pressure becomes positive in $t \approx 0.2\,\mathrm{fm}/c$ due to the fast particle production that gives a positive contribution to the pressure.

For $\eta/s \leqslant 0.3$ the strong interactions among the particles remove the initial pressure anisotropy quite efficiently and quickly, then the ratio tends to increase towards 1, which corresponds to an isotropic system. For larger values of η/s plasma oscillations cause the system to be less isotropic. We have also studied proper energy density and temperature evolution as well as particle spectra in the transverse plane for several values of η/s. In the case of small viscosity the dynamics is very efficient in getting a quick thermalization; indeed, for $\eta/s = 1$ we have found that the system gets thermalized in less than 1 fm/c; however, increasing η/s results in a longer thermalization time. The fact that we have found for a lowly viscous system an isotropization time of less than 1 fm/c would justify the use of viscous hydrodynamics with initial times $t_0 \approx 0.6$–$0.8\,\mathrm{fm}/c$ for $4\pi\eta/s = 1 - 3$.

Even though the 1+1D expanding system is interesting because a longitudinal expansion characterizes the very early times on ultra-relativistic heavy-ion collisions, a more realistic system experiences a 3+1D expansion. Therefore, we have extended our model allowing the formation of longitudinal as well as transverse components of currents and field. As in the 1+1D case, we have found that particles are produced very early, within 0.5 fm/c, independently of the value of η/s, which affects very mildly the conversion of the initial field to a plasma. The qualitative behaviour of the pressure ratio P_L/P_T is similar to that found in the 1+1D case: the larger the viscosity of the fluid the larger are the oscillations of P_L/P_T. Nevertheless, with respect to the one-dimensional expansion oscillations of P_L/P_T are more efficiently damped in a three-dimensional expanding system, vanishing after about 3 fm/c even for large viscosity. Furthermore, asymptotically $P_L/P_T \simeq 0.7$ for $4\pi\eta/s = 1$, maintaining a

higher level of anisotropy respect to the 1+1D case; this is due to the transverse expansion which, causing a quicker dilution of the system, makes collision less efficient in isotropizing particle momenta. However, the qualitative behaviour and time scales of all the quantities considered does not change in a remarkable way when turning from the 1+1D expansion to the 3+1D expansion.

The implementation of the three-dimensional expansion has allowed us to study the impact of the early times dynamics on the behaviour of physical quantities measured in experiments. We have used a realistic initial condition with a smooth distribution of the longitudinal color-electric field such to reproduce multiplicity and spatial anisotropy of particle created in collisions at RHIC and LHC energies; then we have investigate the effect of the pre-equilibrium stage on observables such as spectrum and elliptic flow of photons emitted from the quark-gluon plasma produced in heavy ion collisions. We do not compute photon production by integrating photon rate over a space-time volume as it is done in hydrodynamics calculations, but we use scattering matrix elements in the collision integral; this allows to follow photon production since the very early stage as soon as particles pop up from the vacuum.

We have found that the pre-equilibrium stage gives a substantial contribution to the total number of photons emitted from the quark-gluon plasma, being the pre-equilibrium photons about 30% of the total. This early contribution enhances the spectrum for $p_T \gtrsim 1.5\,\mathrm{GeV}$ at RHIC energy, while it becomes important for higher transverse momenta at LHC collisions ($p_T \gtrsim 3\,\mathrm{GeV}$). Thus, there is no dark age for the quark-gluon plasma, since it shines brightly in all the stages of its lifetime, even before its thermalization. Photons produced in the early stage are comparable in number with those emitted by the equilibrated quark-gluon plasma and give an important contribution in a p_T range ($p_T \gtrsim 2 - 3\,\mathrm{GeV}$) where thermal emission (both from QGP and from hadron gas) becomes

less important. Nevertheless, in order to reduce the tension with experimental data on direct photon spectrum, we need to include in our simulations hadronic thermal production which would enhance the direct photon yield mainly at $p_T \lesssim 2\,\mathrm{GeV}$.

We have computed also the elliptic flow v_2 of photons produced from the quark-gluon plasma; our results systematically underestimates data, both at RHIC and LHC energies. Moreover, we have found that photons coming from the early times evolution of the fireball suppress the contribution to the momentum anisotropy brought by QGP thermal photons. As for the spectrum, hadrons is expected to give an even more significant contribution for the description of the final elliptic flow: since photon azimuthal asymmetry reflects the one of the strongly interacting system at the emission time, we expect that thermal photons from hadron gas would bring a much higher momentum anisotropy.

The tension in reproducing consistently both spectrum and elliptic flow of direct photons is a common issue of all current theoretical approaches and its solution is one of the more challenging aspects of the present research on the quark-gluon plasma physics. The inclusion in our simulations of thermal photon production from the hadronic phase, a step which we are currently carrying out, will allow us to further improve our description of the experimental photon observables and to better understand the relative importance of the different source of photon emission.

Another main development of our work will be to progress in our description of the pre-equilibrium phase including a longitudinal color-magnetic field, which is expected to be present in a more complete description of the Glasma initial state and might induce some modification of the Schwinger amplitude of particle production. Moreover, we have neglected fluctuations of the color-electric field both in rapidity and in transverse plane, which would permit the study of the higher flow harmonics v_n. It is interesting to add these ingredients to our approach for a

more complete comprehension of the early times dynamics of relativistic heavy ion collision and of its impact on the subsequent evolution of the fireball.

BIBLIOGRAPHY

[1] S. Eidelman et al., *Phys. Lett.* B 592, 1 (2004).

[2] "The Nobel Prize in Physics 2004", http://nobelprize.org/nobel prizes/physics/laureates/2004/.

[3] D. J. Gross and F. Wilczek, *Phys. Rev. Lett.* 30, 1343 (1973).

[4] H. Politzer, *Phys. Rev. Lett.* 30, 1346 (1973).

[5] G. 't Hooft, *Nucl. Phys.* B 254, 11 (1985).

[6] K. A. Olive et al. (Particle Data Group), *Chin. Phys.* C, 38, 010009 (2014) and 2015 update.

[7] A. Pich, "Aspects of Quantum Chromodynamics", Lectures given at the ICTP Summer School in Particle Physics, Trieste [hep-ph/0001118] (1999).

[8] A. D. Linde, *Phys. Lett.* B 96, 289 (1980).

[9] S. Borsányi, G. Endrődi, Z. Fodor, A. Jakovac, S. D. Katz, S. Krieg, C. Ratti and K. K. Szabo, "The QCD equation of state with dynamical quarks", *J. High Energ. Phys.* 11, 077 (2010) [arXiv:hep-lat/1007.2580].

[10] S. Borsányi, Z. Fodor, C. Hoelbling, S. D. Katz, S. Krieg and K. K. Szabo, "Full result for the QCD equation of state with 2+1 flavors", *Phys. Lett.* B 730, 99 (2014) [arXiv:hep-lat/1309.5258].

[11] A. Bazavov et al. (HotQCD Collaboration), "Equation of state in (2+1)-flavor QCD", *Phys. Rev.* D 90, 094503 (2014) [arXiv:hep-lat/1407.6387].

[12] C. R. Allton, S. Ejiri, S. J. Hands, O. Kaczmarek, F. Karsch, E. Laermann, C. Schmidt and L. Scorzato, "The QCD thermal phase transition in the presence of a small chemical potential", *Phys. Rev.* D 66, 074507 (2002) [hep-lat/0204010].

[13] R. V. Gavai and S. Gupta, *Phys. Rev.* D 78, 114503 (2008) [arXiv:0806.2233[hep-lat]].

[14] Z. Fodor and S. D. Katz, "A new method to study lattice QCD at finite temperature and chemical potential", *Phys. Lett.* B 534, 87-92 (2002) [hep-lat/0104001].

[15] P. de Forcrand and O. Philipsen, "The QCD phase diagram for small densities from imaginary chemical potential" *Nucl. Phys.* B 642, 290-306 (2002) [hep-lat/0205016].

[16] M. D'Elia and M. P. Lombardo, *Phys. Rev.* D 67, 014505 (2003) [hep-lat/0209146].

[17] L. K. Wu, X. Q. Luo and H. S. Chen, *Phys. Rev.* D 76, 034505 (2007) [hep-lat/0611035].

[18] A. R. Bodmer, *Phys. Rev.* D 4, 1601 (1971).

[19] T. D. Lee and G. C. Wick, "Vacuum stability and vacuum excitation in a spin 0 field theory", *Phys. Rev.* D 9, 2291 (1974).

[20] J. C. Collins and M. J. Perry, "Superdense matter: Neutrons or asymptotically free quarks?", *Phys. Rev. Lett.* 34, 1353 (1975).

[21] G. Baym and S. A. Chin, "Can a neutron star be a giant mit bag?", *Phys. Lett.* B 62, 241–244 (1976).

[22] B. A. Freedman and L. D. McLerran, "Fermions and gauge vector mesons at finite temperature and density. 3. the ground state energy of a relativistic quark gas", *Phys. Rev.* D 16, 1169 (1977).

[23] G. Chapline and M. Nauenberg, "Asymptotic freedom and the baryon-quark phase transition", *Phys. Rev.* D 16, 450 (1977).

[24] E. V. Shuryak, "Theory of hadronic plasma", *Sov. Phys. JETP* 47, 212–219 (1978) [Zh. Eksp. Teor. Fiz. 74, 408 (1978)].

[25] E. V. Shuryak, "Quark-gluon plasma and hadronic production of leptons, photons and psions", *Phys. Lett.* B 78, 150 (1978) [Yad. Fiz. 2, 796 (1978)].

[26] O. K. Kalashnikov and V. V. Klimov, "Phase transition in quark-gluon plasma", *Phys. Lett.* B 88, 328 (1979).

[27] J. I. Kapusta, "Quantum chromodynamics at high temperature", *Nucl. Phys.* B 148, 461–498 (1979).

[28] E. V. Shuryak, "Quantum chromodynamics and the theory of superdense matter", *Phys. Rept.* 61, 71–158 (1980).

[29] R. Hagedorn, *Nuovo Cim. Suppl.* 3, 147 (1965).

[30] D. J. Schwarz, "The first second of the universe", *Annalen Phys.* 12, 220-270 (2003).

[31] Shapiro and Teukolsky, "Black Holes, White Dwarfs and Neutron Stars: The Physics of Compact Objects", *Wiley*, 4 (2008).

[32] Yagi. K., Hatsuda T. e Miake Y., "Quark-Gluon Plasma", *Cambridge University Press* (2005).

[33] E. Iancu, CERN-2014-003, "QCD in heavy ion collisions", 197-266 (2014) [hep-ph/1205.0579].

[34] "New State of Matter Created at CERN". The CERN Courier. http://press.web.cern.ch/press-releases/2000/02/new-state-matter-createdcern. (2000) 6

[35] Bass et al, representing the US Heavy-Ion Community. "Hot and Dense QCD Matter: Unraveling the Mysteries of the Strongly Interacting Quark-Gluon-Plasma". A Community White Paper on the Future of Relativistic Heavy-Ion Physics in the US. 4, 6, 8

[36] K. Adcox et al. (PHENIX Collaboration), "Formation of dense partonic matter in relativistic nucleus nucleus collisions at RHIC: Experimental evaluation by the Phenix collaboration", *Nucl. Phys.* A 757, 184–283 (2005) [nucl-ex/0410003].

[37] J. Adams et al. (STAR Collaboration), "Experimental and theoretical challenges in the search for the quark gluon plasma: The Star collaboration's critical assessment of the evidence from RHIC collisions", *Nucl. Phys.* A 757, 102–183 (2005) [nucl-ex/0501009].

[38] I. Arsene et al. (BRAHMS Collaboration), "Quark gluon plasma and color glass condensate at RHIC? The perspective from the BRAHMS experiment", *Nucl. Phys.* A 757, 1-27 (2005) [nucl-ex/0410020].

[39] B. B. Back et al., "The Phobos perspective on discoveries at Rhic", *Nucl. Phys.* A 757, 28–101 (2005) [nucl-ex/0410022].

[40] A. Adare et al. (PHENIX Collaboration), "Detailed measurement of the e+e− pair continuum in p+p and Au+Au collisions at $\sqrt{s_{NN}} = 200$

GeV and implications for direct photon production", *Phys. Rev.* C 81, 034911 (2010).

[41] M. L. Miller, K. Reygers, S. J. Sanders and P. Steinberg, "Glauber Modeling in High-Energy Nuclear Collisions", *Ann. Rev. Nucl. Part. Sci.* 57, 205–243 (2007).

[42] T. Lappi and L. McLerran, *Nucl. Phys.* A 772, 200 (2006).

[43] F. Gelis and R. Venugopalan, *Acta Phys. Pol.* B 37, 3253 (2006).

[44] T. Lappi, *J. Phys.* G 35, 104052 (2008).

[45] F. Gelis, T. Lappi and L. McLerran, *Nucl. Phys.* A 828, 149 (2009).

[46] K. Fukushima and F. Gelis, *Nucl. Phys.* A 874, 108 (2012).

[47] H. Iida, T. Kunihiro, B. Muller, A. Ohnishi, A. Schafer and T. T. Takahashi, *Phys. Rev.* D 88, 094006 (2013).

[48] F. D. Aaron et al., "Combined Measurement and QCD Analysis of the Inclusive e+-p Scattering Cross Sections at HERA", *JHEP* 01, 109 (2010).

[49] W. Florkowski, "Phenomenology of Ultra-Relativistic Heavy Ion Collisions", *World Scientific, Singapore* (2010).

[50] P. Romatschke and R. Venugopalan, *Phys. Rev.* D 74, 045011 (2006).

[51] H. Fujii, K. Itakura and A. Iwazaki, *Nucl. Phys.* A 828, 178 (2009).

[52] T. Epelbaum and F. Gelis, *Phys. Rev. Lett.* 111, 232301 (2013).

[53] J. Randrup and S. Mrowczynski, "Chromodynamic Weibel instabilities in relativistic nuclear collisions", *Phys. Rev.* C 68, 034909 (2003) [arXiv:nucl-th/0303021].

[54] S. Mrowczynski, "Instabilities driven equilibration of the quark-gluon plasma", *Acta Phys. Pol.* B 37, 427-454 (2006) [arXiv:hep-ph/0511052].

[55] M. Attems, A. Rebhan and M. Strickland, *Phys. Rev.* D 87, 025010 (2013).

[56] A. Rebhan, P. Romatschke and M. Strickland, "Hard-loop dynamics of non-Abelian plasma instabilities", *Phys. Rev. Lett.* 94, 102303 (2005) [arXiv:hep-ph/0412016]; "Dynamics of quark-gluon plasma instabilities in discretized hard-loop approximation", *J. High Energy Phys.* 09 (2005) 041 [arXiv:hep-ph/0505261].

[57] L. Bellantuono, P. Colangelo, F. De Fazio, and F. Giannuzzi, *J. High Energy Phys.* 07, 053 (2015).

[58] M. P. Heller, R. A. Janik, M. Spalinski and P.Witaszczyk, *Phys. Rev. Lett.* 113, 261601 (2014).

[59] V. Greco, C. M. Ko and P. Levai, "Parton coalescence at RHIC", *Phys. Rev.* C 68, 034904 (2003).

[60] R. Fries, V. Greco and P. Sorensen, "Coalescence Models For Hadron Formation From Quark Gluon Plasma", *Ann. Rev. Nucl. Part. Sci.* 58, 177-205 (2008).

[61] G. Baym, B. L. Friman, J.-P. Blaizot, M. Soyeur and W. Czyz, *Nucl. Phys.* A 407, 541 (1983).

[62] J. D. Bjorken, "Highly relativistic nucleus-nucleus collisions: The central rapidity region", *Phys. Rev.* D 27, 140 (1983).

[63] E. Abbas et al. (ALICE Collaboration), "Centrality dependence of the pseudorapidity density distribution for charged particles in Pb-Pb collisions at $\sqrt{s_{NN}} = 2.76$ TeV", *Phys. Lett.* B 726, 610–622 (2013).

[64] P. F. Kolb, J. Sollfrank and U. W. Heinz, *Phys. Rev.* C 62, 054909 (2000).

[65] B. V. Jacak and B. Müller, "The Exploration of Hot Nuclear Matter", *Science* 337, 310 (2012).

[66] K.H. Ackermann et al., "Elliptic flow in Au + Au collisions at $\sqrt{s_{NN}} = 130$ GeV", *Phys. Rev. Lett.* 86, 402–407 (2001).

[67] P. F. Kolb and U. W. Heinz, "Hydrodynamic description of ultrarelativistic heavy ion collisions", invited review for "Quark Gluon Plasma 3", editors: R. C. Hwa and X.-N. Wang, *World Scientific, Singapore* (2003).

[68] S. S. Adler et al. (PHENIX Collaboration), "Elliptic flow of identified hadrons in Au+Au collisions at $\sqrt{s_{NN}} = 200$ GeV", *Phys. Rev. Lett.* 91, 182301 (2003).

[69] J. Adams et al. (STAR Collaboration), "Particle type dependence of azimuthal anisotropy and nuclear modification of particle production in Au + Au collisions at $\sqrt{s_{NN}} = 200$ GeV", *Phys. Rev. Lett.* 92, 052302 (2004).

[70] J. Adams et al. (STAR Collaboration), "Multi-strange baryon elliptic flow in Au + Au collisions at $\sqrt{s_{NN}} = 200$ GeV", *Phys. Rev. Lett.* 95, 122301 (2005).

[71] U. Heinz, "From SPS to RHIC: Maurice and the CERN heavy-ion programme", *Phys. Scripta* 78, 028005 (2008) [nucl-th/08054572].

[72] B. B. Back et al., *Phys. Rev.* C 72, 051901 (2005).

[73] B. B. Back et al., *Phys. Rev. Lett.* 94, 122303 (2005).

[74] R. S. Bhalerao, J.-P. Blaizot, N. Borghini and J. Y. Ollitrault, *Phys. Lett.* B 627, 49 (2005).

[75] D. Molnar and S. A. Voloshin, "Elliptic flow at large transverse momenta from quark coalescence", *Phys. Rev. Lett.* 91, 092301 (2003).

[76] A. Adare et al. (PHENIX Collaboration), "Scaling properties of azimuthal anisotropy in Au+Au and Cu+Cu collisions at s(NN) = 200-GeV", *Phys. Rev. Lett.* 98, 162301 (2007).

[77] J. D. Bjorken, "Energy Loss of Energetic Partons in Quark-Gluon Plasma: Possible Extinction of High p(t) Jets in Hadron-Hadron Collisions" (1982).

[78] D. A. Appel, "Jets as a probe of quark-gluon plasma", *Phys. Rev.* D 33, 717 (1986).

[79] M. Gyulassy, I. Vitev, X.-N. Wang and B.-W. Zhang, "Jet quenching and radiative energy loss in dense nuclear matter" published in "Quark Gluon Plasma 3", editors: R.C. Hwa and X.N. Wang, *World Scientific*, Singapore (2003).

[80] X. N. Wang, "Discovery of jet quenching and beyond", *Nucl. Phys.* A 750, 98–120 (2005).

[81] J. Casalderrey-Solana and C. A. Salgado, "Introductory lectures on jet quenching in heavy ion collisions", *Acta Phys. Polon.* B 38, 3731–3794 (2007).

[82] R. Rapp and H. van Hees, "Heavy Quarks in the Quark-Gluon Plasma", R. C. Hwa, X.-N. Wang (Ed.) Quark Gluon Plasma 4, World Scientific, 111 (2010).

[83] V. Greco, H. van Hees and R. Rapp, "Heavy Quark Dynamics in the QGP", *AIP Conf.Proc.* 1422, 117-126 (2012).

[84] S. K. Das, F. Scardina, S. Plumari and V. Greco, "Heavy-flavor in-medium momentum evolution: Langevin versus Boltzmann approach", *Phys. Rev.* C 90, 044901 (2014) [arXiv:nucl-th/1312.6857].

[85] Y. L. Dokshitzer and D. E. Kharzeev, "Heavy quark colorimetry of QCD matter," *Phys. Lett.* B 519, 199–206 (2001).

[86] S. K. Das, F. Scardina, S. Plumari and V. Greco, "Toward a solution to the R_{AA} and v_2 puzzle for heavy quarks", *Phys. Lett.* B 747, 260-264 (2015) [arXiv:nucl-th/1502.03757].

[87] T. Matsui and H. Satz, "J/psi Suppression by Quark-Gluon Plasma Formation", *Phys. Lett.* B 178, 416 (1986).

[88] H. Goldstein, "Classical Mechanics", *Addison-Wesley*, Cambridge, Mass., Ch. 8-8 (1953).

[89] L. P. Csernai, "Introduction to Relativistic Heavy Ion Collisions", *John Wiley & Sons*, New York (1994).

[90] H.-T. Elze, "Relativistic quantum transport theory", *AIP Conf.Proc.* 631, 229-252 (2002).

[91] D. Vasak, M. Gyulassy and H.-T. Elze, "Quantum transport theory for abelian plasmas", *Ann. Phys.* 173, 462-492 (1987).

[92] H.-T. Elze, M. Gyulassy, D. Vasak, H. Heinz, H. Stoecker and W. Greiner, "Towards a relativistic selfconsistent quantum transport theory of hadronic matter", *Mod. Phys. Lett.* A 2, 451–460 (1987).

[93] C.-Y. Wong, "Dynamics of nuclear fluid. VIII. Time-dependent Hartree-Fock approximation from a classical point of view", *Phys. Rev.* C 25, 1460–1475 (1982).

[94] G. F. Bertsch and S. Das Gupta, "A Guide to microscopic models for intermediate-energy heavy ion collisions", *Phys. Rept.* 160, 189–233 (1988).

[95] W. Cassing, V. Metag, U. Mosel and K. Niita, "Production of energetic particles in heavy ion collisions", *Phys. Rept.* 188, 363–449 (1990).

[96] H. Kruse, B. V. Jacak and H. Stoecker, "Microscopic theory of pion production and sidewards flow in heavy ion collisions", *Phys. Rev. Lett.* 54, 289–292 (1985).

[97] G. Ferini, M. Colonna, M. Di Toro and V. Greco, "Scalings of Elliptic Flow for a Fluid at Finite Shear Viscosity", *Phys. Lett.* B 670, 325–329 (2009).

[98] V. Greco, M. Colonna, M. Di Toro and G. Ferini, *Prog. Part. Nucl. Phys.* 62, 562 (2009).

[99] Z. Xu and C. Greiner, "Thermalization of gluons in ultrarelativistic heavy ion collisions by including three-body interactions in a parton cascade", *Phys. Rev.* C 71, 064901 (2005).

[100] P. Danielewicz and G.F. Bertsch, "Production of deuterons and pions in a transport model of energetic heavy ion reactions", Nucl. Phys. A 533, 712–748 (1991).

[101] A. Lang, H. Babovsky, W. Cassing, U. Mosel, H.-G. Reusch and K. Weber, "A new treatment of boltzmann-like collision integrals in nuclear kinetic equations", *J. Comput. Phys.* 106, 391–396 (1993).

[102] W. Cassing, *Nucl. Phys.* A 700, 618 (2002).

[103] S. Plumari, A. Puglisi, F. Scardina and V. Greco, "Shear viscosity of a strongly interacting system: Green-Kubo correlator versus

Chapman-Enskog and relaxation-time approximations", *Phys. Rev.* C 86, 054902 (2012).

[104] S. Plumari and V. Greco, "Elliptic Flow and Shear Viscosity within a Transport Approach from RHIC to LHC Energy", *AIP Conf. Proc.* 1422, 56-61 (2012).

[105] S. Plumari, A. Puglisi, M. Colonna, F. Scardina and V. Greco, "Shear viscosity and chemical equilibration of the QGP", *J. Phys. Conf. Ser.* 420, 012029 (2013).

[106] M. Ruggieri, F. Scardina, S. Plumari, and V. Greco, "Elliptic Flow from Nonequilibrium Initial Condition with a Saturation Scale", *Phys. Lett.* B 727, 177-181 (2013).

[107] M. Ruggieri, F. Scardina, S. Plumari and V. Greco, "Thermalization, isotropization, and elliptic flow from nonequilibrium initial conditions with a saturation scale", *Phys. Rev.* C 89, 054914 (2014).

[108] P. B. Arnold, J. Lenaghan and G. D. Moore, "QCD plasma instabilities and bottom up thermalization", *J. High Energy Phys.* 08, 002 (2003) [arXiv:hep-ph/0307325]; erratum added online, sep/29/2004.

[109] P. B. Arnold, J. Lenaghan, G. D. Moore and L. G. Yaffe, "Apparent thermalization due to plasma instabilities in quark-gluon plasma", *Phys. Rev. Lett.* 94, 072302 (2005) [arXiv:nucl-th/0409068].

[110] P. B. Arnold, G. D. Moore and L. G. Yaffe, "The Fate of non-Abelian plasma instabilities in 3+1 dimensions", *Phys. Rev.* D 72, 054003 (2005) [arXiv:hep-ph/0505212].

[111] P. B. Arnold and G. D. Moore, "QCD plasma instabilities: The NonAbelian cascade", *Phys. Rev.* D 73, 025006 (2006) [arXiv:hep-ph/0509206].

[112] A. Rebhan, M. Strickland, and M. Attems, "Instabilities of an anisotropically expanding non-Abelian plasma: 1D+3V discretized hard-loop simulations", *Phys. Rev.* D 78, 045023 (2008) [arXiv:hep-ph/0802.1714].

[113] W. van der Schee, P. Romatschke and S. Pratt, *Phys. Rev. Lett.* 111, 222302 (2013).

[114] Y. V. Kovchegov and A. Taliotis, *Phys. Rev.* C 76, 014905 (2007).

[115] M. P. Heller, R. A. Janik and P. Witaszczyk, *Phys. Rev. Lett.* 108, 201602 (2012).

[116] W. Heisenberg and H. Euler, "Folgerungen aus der Diracschen Theorie des Positrons", *Z. Phys.* 98, 714 (1936).

[117] J. S. Schwinger, "On Gauge Invariance and Vacuum Polarization", *Phys. Rev.* 82, 664 (1951).

[118] G. V. Dunne, in "From Fields to Strings", edited by M. Shifman et al., Vol. 1 (World Scientific, Singapore, 2005), pp. 445–522.

[119] R. Ryblewski and W. Florkowski, "Equilibration of anisotropic quark-gluon plasma produced by decays of color flux tubes", *Phys. Rev.* D 88, 034028 (2013).

[120] G. Gatoff, A. K. Kerman and T. Matsui, "Flux-tube model for ultrarelativistic heavy-ion collisions: Electrohydrodynamics of a quark-gluon plasma", *Phys. Rev.* D 36, 114 (1987).

[121] F. Hebenstreit, J. Berges and D. Gelfand, "Real-Time Dynamics of String Breaking", *Phys. Rev. Lett.* 111, 201601 (2013); F. Hebenstreit, J. Berges and D. Gelfand, "Simulating fermion production in 1+1 dimensional QED", *Phys. Rev.* D 87, 105006 (2013).

[122] F. Gelis and N. Tanji, "Formulation of the Schwinger mechanism in classical statistical field theory", *Phys. Rev.* D 87, 125035 (2013).

[123] G. C. Nayak, "Nonperturbative quark-antiquark production from a constant chromoelectric field via the Schwinger mechanism", *Phys. Rev.* D 72, 125010 (2005) [arXiv:hep-ph/0510052].

[124] F. Cooper and G. C. Nayak, "Nonperturbative gluon pair production from a constant chromo-electric field via the Schwinger mechanism in arbitrary gauge", *Phys. Rev.* D 73, 065005 (2006) [arXiv:hep-ph/0511053].

[125] G. C. Nayak, "Schwinger mechanism for gluon-pair production in the presence of arbitrary time-dependent chromo-electric field", *Eur. Phys. J.* C 59, 715 (2009).

[126] G. C. Nayak, "Schwinger Mechanism for Quark-Antiquark Production in the Presence of Arbitrary Time Dependent Chromo-Electric Field", *Electron. J. Theor. Phys.* 8, 279 (2011) [arXiv:hep-ph/0705.2770].

[127] A. Casher, H. Neuberger and S. Nussinov, "Chromoelectric-flux-tube model of particle production", *Phys. Rev.* D 20, 179 (1979).

[128] N. K. Glendenning and T. Matsui, "Creation of $q\bar{q}$ pair in a chromoelectric flux tube", *Phys. Rev.* D 28, 2890 (1983).

[129] A. Bialas and W. Czyz, "", *Phys. Rev.* D 30, 2371 (1984).

[130] A. Bialas and W. Czyz, "", *Z. Phys.* C 28, 255 (1985).

[131] A. Bialas and W. Czyz, "Conversion of color field into qq matter in the central region of high-energy heavy ion collisions", *Nucl. Phys.* B 267, 242; *Acta Phys. Pol.* B 17, 635 (1986).

[132] M. Gyulassy and A. Iwazaki, "Quark and gluon pair production in SU(N) covariant constant fields", *Phys. Lett.* B 165, 157 (1985).

[133] H. T. Elze, M. Gyulassy, and D. Vasak, *Nucl. Phys.* B 276, 706; *Phys. Lett.* B 177, 402 (1986).

[134] A. Bialas, W. Czyz, A. Dyrek, and W. Florkowski, *Nucl. Phys.* B 296, 611 (1988).

[135] A. Bialas, W. Czyz, A. Dyrek, W. Florkowski and R. B. Peschanski, *Phys. Lett.* B 229, 398 (1989).

[136] A. Dyrek and W. Florkowski, *Nuovo Cimento* A 102, 1013 (1989).

[137] K. Bajan and W. Florkowski, Acta Phys. Pol. B 32, 3035 (2001).

[138] W. Florkowski, *Acta Phys. Pol.* B 35, 799 (2004).

[139] W. Florkowski and R.Ryblewski, *Nucl. Phys.* A 931, 343 (2014).

[140] N. Tanji, *Ann. Phys.* 324, 1691 (2009).

[141] N. Tanji, *Phys. Rev.* D 83, 045011 (2011).

[142] N. Tanji and K. Itakura, *Phys. Lett.* B 713, 117 (2012).

[143] Z. Xu, C. Greiner and H. Stocker, "PQCD calculations of elliptic flow and shear viscosity at RHIC", *Phys. Rev. Lett.* 101, 082302 (2008).

[144] Z. Xu and C. Greiner, "Elliptic flow of gluon matter in ultrarelativistic heavy-ion collisions", *Phys. Rev.* C 79, 014904 (2009).

[145] E. L. Bratkovskaya, W. Cassing, V. P. Konchakovski and O. Linnyk, "Parton-Hadron-String Dynamics at Relativistic Collider Energies", *Nucl. Phys.* A 856, 162-182 (2011).

[146] L. D. Landau and E. M. Lifshitz, "Electrodynamics of Continuous Media, A Course of Theoretical Physics", Vol. 8 *Pergamon Press*, Oxford, UK (1960).

[147] M. Ruggieri, A. Puglisi, L. Oliva, S. Plumari, F. Scardina and V. Greco, "Modelling Early Stages of Relativistic Heavy Ion Collisions: Coupling Relativistic Transport Theory to Decaying Color-electric Flux Tubes", *Phys. Rev.* C 92, 064904 (2015).

[148] A. Puglisi, "Transport coefficients and early time dynamics of the Quark-Gluon Plasma created in ultra-relativistic heavy ion collisions", Ph.D. Thesis at Università degli Studi di Catania (2015).

[149] D. A. Teaney, [arXiv:nucl-th/0905.2433].

[150] M. M. Aggarwal et al. (WA98 Collaboration), Phys. Rev. Lett. 85, 3595 (2000).

[151] S. S. Adler et al. (PHENIX Collaboration), Phys. Rev. Lett. 94, 232301 (2005).

[152] S. S. Adler et al. (PHENIX Collaboration), Phys. Rev. C 76, 034904 (2007).

[153] A. Adare et al. (PHENIX Collaboration), [arXiv:nucl-ex/0804.4168].

[154] S. Bathe (PHENIX Collaboration), Eur. Phys. J. C 49, 225 (2007).

[155] H. Gong (PHENIX Collaboration), Proceedings of 19th International Conference on Ultra-Relativistic Nucleus-Nucleus Collisions: Quark Matter 2006 (QM2006), Shanghai, China, 14–20 Nov 2006 [arXiv:nucl-ex/0705.1133].

[156] T. Dahms et al.: Eur. Phys. J. C 49, 249 (2007).

[157] R. Chatterjee, L. Bhattacharya and D. K. Srivastava, "Electromagnetic Probes", *Lect. Notes Phys.* 785, 219-264 (2010) [arXiv:nucl-th/0901.3610].

[158] Kapusta, Lichard and Seibert, *Phys. Rev.* D 44, 2774 (1991); Phys. Rev. D 47, 4171 (1993) [Erratum].

[159] R. Baier, H. Nakkagawa, A. Niegawa and K. Redlich, Z. Phys. C 53, 433 (1992).

[160] H. Nadeau, J. Kapusta and P. Lichard, Phys. Rev. C 45, 3034 (1992).

[161] P. Aurenche, F. Gelis, H. Zaraket and R.Kobes, "Bremsstrahlung and photon production in thermal QCD", *Phys. Rev.* D 58, 085003 (1998).

[162] P. Aurenche, F. Gelis and H. Zaraket, "Kinoshita-Lee-Nauenberg theorem, magnetic mass, and thermal photon production", *Phys. Rev.* D 61, 116001 (2000); "Landau-Pomeranchuk-Migdal effect in thermal field theory", *Phys. Rev.* D 62, 096012 (2000).

[163] P. Arnold, G. D. Moore and L. G. Yaffe *JHEP* **0112**, 009 (2001) *and references therein.*

[164] L. D. McLerran and T. Toimela, Phys. Rev. D 31, 545 (1985).

[165] H. A. Weldon, Phys. Rev. D 42, 2384 (1990).

[166] C. Gale and J. Kapusta, Nucl. Phys. B 357, 65 (1991).

[167] A. Adare *et al.* (PHENIX Collaboration), "Centrality dependence of low-momentum direct-photon production in Au++Au collisions at $\sqrt{s_{NN}} = 200\,\mathrm{GeV}$", *Phys. Rev.* C **91**, 064904 (2015).

[168] J.-F. Paquet, C. Shen, G. S. Denicol, M. Luzum, B. Schenke, S. Jeon and C. Gale, "Production of photons in relativistic heavy-ion collisions", *Phys. Rev.* C **93** 044906 (2016).

[169] J. Adam *et al.* (ALICE Collaboration), "Direct Photon Production in Pb-Pb Collisions at $\sqrt{s_{NN}} = 2.76\,\text{TeV}$", *Phys. Lett.* B 754, 235 (2016).

[170] A. Adare *et al.* (PHENIX Collaboration), "Azimuthally anisotropic emission of low-momentum direct photons in Au+Au collisions at $\sqrt{s_{NN}} = 200\,\text{GeV}$" (2015) [arXiv:nucl-ex/1509.07758].

[171] D. Lohner (ALICE Collaboration), "Measurement of Direct-Photon Elliptic Flow in Pb-Pb Collisions at $\sqrt{s_{NN}} = 2.76\,\text{TeV}$", *J. Phys. Conf. Ser.* 446, 012028 (2013).